High-resolution laboratory spectroscopy of transient metal-containing molecules

by

Shanshan Yu

A thesis
presented to the University of Waterloo
in fulfillment of the
thesis requirement for the degree of
Doctor of Philosophy
in
Chemistry

Waterloo, Ontario, Canada, 2007

AUTHOR'S DECLARATION

I hereby declare that I am the sole author of this thesis. This is a true copy of the thesis, including any required final revisions, as accepted by my examiners.

I understand that my thesis may be made electronically available to the public.

Abstract

Ten gaseous transient metal-containing molecules have been synthesized and studied by high resolution spectroscopy. Transient molecules are molecules with a short lifetime, and they play an important role in chemistry because they are reaction intermediates. One of the difficulties faced in studying transient molecules is their typically low concentrations under laboratory conditions.

Three types of sources were used to generate these molecules: 1) an emission source that combines a high temperature furnace with an electrical discharge was used to generate SbH, SbD, TeH, TeD, CdH_2, CdD_2, HZnCl and BeF_2; 2) a King furnace (carbon tube furnace) was used to synthesize CoS; 3) a Broida-type oven (metal flow reactor) was used to generate SrOD. Two spectroscopic techniques were employed to study these molecules: 1) Fourier transform infrared emission spectroscopy was used to study SbH, SbD, TeH, TeD, CdH_2, CdD_2, HZnCl, BeF_2, and CoS. 2) Laser-induced fluorescence spectroscopy was employed to study SrOD. One or two lasers were used to excite the SrOD molecules from the ground state to excited electronic states and then these SrOD molecules relaxed back to the ground state by emitting fluorescence, which was detected by a photomultiplier tube.

Significantly-improved spectroscopic constants have been obtained for SbH, SbD, TeH and TeD. For SbH and SbD, the infrared $X\ ^3\Sigma^-$ vibration-rotation bands and the near infrared $b\ ^1\Sigma^+ - X\ ^3\Sigma^-$ transition were observed and rotationally analyzed, and a Hund's case (a) fit was performed for each of the four observed SbH isotopologues. For TeH and TeD, the $X\ ^2\Pi_{3/2}$ vibration-rotation bands and the near infrared $X\ ^2\Pi_{1/2} - X\ ^2\Pi_{3/2}$ transition have been observed and rotationally analyzed, and Hund's case (a) and case (c) fits were performed for each of the ten observed TeH isotopologues.

New spectroscopic constants were obtained for HZnCl, CdH_2 and CdD_2. These three molecules have been successfully generated in the gas phase for the first time. The fundamental band and one hot band were obtained for the H–Zn stretching mode (ν_1) and for the antisymmetric stretching mode (ν_3) of CdH_2 and CdD_2. A least-squares fit was performed for each of the four observed HZnCl isotopologues and the twelve observed CdH_2 isotopologues

For the first time, a complete set of molecular constants for all three vibrational frequencies was experimentally determined for BeF_2. Thirteen new hot bands were rotationally analyzed and the ν_1, ν_2, and ν_3 vibrational frequencies were directly determined by fitting nineteen bands together. The traditional equilibrium vibrational and rotational constants were obtained for BeF_2 by simultaneously fitting the observed vibrational term values and B rotational constants.

New spectroscopic constants were obtained for two electronic states of CoS and SrOD, respectively. The $A\ ^4\Phi_i - X\ ^4\Delta_i$ and $B\ ^4\Pi_i - X\ ^4\Delta_i$ transitions of CoS and the $\widetilde{A}^2\Pi - \widetilde{X}^2\Sigma^+$ and $\widetilde{C}^2\Pi - \widetilde{A}^2\Pi$ transitions of SrOD were observed for the first time. Hund's case (c) fits were performed for the CoS transitions and Hund's case (a) fits were performed for the SrOD transitions.

Acknowledgements

My thanks go first and foremost to my thesis supervisor, Dr. Peter Bernath, for his invaluable guidance and support throughout the course of this work. It has been a unique and most pleasant experience working with him. I am amazed at the amount of knowledge he possesses, and I am grateful to have benefited from it.

I wish to thank Dr. Robert J. Le Roy, Dr. Kaley Walker, Dr. Nick Westwood, and Dr. James Martin for agreeing to serve on my Ph.D. advisory committee and for their comments and suggestions during the course of my Ph.D. I would also like to thank the Natural Sciences and Engineering Research Council (NSERC) of Canada and the Ontario Graduate Scholarships (OGS) for providing funding support.

I would like to acknowledge my collaboration with Dr. Jacek Koput from Poland, who carried out high level *ab initio* calculations on BeF_2. I thank Dr. Robert J. Le Roy for providing his RKR1 and LEVEL computer programs and useful discussions on using these programs. I thank Dr. E. H. Fink from Germany for providing some unpublished line positions of SbH and SbD. I thank Dr. John. L. Hardwick for providing a copy of his program used for the Fermi resonance analysis of BeF_2.

While writing this thesis, I was working with Dr. Takayoshi Amano. I wish to thank him for teaching me submillimeter wave spectroscopy. I also would like to thank Dr. Yangqin Chen, who introduced me into the field of molecular spectroscopy and supervised my Master study.

Throughout the three and half years at Waterloo, I worked with a group of great people. I enjoyed my collaborations with Alireza Shayesteh, Iouli Gordon, Dominique Appadoo, Jin-Guo Wang and Phlilip Sheridan, who were the senior students and postdocs and were always ready to teach when I came to them with questions. I thank Sean McLeod for fixing numerous computer problems for me. I thank other current and former members of the Bernath group for their help and friendship. I am grateful for all the wonderful memories I am taking with me.

Especially, I thank Dejian for being a great husband and colleague. He participated in my first three projects in the Bernath laboratory and helped me build my self-confidence in spectroscopy right at the beginning of my Ph.D. study. He has been a wonderful source of inspiration, and many of my ideas on research and class work came from talking with him. Without his support and love, most of the work presented here would never have been done.

Finally, I'd like to express my deepest appreciation to my parents, sisters and brother for their support and encouragement in every aspect of my life.

For Dejian

Table of Contents

List of Figures

List of Tables

Chapter 1

Introduction

Molecular spectroscopy is one of the most important methods for investigating molecular structure. From the analysis of high-resolution spectra, one can obtain detailed information about electronic structure, chemical bonding and geometries of molecules. Transient molecules are molecules with a short lifetime, and they play an important role in chemistry because they are reaction intermediates. Some transient molecules are found in astronomical objects and are of astrophysical interest. Due to their high reactivity, transient molecules typically occur at very low concentrations in the laboratory, which makes their laboratory detection very difficult. Many astronomical spectra are waiting to be interpreted because laboratory comparison data are not available or are incomplete.

This thesis investigates the high-resolution spectra of ten transient metal-containing molecules. The SbH, SbD, TeH, TeD, CdH_2, CdD_2, HZnCl, BeF_2, CoS and SrOD molecules were successfully generated in the laboratory, and their high-resolution spectra were recorded. From the analysis of the spectra, a set of new or improved molecular parameters was obtained for each molecule. These studies are part of continuing projects on metal hydrides, metal halides, transition metal sulfides and alkaline earth monohydroxides in the Bernath laboratory. The motivation for these works will be discussed in detail in the chapters describing each of the molecules.

Molecular spectroscopy is the study of the interaction of light with molecules, which causes molecules to transit from one energy level to another. The energy levels of a molecule are quantized, as governed by the time-independent Schrödinger equation. This chapter provides a brief description on the general theory of molecular energy levels and the selection rules governing molecular transitions, as well as the derivation of molecular parameters from experimental spectra.

1.1 Born-Oppenheimer Approximation

The energy levels of a molecule can be computed in principle by solving the appropriate time-independent Schrödinger equation, $\hat{H}\psi = E\psi$, with the nonrelativistic Hamiltonian given by [1]:

$$\begin{aligned}\hat{H} &= \hat{T}_N + \hat{T}_e + \hat{V}_{NN} \hat{+} \hat{V}_{Ne} + \hat{V}_{ee} \\ &= \frac{-\hbar^2}{2}\sum_\alpha \frac{\nabla_\alpha^2}{M_\alpha} - \frac{\hbar^2}{2m_e}\sum_i \nabla_i^2 \\ &\quad + \sum_\alpha \sum_{\beta>\alpha} \frac{Z_\alpha Z_\beta e^2}{4\pi\varepsilon_0 r_{\alpha\beta}} - \sum_\alpha \sum_i \frac{Z_\alpha e^2}{4\pi\varepsilon_0 r_{\alpha i}} + \sum_i \sum_{j>i} \frac{e^2}{4\pi\varepsilon_0 r_{ij}}\end{aligned} \quad , \qquad (1.1)$$

Where α and β are the indexes for nuclei; i and j are the indexes for electrons. In Eq. (1.1), the first two terms correspond to the nuclear and electronic kinetic energy, respectively; the next three terms describe the contributions to the potential energy that arise from nuclear-nuclear repulsions, the nuclear-electron attractions and the electron-electron repulsions, respectively.

The Coulombic forces acting on the nuclei and on the electrons are similar in magnitude. Because of the large difference between the masses of the nuclei and the electron, the electrons move much faster that the nuclei. As a consequence, the nuclei can be reasonably viewed as "clamped" at fixed positions relative to the motion of the electrons. Under such an approximation, the nuclear kinetic energy in the Hamiltonian operator, Eq. (1.1) can be treated separately. The approximation of neglecting the nuclear motion is called the Born-Oppenheimer approximation. The Born-Oppenheimer approximation will lead to approximate values of the energy and wavefunctions. For most practical purposes, the Born-Oppenheimer approximation is a very good approximation [2]. Neglecting the nuclear kinetic energy in Eq. (1.1) gives the Hamiltonian for the motion of the electrons around the nuclei fixed at various molecular geometries ($\mathbf{r}_\alpha$):

$$\begin{aligned}\hat{H} &= \hat{T}_e + \hat{V}_{NN} \hat{+} \hat{V}_{Ne} + \hat{V}_{ee} \\ &= -\frac{\hbar^2}{2m_e}\sum_i \nabla_i^2 + \sum_\alpha \sum_{\beta>\alpha} \frac{Z_\alpha Z_\beta e^2}{4\pi\varepsilon_0 r_{\alpha\beta}} - \sum_\alpha \sum_i \frac{Z_\alpha e^2}{4\pi\varepsilon_0 r_{\alpha i}} + \sum_i \sum_{j>i} \frac{e^2}{4\pi\varepsilon_0 r_{ij}} \cdot \end{aligned} \tag{1.2}$$

Because the nuclei are considered to be fixed at each particular geometry ($\mathbf{r}_\alpha$), the electronic energy depends parametrically on the positions of the nuclei ($\mathbf{r}_\alpha$). The electronic structure is obtained by solving the electronic equation

$$\hat{H}_{el}\psi_{el} = (\hat{T}_e + \hat{V}_{Ne} + \hat{V}_{ee})\psi_{el} = E_{el}\psi_{el}\,. \tag{1.3}$$

The nuclear-nuclear repulsion term in Eq. (1.2) is a constant as long as nuclei are "clamped", can be added to E_{el} to form the total potential energy

$$U(\mathbf{r}_\alpha) = E_{el}(\mathbf{r}_\alpha) + \hat{V}_{NN}(\mathbf{r}_\alpha)\,, \tag{1.4}$$

where $\mathbf{r}_\alpha$ represents the positions of the nuclei. The separation of the Schrödinger equation into electronic and nuclear motion (vibraton-rotation) parts means that total wavefunction can be approximated as the simple product of electronic and nuclear wavefunctions [1]:

$$\Psi(\mathbf{r}_i, \mathbf{r}_\alpha) \approx \psi_{el}(\mathbf{r}_i, \mathbf{r}_\alpha)\chi_N(\mathbf{r}_\alpha)\,, \tag{1.5}$$

and the following two equations need to be solved:

$$(\hat{H}_{el} + \hat{V}_{NN})\psi_{el}(\mathbf{r}_i, \mathbf{r}_\alpha) = U(\mathbf{r}_\alpha)\psi_{el}(\mathbf{r}_i, \mathbf{r}_\alpha)\,, \tag{1.6}$$

$$(\hat{T}_N + U(r_\alpha))\chi_N(\mathbf{r}_\alpha) = E_N\chi_N(\mathbf{r}_\alpha)\,, \tag{1.7}$$

where $\mathbf{r}_i$ represents the positions of the electrons. Eq. (1.6) is solved to obtain the total electronic energy $U(\mathbf{r}_\alpha)$, which depends parametrically on the particular nuclear positions, $\mathbf{r}_\alpha$. Clamping the nuclei at different positions will result in a different numerical value for $U(\mathbf{r}_\alpha)$ and different wavefunction for $\psi_{el}(\mathbf{r}_i, \mathbf{r}_\alpha)$. The total electronic energy $U(\mathbf{r}_\alpha)$ serves as the potential energy for the nuclear motion and is used in Eq. (1.7) to obtain nuclear vibration-rotation levels.

Molecular orbital theory is the key to solve Eq. (1.6) to obtain the electronic structure [1]. All the molecules studied in this thesis are diatomic or linear triatomic molecules. The electronic Schrödinger

equation (1.6) can be approximately solved by assuming that ψ_{el} is made up of molecular orbitals with each molecular orbital being a linear combination of atomic orbitals. The solution is fairly complicated and only a few topics related to the electronic structure of diatomic molecules are discussed in this chapter. The electronic structure of linear triatomic molecules is similar to that of diatomic molecules.

A specific form of $U(\mathbf{r}_\alpha)$ is needed to derive the vibration-rotation levels of a molecule from Eq. (1.7). However, since $U(\mathbf{r}_\alpha)$ depends in a parametric way on the positions of the nuclei, $\mathbf{r}_\alpha$, no simple analytical expression for $U(\mathbf{r}_\alpha)$ exists in general. $U(\mathbf{r}_\alpha)$ can be numerically calculated using *ab initio* computation packages, or be represented by empirical forms. In this chapter, only the vibration-rotation levels of diatomic and linear triatomic molecules are considered with empirical forms for the potential energy $U(\mathbf{r}_\alpha)$. For diatomic molecules and linear triatomic molecules, Eq. (1.7) can be solved by introducing the spherical polar coordinates r, θ, ϕ and the normal mode coordinates Q_i, respectively [1].

1.2 Vibration-rotation levels of diatomic molecules

In spherical polar coordinates r, θ, ϕ, the Schrödinger equation for the vibration-rotation motion of a diatomic molecule in a $^1\Sigma$ electronic state can be written as [1]:

$$\frac{-\hbar^2}{2\mu}\left[\frac{1}{r^2}\frac{\partial}{\partial r}r^2\frac{\partial\psi}{\partial r}\right]+\frac{1}{2\mu r^2}\hat{J}^2\psi+U(r)\psi=E\psi\,, \tag{1.8}$$

in which μ is the reduced mass of the diatomic molecule A–B, defined as

$$\mu=\frac{m_A m_B}{m_A+m_B}\;; \tag{1.9}$$

$\hat{J}^2$ is the operator representing the square of the angular momentum, defined as

$$\hat{J}^2=-\hbar^2\left[\frac{1}{\sin\theta}\frac{\partial}{\partial\theta}\sin\theta\frac{\partial\psi}{\partial\theta}+\frac{1}{\sin^2\theta}\frac{\partial^2\psi}{\partial\phi^2}\right]. \tag{1.10}$$

Multiplying through by r^2 and rewriting Eq. (1.8), one obtains

$$\left[\frac{-\hbar^2}{2\mu}\frac{\partial}{\partial r}r^2\frac{\partial\psi}{\partial r}+r^2\left[U(r)-E\right]\psi\right]+\left[\frac{1}{2\mu}\hat{J}^2\psi\right]=0\,. \tag{1.11}$$

Notice that in Eq. (1.11), all the r dependence occurs within the left square brackets and all the θ, ϕ dependence within the right square brackets, which suggests that one can use separation of variables and let

$$\psi(r,\theta,\phi)=R(r)Y(\theta,\phi)\,, \tag{1.12}$$

where $Y(\theta,\phi)$ is a spherical harmonic. Substituting this expression gives [2]:

$$\frac{-\hbar^2}{2\mu}\frac{d^2S}{dr^2}+\left(\frac{\hbar^2 J(J+1)}{2\mu r^2}+U(r)\right)S=ES \tag{1.13}$$

where $S(r)=rR(r)$. A specific form is needed for $U(r)$ to solve Eq. (1.13). For diatomic molecules, one of the most common empirical forms for the potential energy of a diatomic molecular was introduced by Dunham [3], and is a Taylor series expansion about the equilibrium internuclear distance, r_e:

$$U(r)=\frac{1}{2}k(r-r_e)^2+\frac{1}{6}k_3(r-r_e)^3+\frac{1}{24}k_4(r-r_e)^4+\cdots\ , \tag{1.14}$$

where k is the second derivative and k_n is the nth derivative of the potential $U(r)$ at r_e. By keeping only the leading term $\frac{1}{2}k(r-r_e)^2$ in Eq.(1.14), one makes the harmonic approximation. For a non-rotating molecule, $J = 0$, the Hamiltonian for the vibrational motion of a diatomic molecule can be written as:

$$\hat{H}=\frac{-\hbar^2}{2\mu}\frac{d^2}{dr^2}+\frac{1}{2}k(r-r_e)^2, \tag{1.15}$$

which is the Hamiltonian for a harmonic oscillator [2]. The eigenvalues are

$$E_{\mathrm{v}}=\hbar\omega(\mathrm{v}+\tfrac{1}{2}) \tag{1.16}$$

where ω is the angular vibrational frequency and v is the vibrational quantum number.

Since the potential energy curve of a real diatomic molecule is always anharmonic, the vibrational energy expression for an anharmonic potential is usually written as:

$$G(\mathrm{v})=\omega_e(\mathrm{v}+\tfrac{1}{2})-\omega_e x_e(\mathrm{v}+\tfrac{1}{2})^2+\omega_e y_e(\mathrm{v}+\tfrac{1}{2})^3+\omega_e z_e(\mathrm{v}+\tfrac{1}{2})^4+\cdots, \tag{1.17}$$

where ω_e, $\omega_e x_e$, $\omega_e y_e$, and $\omega_e z_e$ are called equilibrium vibrational constants.

A zeroth-order representation of the rotational energies of a diatomic molecule is obtained by making the rigid-rotator approximation [1,2]. By assuming the distance between the two atoms A and B is fixed, Eq. (1.8) can be written as

$$\frac{1}{2\mu r^2}\hat{J}^2\psi=E\psi \tag{1.18}$$

with associated eigenvalues [2]:

$$E_J=BJ(J+1)\qquad J=0,1,2,\cdots, \tag{1.19}$$

where B is called rotational constant and J is the rotational angular momentum quantum number. The rotational constant B is related to the moment of inertia I and to the internuclear distance r by [1]:

$$B = \frac{\hbar^2}{2I} = \frac{\hbar^2}{2\mu r^2}, \tag{1.20}$$

where μ is the reduced mass defined in Eq. (1.9).

Since as the molecule rotates, the average internuclear distance increases due to the centrifugal force. The rotational energy expression for real molecules is:

$$F(J) = B_{\mathrm{v}} J(J+1) - D_{\mathrm{v}}[J(J+1)]^2 + H_{\mathrm{v}}[J(J+1)]^3 + \cdots, \tag{1.21}$$

where D is called the centrifugal distortion constant; H is called the high order centrifugal distortion constant. In Eqs. (1.17) and (1.21), all the parameters have the units of cm^{-1}. The rotational constant has vibrational dependence because the average value of $<1/r^2>$ changes as the vibrational quantum number changes. The B and D constants for different vibrational levels can be written as:

$$B_{\mathrm{v}} = B_e - \alpha_e(v+\tfrac{1}{2}) + \gamma_e(v+\tfrac{1}{2})^2 + \cdots, \tag{1.22}$$

$$D_{\mathrm{v}} = D_e + \beta_e(v+\tfrac{1}{2}) + \cdots, \tag{1.23}$$

where B_e, α_e, γ_e, D_e and β_e are called equilibrium rotational constants.

1.3 Vibration-rotation levels of linear triatomic molecules

By defining normal mode coordinates Q_i and by making the harmonic approximation, the Hamiltonian for the vibratonal motion of a linear polyatomic molecule with N atoms is given by [1]:

$$\hat{H} = \sum_{i=1}^{3N-5} \left(-\frac{\hbar^2}{2}\frac{\partial^2}{\partial Q_i^2} + \frac{1}{2}\lambda_i Q_i^2\right). \tag{1.24}$$

The sum is over $3N$-5 normal mode coordinates because there is no restoring force acting on five of the degrees of freedom, which are associated with the translation of the center of mass (x, y, z) and the rotation of the molecule as a whole (θ, ϕ), and their vibrational frequencies are zero. In the normal mode coordinates, the kinetic and potential energy terms have no cross-terms connecting different coordinates. The Hamiltonian operator is just a sum of $3N$-5 independent harmonic oscillator Hamiltonian operators. The total energy is thus the sum of $3N$-5 harmonic oscillator energies,

$$E = \sum \hbar\omega_i(\mathrm{v}_i + \tfrac{1}{2}) \ . \tag{1.25}$$

For linear triatomic molecules, there are $3N$-5 = 4 vibrational modes. Since the molecule can bend in plane or out of plane, linear triatomic molecules have a doubly degenerate bending mode. The vibrational modes for linear triatomic molecules are labeled as ν_1, ν_2 and ν_3 with ν_2 being a doubly degenerate bending mode. When anharmonic terms are included in the potential, the following vibrational energy expression is obtained for linear triatomic molecules:

$$G(\mathrm{v}_1, \mathrm{v}_2^l, \mathrm{v}_3) = \omega_1(\mathrm{v}_1 + \tfrac{1}{2}) + \omega_2(\mathrm{v}_1 + 1) + \omega_3(\mathrm{v}_3 + \tfrac{1}{2}) + x_{11}(\mathrm{v}_1 + \tfrac{1}{2})^2 + x_{22}(\mathrm{v}_2 + 1)^2 + x_{33}(\mathrm{v}_3 + \tfrac{1}{2})^2 + g_{22}l^2 + x_{12}(\mathrm{v}_1 + \tfrac{1}{2})(\mathrm{v}_2 + 1) + x_{13}(\mathrm{v}_1 + \tfrac{1}{2})(\mathrm{v}_3 + \tfrac{1}{2}) + x_{23}(\mathrm{v}_2 + 1)(\mathrm{v}_3 + \tfrac{1}{2}) \quad , \qquad (1.26)$$

where v_1, v_2 and v_3 are the vibrational quantum numbers for the ν_1, ν_2 and ν_3 modes, respectively; ω_1, ω_2 and ω_3 are the harmonic vibrational frequencies; the term (v_2+1) appears for bending mode because each oscillator of the doubly degenerate pair contributes $\omega_2/2$ of zero-point energy; l is a new quantum number for the vibrational angular momentum [1]. The vibrational angular momentum is associated with the bending mode ν_2, and the possible values for l are v_2, v_2–2,…, 0 or 1.

The rotational energy for linear triatomic molecule is expression as a power series in $[J(J+1)-l^2]$:

$$F(J) = B_\mathrm{v}\left[J(J+1)-l^2\right] - D_\mathrm{v}[J(J+1)-l^2]^2 + H_\mathrm{v}[J(J+1)-l^2]^3 + \cdots, \qquad (1.27)$$

and the vibrational dependence of the rotational constant is given by

$$B_\mathrm{v} = B_e - \alpha_1(\mathrm{v}_1 + \tfrac{1}{2}) - \alpha_2(\mathrm{v}_2 + 1) - \alpha_3(\mathrm{v}_3 + \tfrac{1}{2}). \qquad (1.28)$$

The rotational constant B is related to the moment of inertia I by [1]:

$$B = \frac{\hbar^2}{2I}, \qquad (1.29)$$

where the moment of inertia

$$I = (\frac{1}{M})(m_1 m_2 r_{12}^2 + m_1 m_3 r_{13}^2 + m_2 m_3 r_{23}^2), \qquad (1.30)$$

for a linear triatomic molecule made of atoms with masses m_1, m_2 and m_3 and nuclear distances r_{12}, r_{13} and r_{23} [1]. In Eq. (1.30), M is the total mass of the molecule.

1.4 Electronic states of diatomic molecules

For a diatomic molecule, the total angular momentum (exclusive of nuclear spin) is the vector sum of total electron orbital $\hat{\mathbf{L}}$, total electron spin $\hat{\mathbf{S}}$, and the nuclear rotation $\hat{\mathbf{R}}$ angular momenta. The orbital angular momenta of all electrons are coupled to give $\hat{\mathbf{L}}$, and the spin of all electrons are coupled to give $\hat{\mathbf{S}}$. The notation for the angular momenta and their projections on the intermolecular axis is summarized in Figure 1.1 and Table 1.1.

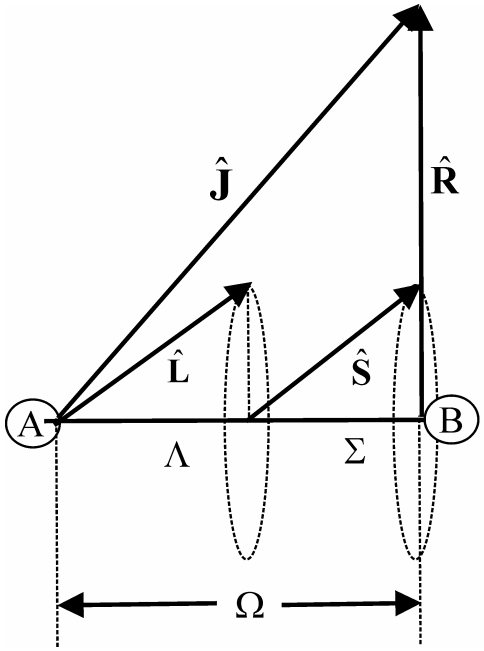

Figure 1.1 Angular momenta in a diatomic molecule.

Table 1.1 Angular momenta in diatomic molecules

Angular Momentum	Projection on Molecular Axis (units of $\hbar$)
$\hat{\mathbf{J}}$	$\Omega = (\Lambda + \Sigma)$
$\hat{\mathbf{L}}$	Λ
$\hat{\mathbf{S}}$	Σ
$\hat{\mathbf{R}}$	–
$\hat{\mathbf{N}} = \hat{\mathbf{R}} + \hat{\mathbf{L}}$	Λ

The term symbol ${}^{2S+1}\Lambda$ is used to denote the electronic state of a diatomic molecule: $\Lambda = 0$ is called a Σ state, $\Lambda = 1$ called a Π state and $\Lambda = 2$ called a Δ state; $(2S+1)$ is called the spin multiplicity and $(2S+1) = 1$ is called a singlet state, $(2S+1) = 2$ is called a doublet state and $(2S+1) = 3$ is called a triplet state. The superscript + or – is used on the ${}^{2S+1}\Sigma^{+}$ and ${}^{2S+1}\Sigma^{-}$ symbols to distinguish between the effect of the reflection operator $\hat{\sigma}_v$ on the electronic wavefunctions, $\hat{\sigma}_v \psi_{el} = \pm\psi_{el}$. For doubly degenerate electronic wavefunctions Π, Δ, Φ and so on, there is no point in writing $\Pi^{\pm}$, $\Delta^{\pm}$ since one component can always be labeled + while the other can be labeled –.

The electronic states of diatomic molecules are also labeled with letters. *X* is reserved for the ground state. Capital case letters *A*, *B*, *C* … are used, in order of increasing energy, for excited states with the same multiplicity (2*S*+1) as the ground state while lower case letters *a*, *b*, *c* … are used for excited states with a different multiplicity.

The simplest electronic state is a $^1\Sigma^+$ or $^1\Sigma^-$ ($\Lambda = 0$, $\Sigma = 0$) state for closed-shell molecules with no unpaired electrons. The energy level expression for $^1\Sigma$ states is:

$$E_{vJ} = T_e + G_v + F(J), \tag{1.31}$$

where T_e is the electronic energy, which is a constant here; G_v is the vibrational energy (Eq. (1.17)); $F(J)$ is the rotational energy (Eq. (1.21)).

For electronic states with $\Lambda>0$, e.g., $^1\Pi$, $^1\Delta$, $^1\Phi$, the circulation of electrons can be in a clockwise or counterclockwise direction around the internuclear axis, which results in a double orbital degeneracy called Λ-doubling. As the molecule begins to rotate, this degeneracy is lifted. The energy level expression for $^1\Pi$, $^1\Delta$, $^1\Phi$ states and so forth is:

$$E_{vJ} = T_e + G_v + F(J) \pm \tfrac{1}{2}[q_v J(J+1) + q_{Dv}[J(J+1)]^2 + \cdots], \tag{1.32}$$

where q and q_D are Λ-doubling constants.

For electronic states with unpaired electrons (nonsinglet states), the electronic structure is more complicated. The electrons have magnetic moments and move in orbitals around the nuclei, which will create magnetic fields. The electron magnetic moments interact with each other, with the orbital magnetic fields, and with the small magnetic field created by nuclear rotation: these interactions are called spin-spin ($\hat{\mathbf{S}}\cdot\hat{\mathbf{S}}$), spin-orbit ($\hat{\mathbf{L}}\cdot\hat{\mathbf{S}}$) and spin-rotation ($\hat{\mathbf{N}}\cdot\hat{\mathbf{S}}$) interactions, respectively. The energy levels of nonsinglet states are obtained by the addition of the spin-orbit, spin-spin and spin-rotation operators, and the Hamiltonian becomes,

$$\hat{H}_{eff} = \hat{T}_e + \hat{H}_{\text{vib}} + \hat{H}_{\text{rot}} + \hat{H}_{\text{spin-orbit}} + \hat{H}_{\text{spin-spin}} + \hat{H}_{\text{spin-rotation}} + \hat{H}_{LD}, \tag{1.33}$$

where

$$\hat{H}_{\text{spin-orbit}} = \mathrm{A}\hat{\mathbf{L}}\cdot\hat{\mathbf{S}}, \tag{1.34}$$

$$\hat{H}_{\text{spin-spin}} = \tfrac{2}{3}\lambda(3\hat{\mathbf{S}}_z^2 - \hat{\mathbf{S}}^2), \tag{1.35}$$

$$\hat{H}_{\text{spin-rotation}} = \gamma\,\hat{\mathbf{N}}\cdot\hat{\mathbf{S}}, \tag{1.36}$$

and $\hat{H}_{LD}$ describes the Λ-doubling which gives rise to the ± terms in Eq. (1.32) for $^1\Pi$, $^1\Delta$, $^1\Phi$ states and ± terms in different forms for other states.

The energy level pattern of nonsinglet electronic states depends on the size of the spin-orbit coupling term, $\mathrm{A}\hat{\mathbf{L}}\cdot\hat{\mathbf{S}}$, or the spin-spin coupling term, $\lambda(3\hat{\mathbf{S}}_z^2 - \hat{\mathbf{S}}^2)$. For example, there are two common cases for a $^2\Pi$ state. When *A* is large, it is referred to as Hund's case (a) coupling and the $^2\Pi$ state is split into two well-separated spin components, $^2\Pi_{1/2}$ and $^2\Pi_{3/2}$. When *A* is small, it is called Hund's case (b) coupling and the two spin components lie very close to each other.

Under Hund's case (a) coupling, the spin-orbit interaction will split states with $\Lambda > 0$ into $(2S+1)$ spin components. The symbol ${}^{2S+1}\Lambda_{|\Omega|}$ is used to denote these spin components. For example, a $^2\Pi$ state ($\Lambda = 1$, $\Sigma = \pm 1/2$) has $^2\Pi_{1/2}$ and $^2\Pi_{3/2}$ spin components. In case of $S > |\Lambda| > 0$, the labeling of each spin component becomes difficult and $\Omega = |\Lambda| + \Sigma$ is used instead of $|\Omega| = |\Lambda + \Sigma|$, e.g., a $^4\Pi$ state has $^4\Pi_{5/2}$, $^4\Pi_{3/2}$, $^4\Pi_{1/2}$, $^4\Pi_{-1/2}$ spin components. Hund's case (a) coupling is not common for Σ states, since the spin-orbit term $A\hat{\mathbf{L}}\cdot\hat{\mathbf{S}}$ is zero. Hund's case (a) coupling may apply to Σ states with a large spin-spin interaction, which can split ${}^{2S+1}\Sigma$ states into $(S+1)$ spin components. For example, a Hund's case (a) $^3\Sigma$ state ($\Lambda = 0$, $\Sigma = \pm 1, 0$) has $^3\Sigma_1$ and $^3\Sigma_0$ spin components.

In some cases, the spin-orbit and spin-spin interactions become so large that the $(2S+1)$ or $(S+1)$ spin components are widely separated. The various spin components from several ${}^{2S+1}\Lambda$ terms can occur at the same energy, and their wavefunctions become mixed. This case is referred to as Hund's case (c) coupling. For Hund's case (c) coupling, the spin components of a given ${}^{2S+1}\Lambda$ term are like independent electronic states, and the energy levels for each of the spin components can simply be approximated as:

$$E_{vJ} = T_e + G_v + F_J \pm \tfrac{1}{2}[p_v(J+\tfrac{1}{2}) + p_{Dv}(J+\tfrac{1}{2})^3 + p_{Hv}(J+\tfrac{1}{2})^5 + \cdots], \qquad (1.37)$$

where p_v, p_{Dv} and p_{Hv} are called Ω-doubling constants and the lowest order Ω-doubling splitting increases as $J^{2\Omega}$ for half integer Ω or by Eq. (1.32) for integer Ω.

Hund's case (c) coupling only applies to a few heavy molecules. The most common coupling cases are Hund's case (a) and Hund's case (b). Under these coupling cases, different ${}^{2S+1}\Lambda$ states lie far from each other but the spin components from one ${}^{2S+1}\Lambda$ state lie close to each other and may couple with each other. The energy levels of molecules are calculated by diagonalizing the Hamiltonian matrix with off-diagonal matrix elements accounting for the coupling between the spin components.

In this thesis, the usual $\hat{N}^2$ ($\hat{N}^2 = (\hat{J} - \hat{S})^2$) effective Hamiltonian from Brown [4,5] was used. Details on the derivation of an effective Hamiltonian can be found in Refs. [4,5]. In summary, the Hamiltonian operator $\hat{H}$ (Eq. (1.33)) is subjected to a succession of contact or Van Vleck transformations to remove terms coupling different vibronic states. When necessary, a rotational contact transformation is performed to remove redundant terms that could cause interdeterminancies among the molecular parameters [4]. In terms of $\hat{N}^2$ ($\hat{N}^2 = (\hat{J} - \hat{S})^2$), the effective Hamiltonian is given by [4]

$$\begin{aligned}\hat{H}_{eff} &= T_e + G_v + B_v\hat{N}^2 - D_v\hat{N}^4 + \tfrac{1}{2}[A_v + A_{Dv}\hat{N}^2, \hat{L}_z\hat{S}_z]_+ \\ &\quad + [\lambda_v + \lambda_{Dv}\hat{N}^2, \hat{S}_z^2 - \tfrac{1}{3}\hat{S}^2]_+ + (\gamma_v + \gamma_{Dv}\hat{N}^2)\hat{N}\cdot\hat{S} \\ &\quad + \hat{H}_{LD}\end{aligned} \qquad (1.38)$$

where the $[,]_+$ indicate anticommutators; the Λ-doubling term $\hat{H}_{LD}$ has different forms for Π, Δ, … states, which has been explained in Refs. [4,6] and is not listed here.

Basis functions are needed to derive matrix elements for electronic states. Usually the energy level expressions are calculated in Hund's case (a) basis $\left|\Lambda S\Sigma J\Omega\right\rangle$ because the matrix elements are algebraically simpler. The *e/f* parity basis functions $\left|J\Omega\pm\right\rangle$ are used instead of $\left|\Lambda S\Sigma J\Omega\right\rangle$:

$$\left|J\Omega\pm\right\rangle = \tfrac{1}{\sqrt{2}}\left[\left|\Lambda S\Sigma J\Omega\right\rangle \pm \left|-\Lambda, S, -\Sigma, J, -\Omega\right\rangle\right]. \tag{1.39}$$

By introducing the ladder operators,

$$J_{\pm} = J_x \pm iJ_y, S_{\pm} = S_x \pm iS_y, \tag{1.40}$$

$$J_{\pm}\left|\Lambda S\Sigma J,\Omega\right\rangle = \hbar\sqrt{J(J+1)-\Omega(\Omega\mp 1)}\left|\Lambda S\Sigma J,\Omega\mp 1\right\rangle, \tag{1.41}$$

$$S_{\pm}\left|\Lambda S,\Sigma,J\Omega\right\rangle = \hbar\sqrt{J(J+1)-\Sigma(\Sigma\pm 1)}\left|\Lambda S,\Sigma\pm 1,J\Omega\right\rangle, \tag{1.42}$$

the Hamiltonian matrix for the case (a) basis set can be derived for any electronic state.

For example, for $^2\Pi$ states, the effective Hamiltonian is

$$\begin{aligned}\hat{H}_{eff} &= T_e + G_{\rm v} + B_{\rm v}\hat{N}^2 - D_{\rm v}\hat{N}^4 + \tfrac{1}{2}[A_{\rm v} + A_{D\rm v}\hat{N}^2, \hat{L}_z\hat{S}_z]_+ \\ &\quad + (\gamma_{\rm v} + \gamma_{D\rm v}\hat{N})\hat{N}\cdot\hat{S} + \hat{H}_{LD}\end{aligned}. \tag{1.43}$$

There is no spin-spin interaction in $^2\Pi$ states, since there is only one unpaired electron. There are four possible case (a) functions for $^2\Pi$ states:

$$\left|{}^2\Pi_{3/2}\right\rangle = \left|\Lambda=1, S=\tfrac{1}{2}, \Sigma=\tfrac{1}{2}, J, \Omega=\tfrac{3}{2}\right\rangle, \tag{1.44}$$

$$\left|{}^2\Pi_{1/2}\right\rangle = \left|\Lambda=1, S=\tfrac{1}{2}, \Sigma=-\tfrac{1}{2}, J, \Omega=\tfrac{1}{2}\right\rangle, \tag{1.45}$$

$$\left|{}^2\Pi_{-1/2}\right\rangle = \left|\Lambda=-1, S=\tfrac{1}{2}, \Sigma=\tfrac{1}{2}, J, \Omega=-\tfrac{1}{2}\right\rangle, \tag{1.46}$$

$$\left|{}^2\Pi_{-3/2}\right\rangle = \left|\Lambda=-1, S=\tfrac{1}{2}, \Sigma=-\tfrac{1}{2}, J, \Omega=-\tfrac{3}{2}\right\rangle. \tag{1.47}$$

The *e/f* parity basis functions can be written as:

$$\left|{}^2\Pi_{3/2}(e/f)\right\rangle = \frac{\left|{}^2\Pi_{3/2}\right\rangle \pm \left|{}^2\Pi_{-3/2}\right\rangle}{\sqrt{2}}, \tag{1.48}$$

$$\left|{}^2\Pi_{1/2}(e/f)\right\rangle = \frac{\left|{}^2\Pi_{1/2}\right\rangle \pm \left|{}^2\Pi_{-1/2}\right\rangle}{\sqrt{2}}. \tag{1.49}$$

The Hamiltonian matrix in this basis set is a 2×2 matrix with

$$H_{11} = \left\langle {}^2\Pi_{3/2}(e/f)\middle|\hat{H}_{eff}\middle|{}^2\Pi_{3/2}(e/f)\right\rangle, \tag{1.50}$$

$$H_{22} = \left\langle {}^2\Pi_{1/2}(e/f)\middle|\hat{H}_{eff}\middle|{}^2\Pi_{1/2}(e/f)\right\rangle, \tag{1.51}$$

$$H_{12} = H_{21} = \left\langle {}^2\Pi_{3/2}(e/f) \middle| \hat{H}_{eff} \middle| {}^2\Pi_{1/2}(e/f) \right\rangle . \quad (1.52)$$

The derivation of the coefficients and multiplicative factors is available in Ref. [1] (for *B*, *D* and *A)* and in Ref. [4] (for Λ-doubling constants *p* and *q*). An explicit listing of these matrix elements is provided by Amiot *et al*. [7] and, for convenience, Table 1.2 lists these coefficients and multiplicative factors. Please note that the spin-rotation constant γ can not be determined simultaneously with the A_D constant, and therefore is ignored.

Figure 1.2 shows the energy level diagram for $^2\Pi$ states. Notice that each level in Figure 1.2 is labeled by quantum numbers *J*, *e/f* and +/–. The last two are called rotationless parity and total parity, respectively. Several different types of parity are used in molecular spectroscopy, and are well explained in Ref. [1]. Here only *e/f* parity is mentioned, which is the most convenient to use. The total parity changes sign with *J* (Figure 1.2), and the rotationless *e/f* parity is defined for integer *J* as:

$$\hat{E}^* \psi = +(-1)^J \psi \qquad \text{for } e \quad (1.53)$$

$$\hat{E}^* \psi = -(-1)^J \psi \qquad \text{for } f \quad (1.54)$$

where $\hat{E}^*$ is the inversion operator and ψ is the total wavefunction ($\psi = \psi_{el}\psi_{vib}\psi_{rot}$). For half-integer *J*, *J*-1/2 is used instead of *J* in Eq. (1.53) and Eq. (1.54).

The matrix elements for other electronic states can be obtained in a similar way. The matrix elements and energy diagrams for electronic states studied in this thesis will be listed in the relevant chapters.

Table 1.2 Coefficients and multiplicative factors of the matrix elements of $^2\Pi$ states in Hund's case (a) basis functions using the usual $\hat{N}^2$ Hamiltonian.[a]

Constants	H_{11} [b]	H_{12}	H_{22} [c]
G_v	1	0	1
A_v	0.5	0	-0.5
A_{Dv}	0.5x	0	-0.5(x+2)
A_{Hv}	x^2	$-(x+2)^2$	$x^{1/2}$
B_v	x	$-x^{1/2}$	x+2
D_v	-x(x+1)	$2x^{1/2}(x+1)$	-(x+1)(x+4)
H_v	x(x+1)(x+2)	$-x^{1/2}(x+1)(3x+4)$	$(x+1)(x^2+8x+8)$
p_v	0	0	$\pm 0.5(J+0.5)$
p_{Dv}	0	$\pm 0.25x^{1/2}(J+0.5)$	$\pm 0.5(J+0.5)(x+2)$
p_{Hv}	0	$\pm 0.5x^{1/2}(J+0.5)^3$	$\pm 0.5(J+0.5)^3(x+4)$
q_v	0	$\pm 0.5x^{1/2}(J+0.5)$	$\pm 0.5(J+0.5)$
q_{Dv}	$\pm 0.5x(J+0.5)$	$\pm 0.5x^{1/2}(x+2)(J+0.5)$	$\pm 0.5(3x+4)(J+0.5)$

[a] x = (*J*-0.5)(*J*+1.5).When two signs are quoted, the upper is for *e* levels and the lower for *f* levels.
[b] Matrix elements for $^2\Pi_{3/2}$.
[c] Matrix elements for $^2\Pi_{1/2}$.

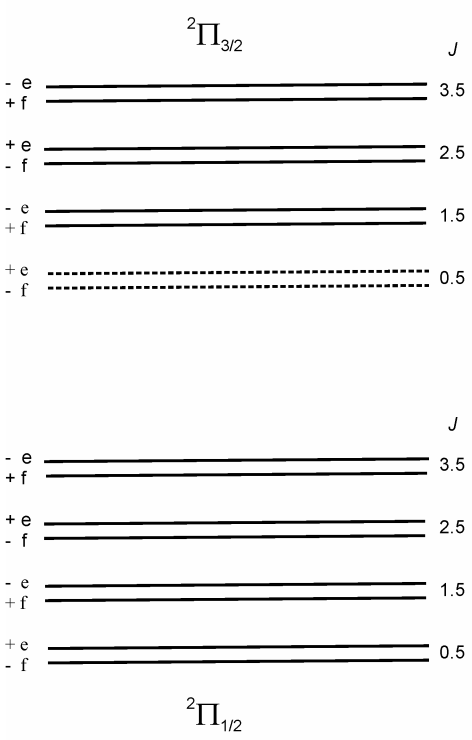

Figure 1.2 Energy level diagram of a Hund's case (a) $^2\Pi$ state. Each level is labeled by quantum number *J*, rotationless (*e*/*f*) parity and total (+/-) parity. Each rotational level is split into a doublet due to Λ-doubling. The *J* = 0.5 levels of the $^2\Pi_{3/2}$ spin component are dashed because the *J* quantum number starts from the value of Ω for each $^{2S+1}\Lambda_\Omega$ spin component.

1.5 Perturbations

When two energy levels lie close to each other, they will interact with each other through the mixing of their wavefunctions, as long as the following selection rules are not violated:

$$\Delta J = 0, e \leftrightarrow e \text{ or } f \leftrightarrow f,\ g \leftrightarrow g \text{ or } u \leftrightarrow u.$$

This interaction is called a perturbation, and it will push the energy levels involved away from each other. In this case, the molecular models introduced in Section 1.4 will be unable to describe the perturbed levels, and the following modified Hamiltonian matrix will be required to account for the perturbation:

$$H = \begin{pmatrix} H_1^0 & V \\ V & H_2^0 \end{pmatrix}, \tag{1.55}$$

where $\hat{H}_1^0$ and $\hat{H}_2^0$ are the unperturbed Hamiltonian matrixes and the off-diagonal term V connects the two perturbed states. Perturbations were observed for TeH, CdH_2, BeF_2 and CoS, and will be discussed in detail later in the chapters on those molecules.

1.6 Selection rules

The transitions studied in this thesis can be classified into three categories: vibration-rotation transitions of diatomic molecules; vibration-rotation transitions of linear triatomic molecules in $^1\Sigma^+$ states; electronic transitions of diatomic and linear triatomic molecules. The derivation of selection rules for these transitions is explained in Ref. [1]. These rules are listed here for convenience.

The selection rules for vibration-rotation transitions of diatomic molecules are:

(1) $\Delta J = \pm 1, e \leftrightarrow e \text{ or } f \leftrightarrow f$ for $^1\Sigma^+$ or $^1\Sigma^-$ states. *P* and *R* branches are possible for molecules with no net spin or orbital angular momentum ($^1\Sigma$ states).

(2) $\Delta J = \pm 1, e \leftrightarrow e, f \leftrightarrow f \text{ or } \Delta J = 0, e \leftrightarrow f$ for states other than $^1\Sigma^+$ states. Weak *Q* branches are also possible for free radicals in which $\hat{\mathbf{L}}$ or $\hat{\mathbf{S}}$ are non-zero.

The selection rules for vibration-rotation transitions of linear triatomic molecules in $^1\Sigma^+$ states are:

(1) $\Delta l = 0$ with $l = 0$. This is a parallel transition of the Σ^+–Σ^+ type with *P* and *R* branches ($\Delta J = \pm 1, e \leftrightarrow e, f \leftrightarrow f$).

(2) $\Delta l = 0$ with $l \neq 0$. This is also a parallel transition such as Π–Π and Δ–Δ, with strong *P* and *R* branches and weak *Q* branches ($\Delta J = \pm 1, e \leftrightarrow e, f \leftrightarrow f \text{ or } \Delta J = 0, e \leftrightarrow f$).

(3) $\Delta l = \pm 1$. This is a perpendicular transition such as Π–Σ and Δ–Π, with *P* and *R* branches and strong *Q* branches ($\Delta J = \pm 1, e \leftrightarrow e, f \leftrightarrow f \text{ or } \Delta J = 0, e \leftrightarrow f$).

The selection rules for electronic transitions of diatomic and linear triatomic molecules for Hund's case (a) and case (b) coupling are:

(1) $\Delta\Lambda = 0, \pm 1$. Transitions such as Σ–Σ, Π–Π, Π–Σ and Π–Σ are allowed.

(2) Σ^+–Σ^+ and Σ^-–Σ^- but not Σ^+–Σ^-.

(3) $\Delta S = 0$. Transitions that change spin multiplicity are very weak.

(4) $\Delta\Sigma = 0$. Cross spin component transitions are very weak if spin-orbit constants are large.
(5) $\Delta\Omega = 0, \pm 1$.
(6) $g \leftrightarrow u$ for centrosymmetric molecules.

For pure Hund's case (c) coupling, S, Λ and Σ no longer have any meaning; only J and Ω are good quantum numbers [1]. The selection rules for electronic transitions of diatomic and linear triatomic molecules for Hund's case (c) are: $\Delta\Omega = 0, \pm 1$, and $g \leftrightarrow u$ for centrosymmetric molecules.

1.7 Least-squares fitting of spectroscopic data

With molecular energy level models derived from Sections 1.2, 1.3 and 1.4, known molecular constants, and selection rules listed in Section 1.6, one can calculate the line positions (the spectrum) for allowed molecular transitions. In reverse, one can obtain molecular constants by fitting the experimental spectrum with molecular energy level models. In this thesis, high-resolution spectra of ten transient metal-containing molecules were obtained from experiment and were fitted to molecular models using a non-linear least-squares fitting procedure, and a set of experimental molecular parameters was obtained for each molecule.

In the fitting, the dimensionless standard error σ is used to represent the ability of a set of molecular parameters to reproduce the experimental line positions [8]:

$$\sigma = \left\{ \frac{1}{N-M} \sum_{i=1}^{N} \left[\frac{y_{\text{calc}}(i) - y_{\text{obs}}(i)}{u(i)} \right]^2 \right\}^{1/2} \tag{1.56}$$

where N is the number of experimental data and M is the number of parameters; $y_{\text{obs}}(i)$ is an observed line position with an experimental uncertainty of $u(i)$; $y_{\text{calc}}(i)$ is the line position predicted by the model. If the experimental uncertainties are appropriate, a good quality fit should have a σ value of about than 1, which means that on average, the predictions of the model differ from the input data by the associated experimental uncertainties. σ can be used to guide the fitting procedure, e.g., one knows something is not right when a large value of σ is obtained.

The spectroscopic parameters are usually rounded when they are reported. If all parameters are rounded as suggested by the statistical errors, the σ value increases notably. Therefore, it is customary to report one extra digit for spectroscopic parameters.

1.8 Molecular structures

One of the main applications of molecular spectroscopy is the determination of molecular structures. The bond lengths of diatomic molecules can be simply determined from the moments of inertia (Eq. (1.20)). Due to the vibration and rotation of a molecule, each vibrational level has a different value of B_v (Eq. (1.22)); therefore there are many corresponding r_v values. The r_e structure is called the equilibrium structure, which corresponds to the bottom of the potential well where the atoms are at rest. Given at least B_0 and B_1, r_e can be computed by using Eqs. (1.22) and (1.20).

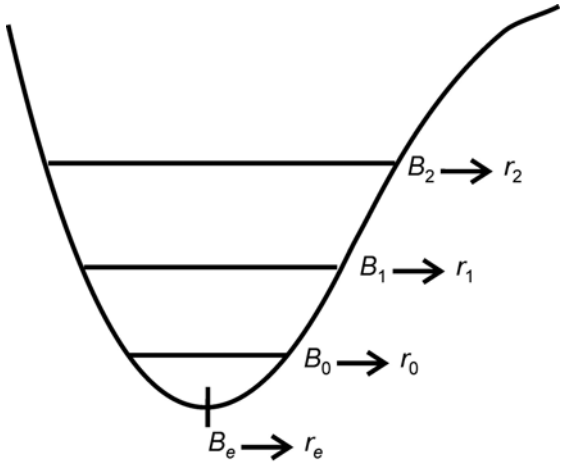

Figure 1.3 B_v and r_v values for diatomic molecules.

The determination of bond lengths for linear triatomic molecules is more difficult. Only one moment of inertia can be experimentally determined for a linear triatomic molecule, but usually two bond lengths need to be determined (Eq. (1.30)). This problem can be solved by making use of data from isotopic molecules and by making the assumption that all the isotopic molecules have the same structure. In this thesis, the r_0 bond lengths of SrOH were derived by using the B_0 values of SrOH and SrOD (see Chapter 6).

The r_e structure is generally considered to be the "best" structure [1]. In case that the r_e structure can not be determined, the r_0 structure is still useful, although r_0 structures have proved to be not very reliable [1]. A "better" structure (i.e., closer to the equilibrium structure) is the r_s structure, which can de derived by using Kraichman's equations [9]. In this thesis, single isotopic substitution procedure was used to determine the r_s Zn-Cl bond length for HZnCl, and multiple isotopic substitution procedure was used to derive the r_s structure of CdH_2. The equations used for these two molecules will be listed in the chapters on those two molecules.

1.9 References

[1] P.F. Bernath, *Spectra of Atoms and Molecules*, 2nd ed., Oxford University Press, New York (2005).

[2] D.A. McQuarrie and J. D. Simon, *Physical Chemistry, a Molecular Approach*, University Science Books, California (1997).

[3] J.L. Dunham, Phys. Rev. **41,** 721 (1932).

[4] J.M. Brown, E.A. Colbourn, J.K.G. Watson and F.D. Wayne, J. Mol. Spectrosc. **74,** 294 (1979).

[5] J. M. Brown and A. Carrington, *Rotational Spectroscopy of Diatomic Molecules*, Cambridge University Press, Cambridge (2003).

[6] J.M. Brown, A.S-C. Cheung and A.J. Merer, J. Mol. Spectrosc. **124,** 464 (1987).

[7] C. Amiot, J.-P. Maillard, J. Chauville, J. Mol. Spectrosc. **87,** 196 (1981).

[8] R.J. Le Roy, J. Mol. Spectrosc. **191,** 223 (1998).

[9] W. Gordy, R.L Cook, *Microwave Molecular Spectra*, Interscience Publishers, New York, 1970.

Chapter 2

Experimental

2.1 Gas phase molecule synthesis sources

Three types of gas phase molecule synthesis sources were used to generate the molecules studied in this thesis: 1) an discharge-furnace emission source that combines a high temperature furnace with an electrical discharge was used to generate the SbH, SbD, TeH, TeD, CdH_2, CdD_2, HZnCl and BeF_2 molecules; 2) a King furnace (carbon tube furnace) was used to synthesize the CoS molecule; 3) a Broida-type oven (metal flow reactor) was used to generate the SrOD molecule.

2.1.1 Discharge-furnace emission source

The Bernath group has a very good system to investigate spectra of gaseous metal hydrides: an emission source that combines a high temperature tube furnace with an electrical discharge. A schematic diagram of the discharge-furnace emission source is given in Figure 2.1.

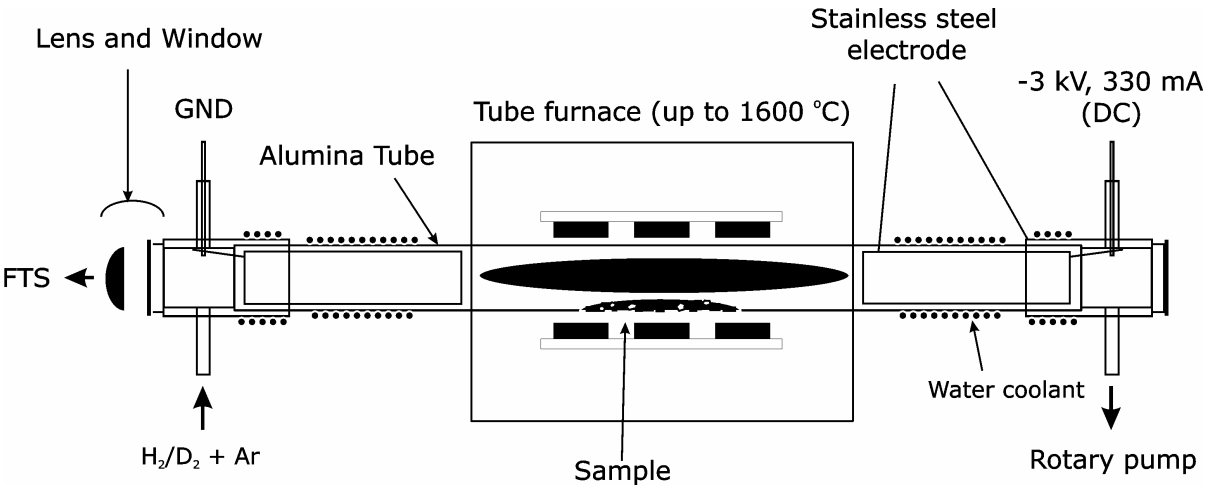

Figure 2.1 A diagram of the discharge-furnace emission source in the Bernath laboratory.

An alumina tube (5 cm × 120 cm) was placed inside a tube furnace, which can be heated up to 1600°C depending on the experiment. The metals (Sb, Te, Zn or Cd) were place in the center of the alumina tube and heated to produce about of 1 Torr metal vapor pressure. (The temperatures to which these metals were heated to produce 1 Torr of vapor pressure were calculated using the equations in Ref. [1].) A mixture of 1 to 3 Torr hydrogen or deuterium and 2 Torr Ar was flowed slowly through the alumina tube. For the experiments on HZnCl, pure HCl gas was used. The mixture of gases was

then exposed to the discharge, which was generated by applying a 3 kV/330 mA dc power supply to the two stainless-steel tube electrodes located inside the ends of the alumina tube. The discharge is very critical in the generation of metal hydrides and hydrochlorides, and provides the energy needed to overcome the reaction barrier. The two ends of the alumina tube were cooled from outside by a constant flow of cold water. When synthesized in this emission source, the molecules have population in excited states, and they relax to the ground state by emitting infrared and visible radiation. This radiation was focused by a CaF_2 or BaF_2 lens into the entrance aperture of a Bruker IFS 120 HR Fourier transform spectrometer.

2.1.2 Carbon tube furnace (King furnace)

The discharge-furnace emission source has proved to be an excellent source for spectroscopy of metal hydrides. Molecules other than metal hydrides, however, are very difficult to generate in the discharge-furnace emission source. One reason for this is that the electrodes become contaminated rapidly, and the discharge becomes unstable. In addition, the highest temperature that the discharge-furnace emission source can achieve is 1600°C. Some metals have to be heated to over 1600°C in order to produce 1 Torr of metal vapor pressure. For example, Co has to be heated to 2000°C to produce 1 Torr of vapor pressure. One solution to this problem is to use a carbon tube furnace (King furnace), which is one of the oldest tools for gas phase spectroscopy and was introduced by Arthur King in 1908 [2]. A schematic diagram of the King furnace in the Bernath laboratory is given in Figure 2.2.

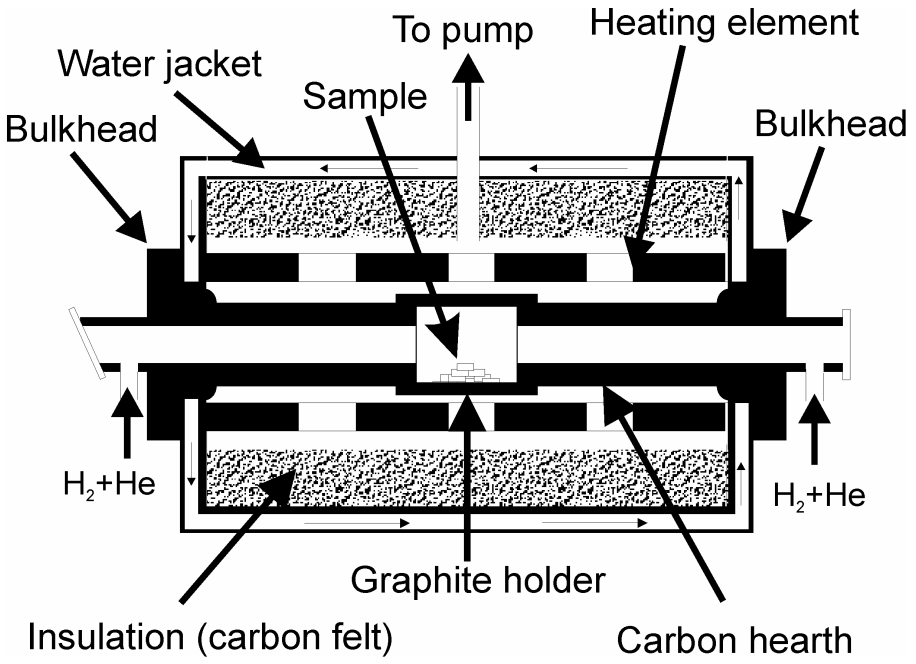

Figure 2.2 A schematic diagram of the King furnace in the Bernath laboratory.

The furnace shell is a water cooled jacket made from anodized aluminum. Everything inside the shell is made of carbon. The essential component of the furnace is the graphite heating element through which currents up to 60 A can flow. The temperatures inside the furnace can reach to 2700^{o}C, depending on the experimental conditions such as the applied current and the operating gas. The heating element is thermally insulated from the furnace shell by carbon felt. Two carbon hearths (tubes) are connected to the two bulkheads by threads and placed coaxially to the heating element. Attached to the ends of the two carbon hearths is a graphite holder that is used to hold the sample. The King furnace needs at least 100 Torr of operating gas (He), and the total pressure inside the King furnace is usually held at 200 Torr when spectra are recorded.

2.1.3 Broida oven

A flow reactor called a Broida oven was introduced in 1974 by West *et al*. [3] to produce diatomic metal oxides and halides. The Broida oven is a relatively cool (~500 K) and low-pressure (~5 Torr) source. Harris and co-workers [4,5] discovered that alkaline earth monohydroxides could be made easily in the Broida oven. A schematic diagram of the Broida oven in the Bernath laboratory is given in Figure 2.3.

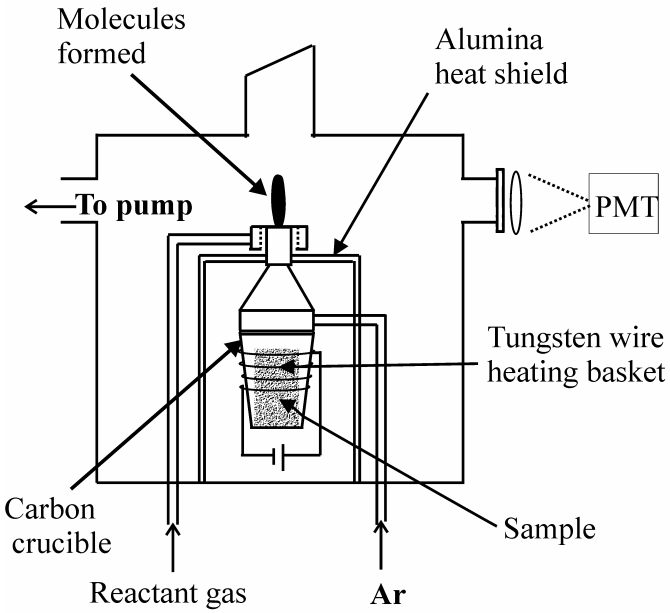

Figure 2.3 A schematic diagram of the Broida oven in the Bernath laboratory

The essential component of a Broida oven is a tungsten wire heating basket through which current can flow. Metals are heated in a carbon crucible placed in the tungsten basket to produce metal vapors. The current is increased slowly over a period of ~2 hours to a maximum determined by the vapor pressure of metals. Typically, a few mTorr of metal vapor is adequate. In order to prevent the

escape of heat, a cylindrical alumina heat shield is place around the crucible. The space between the crucible and the heat shield is filled with zirconia felt. The metal vapor is then carried out of the crucible by an inert gas (usually ~5 Torr of Ar) through a stainless-steel conical chimney, which reduces the cross sectional area of the flow. The oxidant gas was admitted to the argon metal-vapor mixture through a ring located above the chimney. The molecules are formed above the exit of the chimney.

The molecules produced in the Broida oven can be detected through their chemiluminescent emission or by laser-induced fluorescence using either pulsed or continuous lasers. In this thesis, SrOD was produced in the Broida oven, and was detected by two spectroscopic techniques: laser excitation spectroscopy and optical-optical double resonance spectroscopy, which are described later in detail in this chapter.

2.2 Spectroscopic techniques

All the experiments in this thesis were carried out in emission. In the visible region, it is well-known that emission spectroscopy is more sensitive than absorption spectroscopy [6]. In absorption experiments, the noise mainly comes from the background continuum, while in emission experiments, this background continuum is absent. Although the total signal level is reduced in emission experiments, the overall signal-noise ratio is increased because the noise declines much more than the signal. In the infrared region, the advantages of emission spectroscopy are not so obvious [6]. Infrared emission spectroscopy requires that sample be at a higher or lower temperature than the spectrometer. Usually, furnaces are used to heat the sample. The blackbody radiation from hot furnaces is a background continuum, and provides noise. Fortunately, these unwanted blackbody radiation can be greatly reduced by limiting the field of view with apertures and by limiting the spectral range of detectors with band pass filters. Therefore, the advantages of emission spectroscopy persist into the infrared.

In this thesis, all the molecules except SrOD were studied by Fourier transform spectroscopy. Two laser spectroscopic techniques were used to study SrOD: laser excitation spectroscopy and optical-optical double-resonance spectroscopy.

2.2.1 Fourier transform spectroscopy

The essential component of Fourier transform spectrometers is the Michelson interferometer, first proposed by Albert Michelson in 1891 [7]. A schematic diagram of a Michelson interferometer is given in Figure 2.4. Light from an external source reaches the beamsplitter and splits into two beams. These two beams are reflected back by two mirrors and recombined at the beamsplitter. One mirror is moved to change the path difference x between the two interfering beams. At the detector, the signal as a function of the path difference x between the two beams – the interferogram – is the Fourier transform of the spectrum. The spectrum can be recovered by taking the inverse Fourier transform of the interferogram. The principles of Fourier transform spectroscopy have been described in detail in Refs. [8,9]. A brief description is given here.

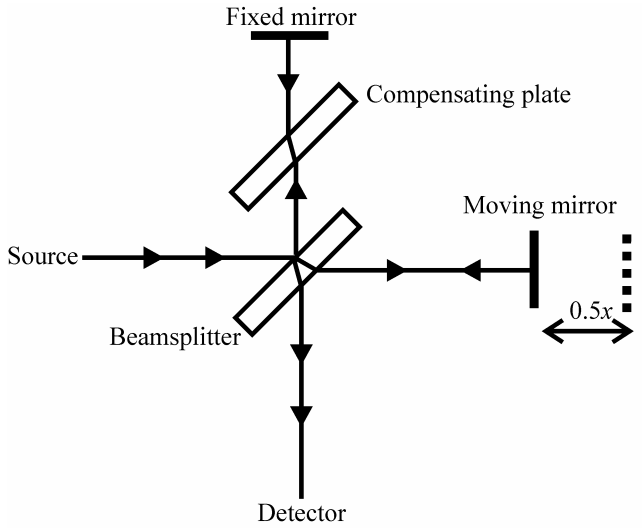

Figure 2.4 A schematic diagram of a Michelson interferometer. The compensating plate is used to match optical paths through beamsplitter material.

From the superposition of two monochromatic coherent beams of wavenumber $\tilde{\nu}$ with an optical path difference x between them, the intensity of the interferogram $I(x)$ is given by

$$I(x) = B(\tilde{\nu})[1 + \cos(2\pi\tilde{\nu}x)], \tag{2.1}$$

where $B(\tilde{\nu})$ is the spectral intensity as a function of wavenumber $\tilde{\nu}$. When the source contains more than one frequency, the intensity of interferogram is obtained by summing the contributions from all spectral elements

$$\begin{aligned} I(x) &= \int_0^{+\infty} B(\tilde{\nu})[1 + \cos(2\pi\tilde{\nu}x)]d\tilde{\nu} \\ &= \int_0^{+\infty} B(\tilde{\nu})d\tilde{\nu} + \int_0^{+\infty} B(\tilde{\nu})\cos(2\pi\tilde{\nu}x)]d\tilde{\nu} \end{aligned}. \tag{2.2}$$

The first term is a constant while the second term contains all the information on the spectrum and is defined as $I'(x)$,

$$I'(x) = \int_{-\infty}^{+\infty} B(\tilde{\nu})\cos(2\pi\tilde{\nu}x)d\tilde{\nu}, \tag{2.3}$$

where the lower limit of integration of this term can be taken as -∞ because $B(\tilde{\nu}) = 0$ for negative $\tilde{\nu}$. The spectrum can be recovered from the interferogram $I'(x)$ as

$$B(\tilde{\nu}) = \int_{-\infty}^{+\infty} I'(x)\cos(2\pi\tilde{\nu}x)dx. \tag{2.4}$$

In reality, the interferogram is recorded up to a finite optical path difference x = L, not to infinity. Therefore, the limits of Eq. (2.4) are replace by –L and +L. As a result, the spectrum has a finite

resolution $\Delta\tilde{\nu}$, which is the full width at half maximum (FWHM) of the spectral lines. Usually resolution is defined as

$$\Delta\tilde{\nu} = \frac{0.6}{L}, \tag{2.5}$$

where L is the maximum optical path difference in an experiment. Different companies have different definitions of resolution. The Bruker company defines the resolution as 0.9/L for its instruments. The maximum optical path difference of the Bruker IFS 120 HR Fourier transform spectrometer in the Bernath laboratory is about 5 meters, which gives the highest resolution of 0.002 cm^{-1}. All the experiments reported in this thesis were carried out at high temperatures or high pressures, where Doppler broadening or pressure broadening is dominant, respectively. The linewidth was on the order of 0.01 cm^{-1} to 0.05 cm^{-1}, and it was not necessary to use the maximum possible instrumental resolution.

2.2.2 Laser excitation spectroscopy

Figure 2.5 gives an experimental block diagram for laser excitation experiments in the Bernath laboratory. The output of a cw single-mode laser is split into two beams: one was directed into an iodine vapor cell for calibration, and the other beam was amplitude modulated by a mechanical chopper and then directed vertically into the Broida-type oven. As the ring dye laser is scanned, the excitation fluorescence from the excited state was collected using a photomultiplier tube (PMT) with a red pass filter through a monochromator. The monochromator is used as a band pass filter, and is not scanned during the experiments. The output current signal from the PMT was transformed into a voltage signal by connecting a resistance (1 MΩ), then amplified by a lock-in amplifier and sent to a computer. Every time the laser frequency is in resonance with a molecular transition, a fluorescence signal is obtained.

The Bernath laboratory has two types of cw single-mode lasers: dye and Ti:Sapphire lasers. The Ti:Sapphire laser covers the 10000 – 13000 cm^{-1} spectral region in which the I_2 spectra are extremely weak. The Ti:Sapphire laser is calibrated by the laser absorption spectra of hot I_2. The dye lasers cover the higher wavenumber region and are calibrated by using the laser excitation spectra of I_2 at room temperature. Figure 2.5 shows the use of a laser excitation spectrum of I_2 at room temperature as calibration. A small fraction of the laser beam is directed into an I_2 cell and the excitation spectrum of I_2 is collected by a PMT. The output current signal from the PMT is amplified by a current-to-voltage amplifier, and then sent to the computer.

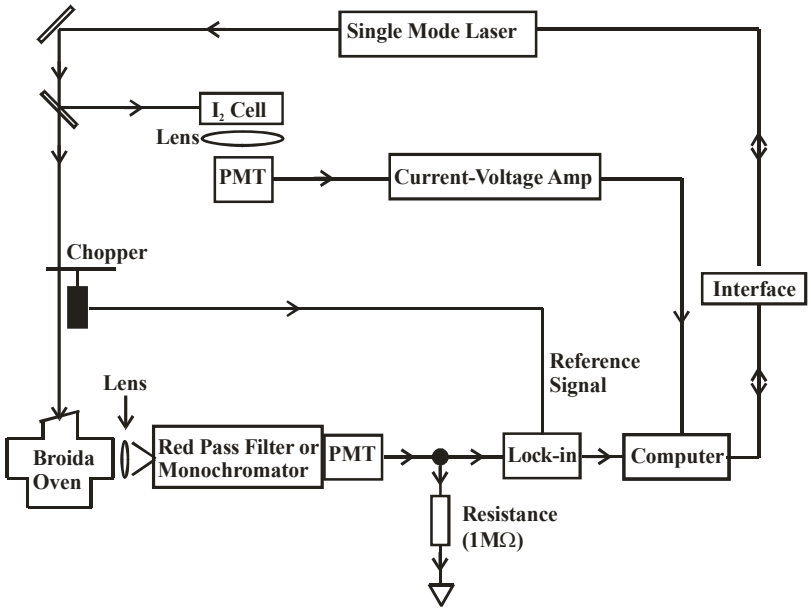

Figure 2.5 A block diagram for laser excitation experiments in the Bernath laboratory.

2.2.3 Optical-optical double-resonance spectroscopy

The laser excitation spectroscopy is an ideal technique for studying low-lying excited states of molecules. However, using one single-mode laser, this technique is unable to study higher energy electronic states. One solution for this problem is optical-optical double resonance spectroscopy, which is illustrated in Figure 2.6. First, a laser is used to pump the molecules to the *A* state. Then a second laser is used to promote the molecules from the *A* state to the *B* state. The UV fluorescence from the *B* state to the *X* ground state is collected using a blue pass filter.

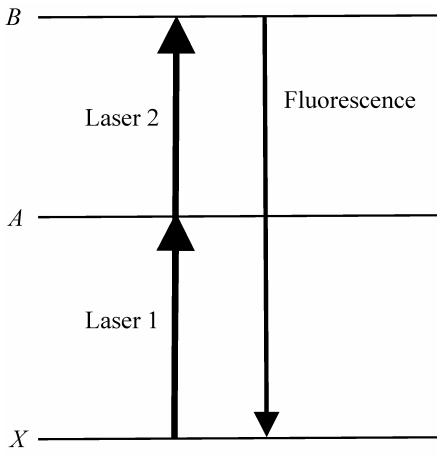

Figure 2.6 Optical-optical double-resonance spectroscopy.

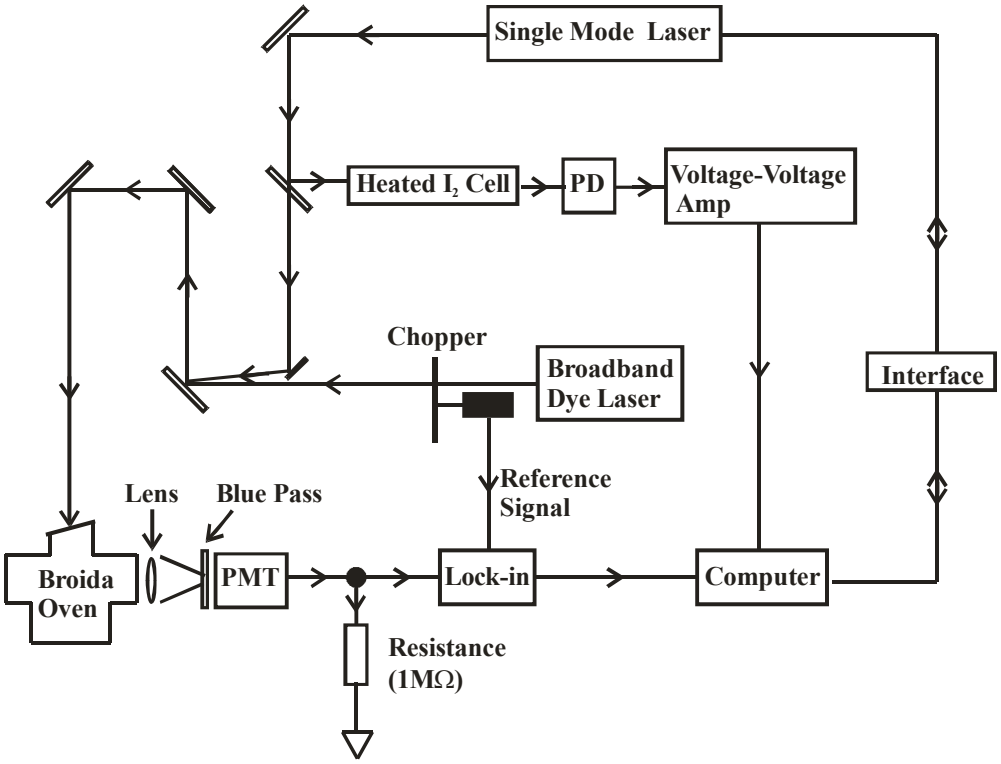

Figure 2.7 An block diagram for optical-optical double-resonance experiments in the Bernath laboratory.

Figure 2.7 shows a block diagram for optical-optical double-resonance experiments. The pump laser is a linear cavity dye laser (DCM dye) with a bandwidth of about 1 cm^{-1}. The reason for using a broadband laser is that more *J* levels in the *A* state are populated. The probe laser is a single-mode dye or Ti:sapphire ring laser. The output of the pump and probe lasers are directed collinearly and focused into the Broida oven. The signal is optimized by maximizing the overlap of the pump and probe lasers in the reaction zone. As the probe laser is scanned, the excitation fluorescence from the *B* state is collected using a PMT with a blue pass filter. The output current signal from the PMT is transformed, amplified by a lock-in amplifier and then sent to a computer. The mechanical chopper modulates the pump laser. Every time the probe single mode laser is in resonance with a molecular transition in the *B* to *A* transition, a signal is obtained.

Figure 2.7 shows the use of the laser absorption spectra of hot I_2 for calibration. A small fraction of the laser beam is directed into a heated I_2 cell, and the absorption spectrum of I_2 is collected by a photodiode detector (PD). The output voltage signal from the PD is amplified and then sent into the computer.

2.3 References

[1] O. Knacke, O. Kubaschewski and L. Hesselmann, *Thermochemical Properties of Inorganic Substances*, volume 51, Springer-Verlag Berlin, Heidelberg, 2nd edition, 1991.

[2] A. S. King, Astrophys. J. **28,** 300 (1908).

[3] J. West, R. Bradford, J.D. Eversole and C. Jones, Rev. Sci. Instr. **46,** 164 (1975).

[4] R. F. Wormsbecher, M. Trkula, R.E. Penn and D.O. Harris, J. Mol. Spectrosc. **97,** 29 (1983).

[5] J. Nakagawa, R.F. Wormsbecher and D.O. Harris, J. Mol. Spectrosc. **97,** 37 (1983).

[6] P.F. Bernath, Adv. in Photochem. **23**, 1 (1997).

[7] A. Michelson, Phil. Mag. **31,** 256 (1891).

[8] S.O. Davis, M.C. Abrams and J.W. Brault, *Fourier transform spectroscopy*, Academic Press, New York, 2001.

[9] A. Thorne, U. Litzen and S. Johansson, *Spectrophysics*, Springer-Verlag Berlin, Heidelberg, 2nd edition, 1991.

Chapter 3

Fourier transform infrared emission spectroscopy of SbH and SbD

3.1 Introduction

SbH and SbD radicals are the least studied of the Group V diatomic hydrides. The first observation of SbH and SbD was reported in 1967 by Bollmark and Lindgren [1], and Basco and Yee [2]. They independently measured the $A\ ^3\Pi_i - X\ ^3\Sigma^-$ absorption spectra at low resolution by flash photolysis of stibine (SbH_3) and deuterostibine (SbD_3), and observed several bandheads in the region 3330 – 3900 Å. Seven years later, Bollmark and Lindgren [3] made new observations of the $A\ ^3\Pi_i - X\ ^3\Sigma^-$ transition, which permitted them to perform the first detailed rotational analysis and derive molecular constants for the $A\ ^3\Pi_i$ and $X\ ^3\Sigma^-$ states of SbH and SbD. In 1981, Bollmark *et al.* [4] extended their study of the absorption spectra of SbH and SbD to the 1900 – 1580 Å region by the flash discharge technique, and some improvements of the ground state constants were obtained together with information about several new upper states. The experimental uncertainties in the line positions in all of these studies were around 0.1 cm^{-1}.

More precise molecular constants for the $X\ ^3\Sigma^-$ ground state of SbH were obtained by Stackmann *et al*. [5], who studied 11 transitions in the fundamental band and 7 transitions in the 2 – 1 hot band by the infrared laser magnetic resonance technique with experimental uncertainties of 14 MHz (0.0005 cm^{-1}). Improved spectroscopic constants for the $X\ ^3\Sigma^-$ ground state of SbD were obtained by Urban *et al*. [6] in their study of the fundamental bands and the 2 – 1 hot bands of SbH and SbD with a tunable diode laser with experimental uncertainties of 0.001 cm^{-1}. Recently, Beutel *et al*. [7] measured the 0 – 0 and 1 – 1 bands of the $a\ ^1\Delta - X\ ^3\Sigma^-$ transitions of SbH and SbD with a Fourier transform spectrometer with experimental uncertainties of 0.02 cm^{-1}. Shestakov *et al*. [8] studied the $b\ ^1\Sigma^+ - X\ ^3\Sigma^-$ transitions of SbH and SbD by pulsed laser excitation spectroscopy with experimental uncertainties of 0.05 cm^{-1}. The spectra of Shestakov *et al*. [8] allowed the large spin splitting of about 660 cm^{-1} between the $X_1\ 0^+$ and $X_2\ 1$ spin components of the $X\ ^3\Sigma^-$ state to be determined directly. More recently, Wang *et al.* [9] observed infrared spectra of several antimony hydrides, including SbH and SbD, in solid matrices. In addition, several theoretical calculations [10 – 12] were carried out for SbH and SbD.

Infrared spectroscopy of gaseous metal hydrides is a continuing project in the Bernath laboratory. Our interest in SbH was sparked by the fact that the ro-vibrational data for SbH were very sparse. The number of infrared lines for SbH was roughly six times less than that for SbD in the experiments of Urban *et al*. [6]. They did not have a suitable laser diode for SbH, and thus only reported eight assigned lines (none of which turned out to be correct) for the infrared bands of the $X_1\ 0^+$ spin component. They also reported thirteen lines from the weaker $X_2\ 1$ spin component, which turned out to be correct.

In this chapter, new observations of SbH and SbD are reported. The $X\ ^3\Sigma^-$ ground state vibration-rotation spectrum of SbH and the near infrared spectra of the $b\ ^1\Sigma^+ - X\ ^3\Sigma^-$ transitions of SbH and SbD have been measured by Fourier transform spectroscopy with experimental uncertainties of 0.001

cm^{-1} and 0.003 cm^{-1}, respectively. The present data set was combined with the available ground state data on SbD and $a\ ^1\Delta$ data for SbH and SbD from previous work, and a least-squares fit was performed for each of the four isotopologues: ^{121}SbH, ^{123}SbH, ^{121}SbD and ^{123}SbD. The results presented in this chapter have been published in Ref. [13].

3.2 Experimental details

The SbH and SbD molecules were generated with the high temperature tube furnace and an electrical discharge, as has been described in Section 2.1.1. About 10 grams of antimony metal powder was placed inside an alumina tube and was heated to 800°C to produce about 1 Torr of antimony vapor. A mixture of 2 Torr of hydrogen or deuterium and 2.5 Torr of argon was flowed through the alumina tube, and a DC discharge (333 mA and 2.8 kV) was created between the electrodes installed at the two ends of the alumina tube. The emitted infrared radiation was focused by a CaF_2 lens into the entrance aperture of a Bruker IFS 120 HR Fourier transform spectrometer.

Electronic spectra of the SbH and SbD radicals were measured at a resolution of 0.05 cm^{-1} in the 8000 – 15000 cm^{-1} region with a visible quartz beamsplitter and a silicon diode detector. The recording time was about two hours (250 scans) for SbH, and about one hour (120 scans) for SbD. The spectrometer was not evacuated, so that the ″air″ wavenumbers of the lines were first corrected to vacuum wavenumbers [14], and then calibrated with the argon atomic lines [15] that appear in the spectra. The precision of the measured wavenumbers is approximately 0.003 cm^{-1} for the lines from the 1_f component, but 0.01 cm^{-1} for the lines from the 0^+ and 1_e components, due to the overlapping of lines from ^{121}SbH and ^{123}SbH. Antimony has two isotopes ^{121}Sb and ^{123}Sb with natural abundances of 57.3% and 42.7%, respectively.

A vibration-rotation spectrum of SbH was recorded in the 1200 – 2200 cm^{-1} region at a resolution of 0.01 cm^{-1} with a KBr beamsplitter and a liquid nitrogen-cooled HgCdTe (MCT) detector. The recording time was about four hours (240 scans). This SbH spectrum was calibrated by the use of thirteen SbH lines reported by Urban *et al*. [6] with a diode laser spectrometer. The SbH vibration-rotation lines in the present work should have an absolute accuracy of about 0.001 cm^{-1}. A much weaker SbD spectrum was also measured at a resolution of 0.01 cm^{-1} in the 800 – 2500 cm^{-1} region. The recording time was about six hours (360 scans). This SbD spectrum was not used in the analysis because of the low signal-to-noise ratio (S/N ≈ 3). Instead, the extensive diode laser data from Urban *et al*. [6] for SbD were used in the analysis.

3.3 Results and discussion

An energy level diagram of the $X\ ^3\Sigma^-$ and $b\ ^1\Sigma^+$ states of SbH is illustrated by Figure 3.1. The $X\ ^3\Sigma^-$ levels are located on the bottom and the $b\ ^1\Sigma^+$ levels are located at the top. Each level is labeled by quantum numbers N, J, rotationless (e/f) parity and total (+/–) parity. The lowest electronic configuration of SbH, π^2, gives rise to three electronic states: $^3\Sigma^-$, $^1\Delta$ and $^1\Sigma$, which is similar to the case for O_2. The spin-spin constant λ of the $X\ ^3\Sigma^-$ state is 330 cm^{-1}, and the three levels of the ground state separate into a singlet labeled as $X_1\ 0^+$ and a doublet labeled as $X_2\ 1$, and the $X_2\ 1$ levels lie roughly 660 cm^{-1} (2λ) above the 0^+ levels. In the near-infrared region for the $b\ ^1\Sigma^+ – X\ ^3\Sigma^-$ transition,

the selection rule $\Delta J = \pm 1$, $e - e$ and $f - f$ or $\Delta J = 0$ and $e - f$ gives rise to five branches, ${}^{Q}P$, ${}^{S}R$, ${}^{O}P$, ${}^{Q}Q$, and ${}^{Q}R$, which are labeled by the notation ${}^{\Delta N}\Delta J$. In the infrared region for the vibration-rotation transition of the $X\,{}^3\Sigma^-$ state, the selection rule $\Delta J = \pm 1$, $e - e$ and $f - f$ gives rise to two branches (P and R) for each of the 0^+, 1_e and 1_f components. Weak Q branches are possible for the X_2 1 spin component, but were not observed in the present experiment.

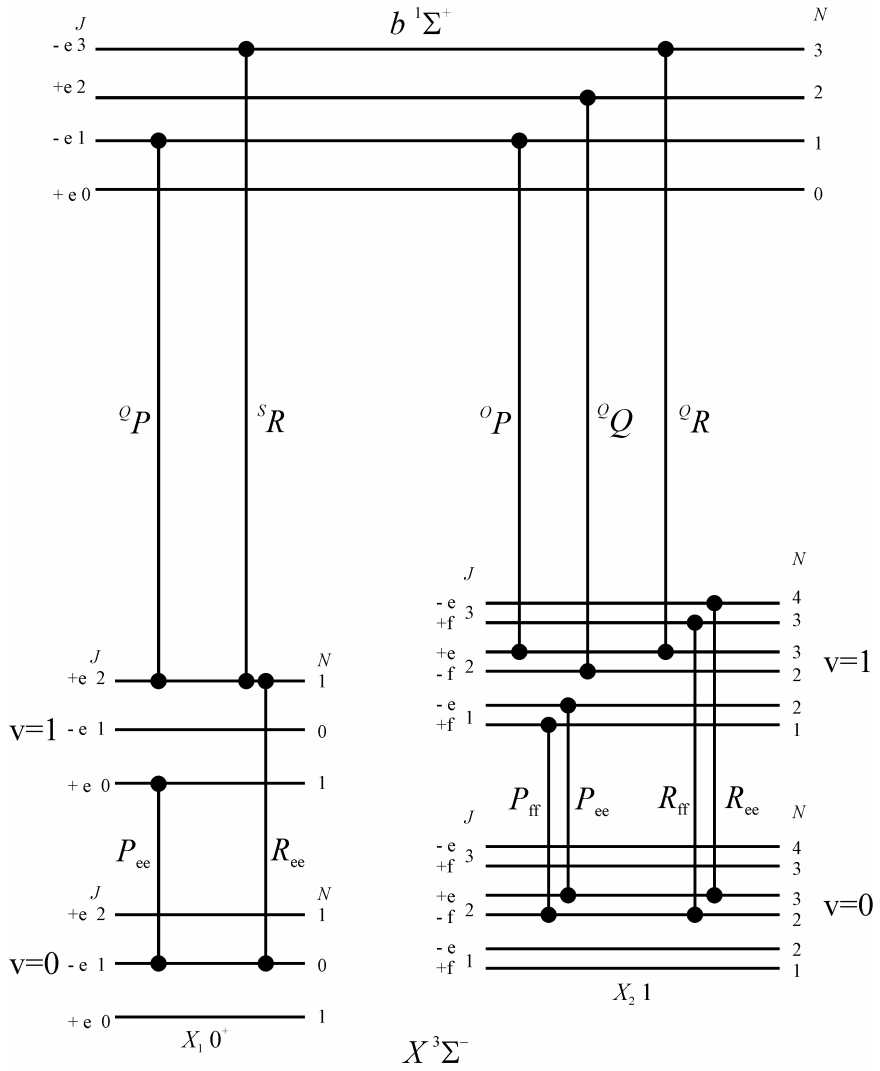

Figure 3.1 An energy level diagram of the $X\,{}^3\Sigma^-$ and $b\,{}^1\Sigma^+$ states of SbH. Each level is labeled by quantum numbers N, J, rotationless (e/f) parity, and total (+/-) parity. The five allowed branches of the $b\,{}^1\Sigma^+ - X\,{}^3\Sigma^-$ transition are labeled by the branch notation ${}^{\Delta N}\Delta J$, while the six allowed branches of the vibration-rotation transition of the $X\,{}^3\Sigma^-$ state are labeled by the branch notation $\Delta J_{P',P''}$ (P = e or f).

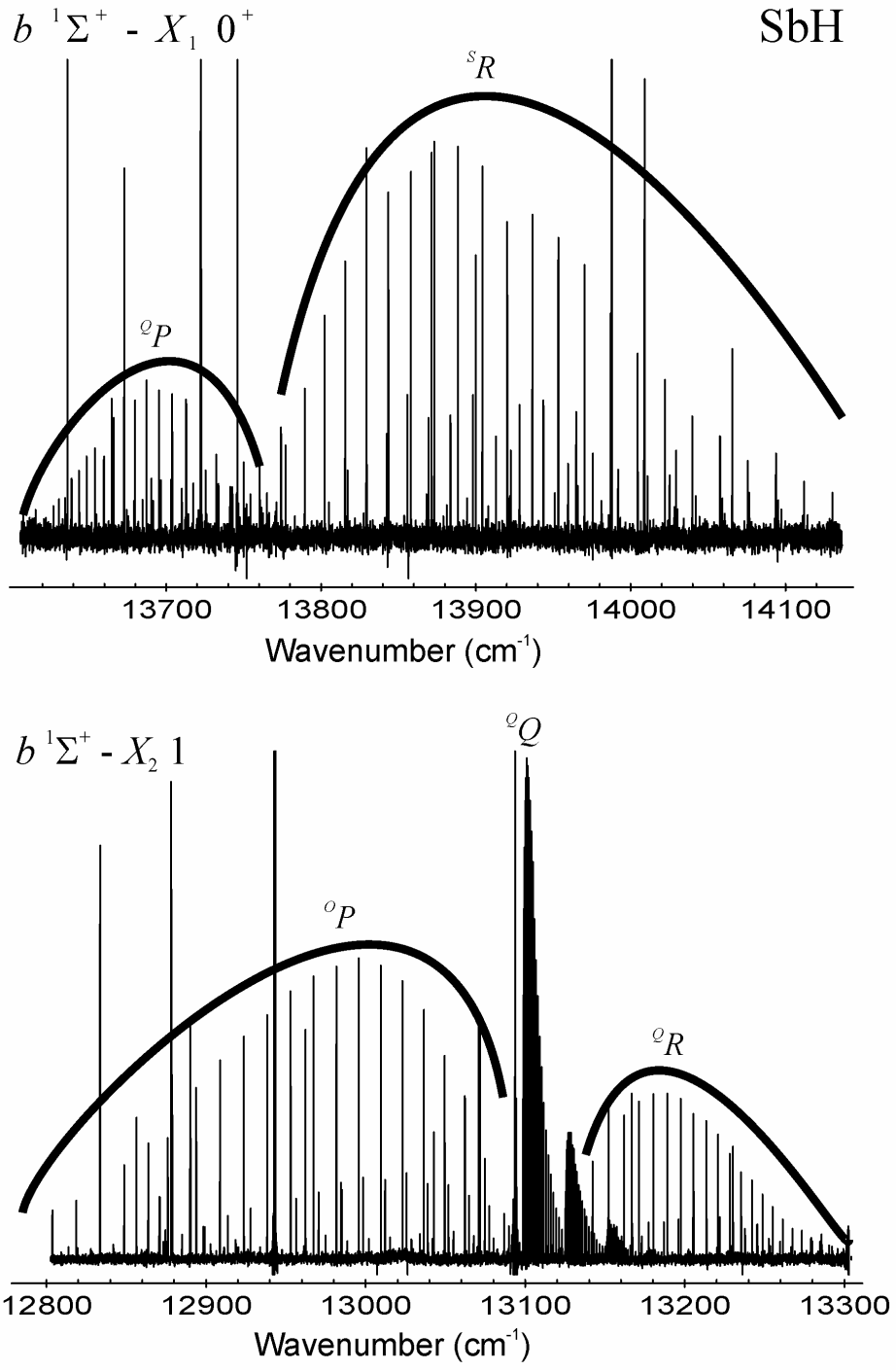

Figure 3.2 An overview spectrum of the *b* $^1\Sigma^+$ – *X* $^3\Sigma^-$ transition of SbH recorded at a resolution of 0.05 cm^{-1}. The atomic lines are from argon, and they were used to calibrate the spectrum.

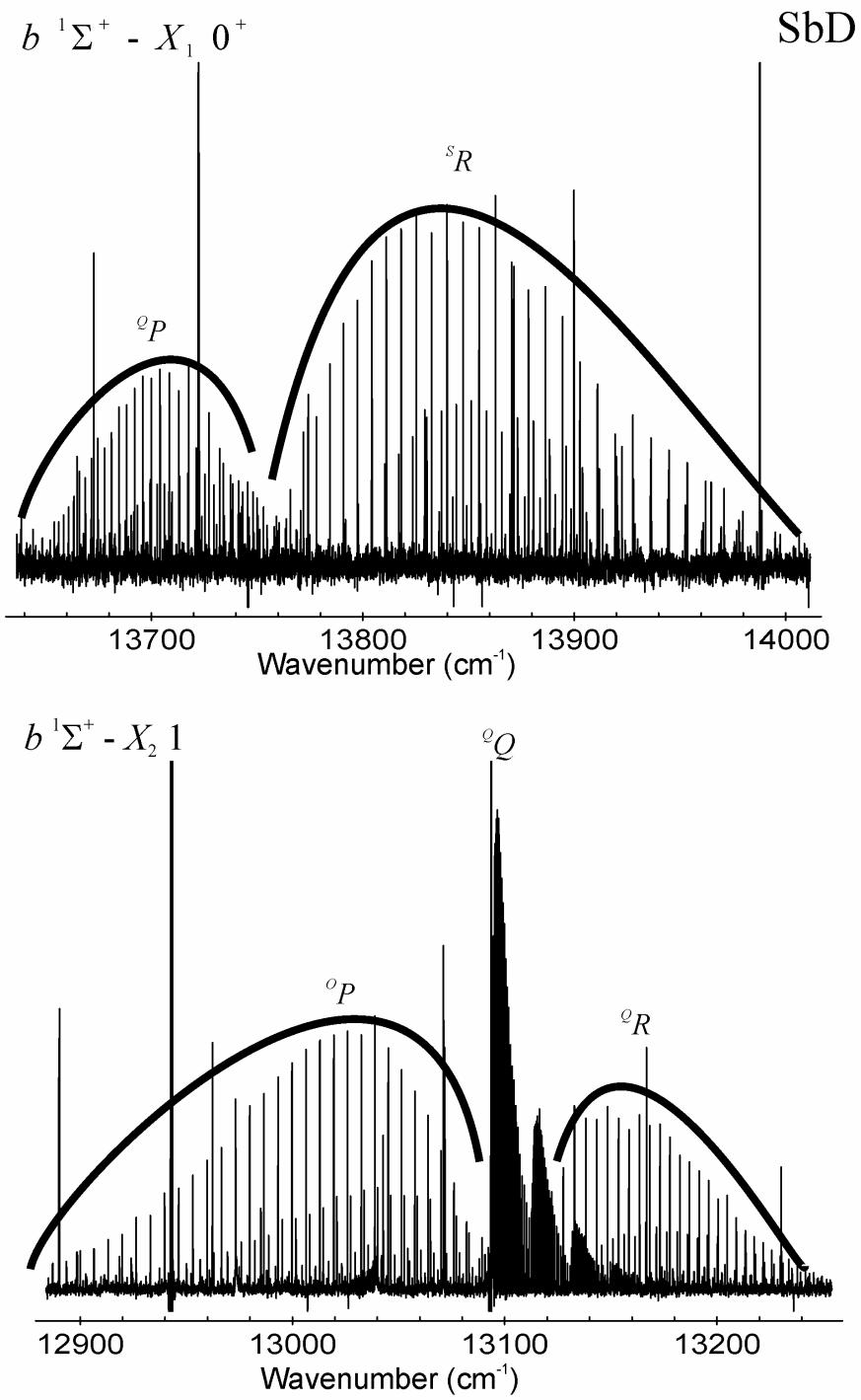

Figure 3.3 An overview spectrum of the $b\ ^1\Sigma^+ - X\ ^3\Sigma^-$ transition of SbD recorded at a resolution of 0.05 cm^{-1}. The atomic lines are from argon, and they were used to calibrate the spectrum.

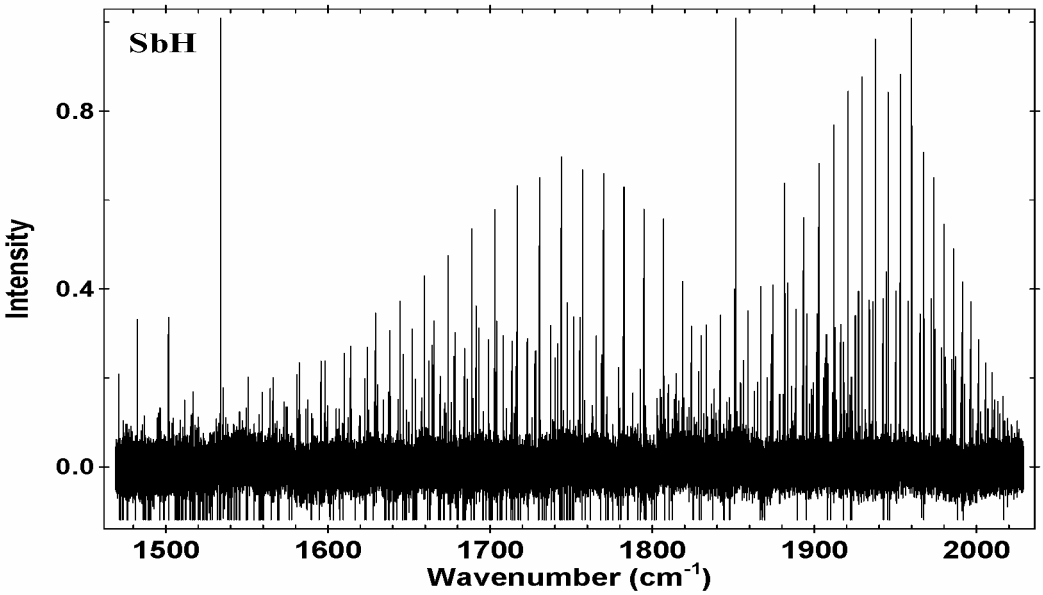

Figure 3.4 An overview of the $X\ ^3\Sigma^-$ ground state infrared spectrum of SbH recorded at a resolution of 0.01 cm^{-1}. The baseline was corrected with the Bruker OPUS software, and the absorption lines are due to atmospheric H_2O vapor.

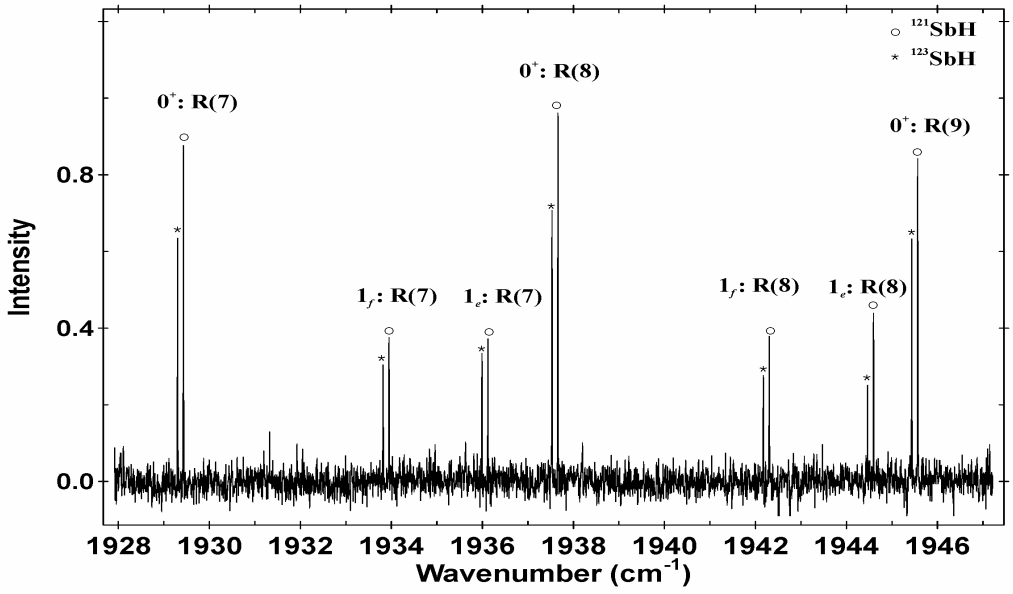

Figure 3.5 An expanded view of the *R* branch of the 1 – 0 band of the $X\ ^3\Sigma^-$ state of SbH near 1930 cm^{-1}. The lines are doubled due to the ^{121}Sb and ^{123}Sb isotopes. The doublets of the 1_e and 1_f components have about 50% of the intensity of the 0^+ component.

In the near infrared spectra of both SbH and SbD, all five branches, ${}^{S}R$, ${}^{Q}P$, ${}^{Q}Q$, ${}^{Q}R$ and ${}^{O}P$, were observed for the 0 – 0, 1 – 1 and 2 – 2 bands of the $b\ {}^1\Sigma^+ - X\ {}^3\Sigma^-$ transition. The 3 – 3 band of SbD was also observed. Figures 3.2 and 3.3 show the spectra of the $b\ {}^1\Sigma^+ - X\ {}^3\Sigma^-$ transitions of SbH and SbD. The line positions agree well with those reported by Shestakov *et al*. [8], within their error limits.

In the infrared region (Figure 3.4), the fundamental band and the 2 – 1 hot band for the 0^+, 1_e and 1_f spin components and the 3 – 2 hot band of the 0^+ component for both ^{121}SbH and ^{123}SbH were observed. The line positions for the 0^+ component differ substantially from those reported by Urban *et al.* [6], with the largest difference being 1.9 cm^{-1}. However, the line positions for the 1_e and 1_f components agree very well with their data. The fundamental band of SbD was also observed, but with a relatively low signal-to-noise ratio. In this case, the line positions for all three components agreed very well with those reported by Urban *et al.* [6]. Therefore, the line positions of the 1_e and 1_f components of SbH of Urban *et al*. [6] are reliable, thus were used for the absolute wavenumber calibration of the infrared SbH spectrum obtained in the present work.

Antimony has two isotopes ^{121}Sb and ^{123}Sb with natural abundances of 57.3% and 42.7%, respectively, so the infrared lines appear as doublets with a relative intensity of 4:3. Because the 1_e and 1_f components lie 660 cm^{-1} higher than the 0^+ component, the transitions of the 1_e and 1_f components have about 50% of the intensity of the 0^+ component (Figure 3.5). Since only the $\Delta v = 0$ sequence of the $b\ {}^1\Sigma^+ - X\ {}^3\Sigma^-$ system of SbH and SbD was observed, the isotopic splitting due to the antimony atom was only observed at high J values ($J > 25$) for the $b\ {}^1\Sigma^+ - X\ {}^3\Sigma^-$ transition.

A least-squares fit was performed for each of the four isotopologues: ^{121}SbH, ^{123}SbH, ^{121}SbD and ^{123}SbD. The data sets included the $X\ {}^3\Sigma^-$ ground state infrared data (the present FTS lines and the diode laser lines of Ref. [6]), the $b\ {}^1\Sigma^+ - X\ {}^3\Sigma^-$ transition observed in the present experiment, and the $a\ {}^1\Delta - X\ {}^3\Sigma^-$ lines reported by Beutel *et al.* [7]. In these fits, the data for the $b\ {}^1\Sigma^+ - X\ {}^3\Sigma^-$ and $a\ {}^1\Delta - X\ {}^3\Sigma^-$ transitions were almost identical for the ^{121}SbH/^{123}SbH and ^{121}SbD/^{123}SbD pairs, except for a few high J lines with resolved Sb isotopic splitting. Because there are no infrared bands to connect with the 3-3 band of the $b\ {}^1\Sigma^+ - X\ {}^3\Sigma^-$ transition of SbD, this band was fitted separately.

The energy levels of both the $b\ {}^1\Sigma^+$ and $a\ {}^1\Delta$ states were represented by the standard formula [16]:

$$F(J) = T_v + B_v J(J+1) - D_v[J(J+1)]^2 + H_v[J(J+1)]^3. \quad (3.1)$$

The energy levels of the $X\ {}^3\Sigma^-$ ground state were calculated by use of the usual Hamiltonian matrix with matrix elements derived with Hund's case (a) basis functions [17]. These matrix elements are listed for convenience in Table 3.1 in the form of multiplicative factors. The spectroscopic constants obtained for the $X\ {}^3\Sigma^-$, $b\ {}^1\Sigma^+$ and $a\ {}^1\Delta$ states for SbH are given in Table 3.2, and the corresponding constants for SbD are in Table 3.3. Since only transitions of the 0^+ component of the 3 – 2 band were observed for ^{121}SbH and ^{123}SbH, the spin-spin constant, λ_3, and the spin-rotation constant, γ_3, of the $X\ {}^3\Sigma^-$ state could not be determined and were fixed to estimated values determined by extrapolation in the fits of these two isotopologues. The spectroscopic constants for the 3 – 3 band of SbD are given separately in Table 3.4. An estimated value was also used for the spin-rotation constant, γ_3, in the separate fit of the 3 – 3 band of the $b\ {}^1\Sigma^+ - X\ {}^3\Sigma^-$ transition of SbD. The output files of the fits (including complete lists of all data) have been published in the supplementary tables of Ref. [13].

In the initial stages of the fits, the same data for the $b\ ^1\Sigma^+ - X\ ^3\Sigma^-$ transition was used for the ^{121}SbH/^{123}SbH and ^{121}SbD/^{123}SbD pairs. A systematic trend in the observed minus calculated line positions was found for nearly all of the bands of the $b\ ^1\Sigma^+ - X\ ^3\Sigma^-$ transition. The residuals were positive in the *P* branches and negative in the *R* branches of ^{121}SbH and ^{121}SbD. For ^{123}SbH and ^{123}SbD, the signs of the residuals changed: they were negative in the *P* branches and positive in the *R* branches. The residuals also increased with increasing *J* values. It was found that the unresolved lines of the two antimony isotopes cause these systematic trends. After the resolved high-*J* lines were added, the trend in the residuals of these few lines disappeared, while the systematic trend remained for the unresolved low *J* lines. Ultimately, some of these low *J* lines were simply deweighted in the final fits.

Table 3.1 Coefficients and multiplicative factors of the matrix elements of $^3\Sigma^-$ states.

Constants	(H_{11}^e)[a]	(H_{12}^e)[a]	(H_{22}^e)[a]	(H_{11}^f)[b]
G_v	1	0	1	1
B_v	$(2 + x)$[c]	$-2x^{1/2}$	x	x
D_v	$-(4 + 8x + x^2)$	$2\ x^{1/2}\ (2 + 2x)$	$-(4x + x^2)$	$-\ x^2$
H_v	$(8 + 28x + 18x^2 + x^3)$	$-2\ x^{1/2}\ (4 + 10x + 3x^2)$	$(8x + 12x^2 + x^3)$	x^3
γ_v	-2	$x^{1/2}$	-1	-1
γ_{Dv}	$-2(2 + 2x)$	$x^{1/2}\ (4 + x)$	-3x	-x
γ_{Hv}	$-2(4 + 10x + 3x^2)$	$x^{1/2}\ (8 + 12x + x^2)$	$-(8x + 5x^2)$	$-x^2$
λ_v	-4/3	0	2/3	2/3
λ_{Dv}	$-(4/3)(2 + x)$	$(2/3)\ x^{1/2}$	(2/3)x	(2/3)x

[a] Matrix elements for the 2×2 matrix with matrix elements H_{11}^e, H_{22}^e, $H_{12}^e = H_{21}^e$ for the *e* parity levels 0^+ and 1_e components, and the 1×1 matrix elements H_{11}^f for the *f* parity levels 1_f.

[b] Matrix element for the 1_f component.

[c] $x = J(J+1)$.

Table 3.2 Spectroscopic constants (in cm^{-1}) for the $X\,^3\Sigma^-$, $a\,^1\Delta$ and $b\,^1\Sigma^+$ states of ^{121}SbH and ^{123}SbH (all uncertainties are 1σ).[a]

		v = 0		v = 1		v = 2		v = 3	
State	Constants	^{121}SbH	^{123}SbH	^{121}SbH	^{123}SbH	^{121}SbH	^{123}SbH	^{121}SbH	^{123}SbH
$X\,^3\Sigma^-$	T_v	0	0	1854.17310(18)	1854.05355(22)	3640.07809(32)	3639.84809(40)	5357.20432(88)	5356.87143(99)
	B_v	5.6830941(74)	5.6823780(91)	5.5257362(67)	5.5250442(86)	5.3676276(76)	5.366966(12)	5.2060522(99)	5.205426(12)
	$10^4\,D_v$	2.06289(31)	2.06362(36)	2.05652(27)	2.05695(35)	2.05484(30)	2.05546(65)	2.01139(29)	2.01249(34)
	$10^9\,H_v$	3.052(39)	3.217(43)	2.937(31)	3.057 (41)	2.736(36)	2.92(12)	…	…
	γ_v	-0.23922(15)	-0.23994(18)	-0.19332(15)	-0.19402(18)	-0.14481(18)	-0.14535(21)	-0.09368[b]	-0.09386[b]
	$10^5\,\gamma_{Dv}$	7.037(28)	7.152(32)	8.147(27)	8.259(30)	9.441(43)	9.555(46)	…	…
	λ_v	333.33269(48)	333.33439(54)	334.27953(47)	334.28153(53)	335.00807(49)	335.01012(55)	335.51822[b]	335.52028[b]
	$10^3\,\lambda_{Dv}$	1.9492(24)	1.9567(29)	1.7868(24)	1.7927(29)	1.5112(26)	1.5201(31)		
$a\,^1\Delta$	T_v	6380.7823(26)	6380.7819(30)	8256.9333(98)	8256.809(11)				
	B_v	5.706694(69)	5.706032(76)	5.55268(51)	5.55259(61)				
	$10^4\,D_v$	2.0388(37)	2.0387(39)	2.021(57)	2.075(72)				
$b\,^1\Sigma^+$	T_v	13321.15387(78)	13321.15427(91)	15202.3132(10)	15202.1937(12)	17014.4636(16)	17014.2371(21)		
	B_v	5.717920(11)	5.717218(13)	5.561834(16)	5.561165(19)	5.404247(39)	5.403503(44)		
	$10^4\,D_v$	2.04249(36)	2.043336(42)	2.03773(61)	2.03855(73)	2.0489(23)	2.0438(24)		
	$10^9\,H_v$	3.019(41)	3.191(45)	2.697(62)	2.834(75)	3.42(39)	2.63(38)		

[a] Fitted to the $X\,^3\Sigma^-$ ground state infrared data (our FTS lines and the diode laser lines [6]), the $b\,^1\Sigma^+ - X\,^3\Sigma^-$ lines observed in our experiment, and the $a\,^1\Delta - X\,^3\Sigma^-$ lines reported by Beutel *et al.*[7].

[b] Fixed values determined by extrapolation of the corresponding constants for v = 0 – 2 .

Table 3.3 Spectroscopic constants (in cm^{-1}) for the $X\,^3\Sigma^-$, $a\,^1\Delta$ and $b\,^1\Sigma^+$ states of ^{121}SbD and ^{123}SbD (all uncertainties are 1σ).[a]

		v = 0		v = 1		v = 2	
State	Constants	^{121}SbD	^{123}SbD	^{121}SbD	^{123}SbD	^{121}SbD	^{123}SbD
$X\,^3\Sigma^-$	T_v	0	0	1331.25546(21)	1331.08415(20)	2628.1647(22)	2627.8277(23)
	B_v	2.879930(10)	2.8792906(81)	2.8235738(94)	2.8229452(76)	2.767072(15)	2.766440(16)
	$10^4\,D_v$	0.52488(21)	0.52673(17)	0.52362(19)	0.52525(16)	0.52305(24)	0.52362(24)
	$10^9\,H_v$	0.307(13)	0.454(10)	0.308(11)	0.4372(86)	0.348(12)	0.4316(90)
	γ_v	-0.11328(23)	-0.11377(26)	-0.08506(22)	-0.08504(25)	-0.05401(65)	-0.05466(73)
	$10^5\,\gamma_{Dv}$	1.769(25)	1.892(24)	2.384(23)	2.435(23)	3.111(85)	2.772(97)
	λ_v	333.02596(57)	333.02534(59)	333.73637(56)	333.73606(58)	334.35316(99)	334.3533(11)
	$10^3\,\lambda_{Dv}$	0.9819(15)	0.9802(17)	0.9328(15)	0.9315(16)	0.8570(40)	0.8435(56)
$a\,^1\Delta$	T_v	6389.1503(25)	6389.1476(27)	7735.3033(54)	7735.1280(51)		
	B_v	2.891087(33)	2.890490(33)	2.836074(75)	2.835590(72)		
	$10^4\,D_v$	0.51584(80)	0.51793(79)	0.5185(20)	0.5237(20)		
$b\,^1\Sigma^+$	T_v	13316.09396(87)	13316.09281(90)	14666.56238(82)	14666.39038(88)	15982.4632(23)	15982.1259(25)
	B_v	2.897829(11)	2.897195(10)	2.842011(11)	2.8413851(95)	2.785864(19)	2.785247(20)
	$10^4\,D_v$	0.51967(22)	0.52163(20)	0.51897(20)	0.52066(18)	0.51893(44)	0.52017(49)
	$10^9\,H_v$	0.298(14)	0.450(11)	0.305(12)	0.4369(94)	0.309(32)	0.449(34)

[a] Fitted to the $X\,^3\Sigma^-$ state infrared data reported by Urban *et al.* [6], the $b\,^1\Sigma^+ - X\,^3\Sigma^-$ transition observed in our experiment, and the $a\,^1\Delta - X\,^3\Sigma^-$ transition reported by Beutel *et al.* [7].

Table 3.4 Spectroscopic constants (in cm^{-1}) for the $X\,^3\Sigma^-$ and $b\,^1\Sigma^+$ states of SbD (v = 3) from the separate fit of the 3 – 3 band (all uncertainties are 1σ).

State	Constants	Value
$X\,^3\Sigma^-$	B_3	2.71047(16)
	$10^4\,D_3$	0.5566(30)
	γ_3	-0.02001[a]
	λ_3	334.8411(26)
	$10^3\,\lambda_{D3}$	0.857(15)
$b\,^1\Sigma^+$	T_{3-3}	13372.8154(30)[b]
	B_3	2.72941(15)
	$10^4\,D_3$	0.5535(29)

[a]Fixed value determined by extrapolation of γ_v from v = 0 – 2.

[b]Band origin of the 3 – 3 band of the $b\,^1\Sigma^+ – X\,^3\Sigma^-$ transition of SbD.

Table 3.5 shows a comparison of the spectroscopic constants obtained in the present work with the recent literature values. The new constants have a higher precision and are more extensive than those from the previous work. They agree reasonably well with the constants of Fink and co-workers [7, 8], but less well with those of Urban *et al*. [6]. In fact, it is a surprise that the constants of SbH reported by Urban *et al*. [6] are even in modest agreement with others, because their line positions for the 0^+ component differ substantially from the present measurements.

3.4 Conclusions

The $X\,^3\Sigma^-$ ground state vibration-rotation spectrum of SbH and the near infrared spectra of the $b\,^1\Sigma^+ – X\,^3\Sigma^-$ transitions of SbH and SbD have been measured at high resolution by Fourier transform spectroscopy. In the infrared region, the 1 – 0 and 2 – 1 bands of the three components (0^+, 1_e and 1_f) as well as the 0^+ component of the 3 – 2 band were observed for ^{121}SbH and ^{123}SbH. In the near infrared region, the 0 – 0, 1 – 1 and 2 – 2 bands of the $b\,^1\Sigma^+ – X\,^3\Sigma^-$ system of both SbH and SbD, as well as the 3 – 3 band of SbD, were observed. The present data set was combined with the available ground-state data on SbD and $a\,^1\Delta$ data for SbH and SbD from previous work, and a least-squares fit was performed for each of the four isotopologues: ^{121}SbH, ^{123}SbH, ^{121}SbD and ^{123}SbD. The present work has resulted in a substantial improvement in the spectroscopic constants of SbD, and particularly for SbH. The new constants are both more extensive and more precise than those reported previously.

Table 3.5 A comparison of spectroscopic constants (in cm^{-1}) for the $X\ ^3\Sigma^-$, $a\ ^1\Delta$ and $b\ ^1\Sigma^+$ states of SbH and SbD (v = 0).

		^{121}SbH				^{121}SbD			
State	Constants	Present work	Shestakov *et al.*[a]	Urban *et al.*[b]	Beutel *et al.*[c]	Present work	Shestakov *et al.*[a]	Urban *et al.*[b]	Beutel *et al.*[c]
$X^3\Sigma^-$	B_0	5.6830941(74)	5.6825(3)	5.684417(85)		2.879930(10)	2.8798(1)	2.880600(19)	
	$10^4\ D_0$	2.06289(31)	2.05(1)	2.1095(99)		0.52488(21)	0.528(7)	0.52574(31)	
	$10^9\ H_0$	3.052(39)	…	2.921		0.307(13)	…	0.375(24)	
	γ_0	-0.23922(15)	-0.238(6)	-0.2319(17)		-0.11328(23)	-0.117(3)	-0.11086(14)	
	$10^5\ \gamma_{D0}$	7.037(28)	6(3)	8.5(15)		1.769(25)	3.1(9)	1.53(19)	
	λ_0	333.33269(48)	333.373(4)	333.29758(53)		333.02596(57)	333.084(7)	333.36984(20)	
	$10^3\ \lambda_{D0}$	1.9492(24)	2(1)	1.044(47)		0.9819(15)	0.94(4)	1.007(18)	
$a\ ^1\Delta$	T_0	6380.7823(26)			[6175.349(2)][d]	6389.1503(25)			[6175.6705(5)][d]
	B_0	5.706694(69)			5.70465(8)	2.891087(33)			2.89033(3)
	$10^4\ D_0$	2.0388(37)			2.041(4)	0.51584(80)			0.5163(6)
$b\ ^1\Sigma^+$	T_0	13321.15387(78)	[13098.623(4)][e]			13316.09396(87)	[13093.844(6)][e]		
	B_0	5.717920(11)	5.7175(3)			2.897829(11)	2.8976(2)		
	$10^4\ D_0$	2.04249(36)	2.04(1)			0.51967(22)	0.519(6)		
	$10^9\ H_0$	3.019(41)	…			0.298(14)	…		

[a] Constants derived from unresolved lines of ^{121}SbH and ^{123}SbH from Ref. [8].
[b] Constants calculated from the equilibrium constants for ^{121}SbH from Ref. [6].
[c] Constants derived from unresolved lines of ^{121}SbH and ^{123}SbH from Ref. [7].
[d] Band origins of the 0 – 0 band of the $b\ ^1\Sigma^+ - X_2\ 1$ transition from Ref. [7], which can not be directly compared with our constants.
[e] Band origins of the 0 – 0 band from Ref. [8] , which can not be directly compared with our constants.

3.5 References

[1] P. Bollmark and B. Lindgren, Chem. Phys. Lett. **1**, 480 (1967).

[2] N. Basco and K.K. Yee, Spectrosc. Lett. **1**, 13 (1968).

[3] P. Bollmark and B. Lindgren, Phys. Scripta. **10**, 325 (1974).

[4] P. Bollmark, B. Lindgren and U. Sassenberg, Phys. Scripta. **24**, 542 (1981).

[5] V. Stackmann, K. Lipus, and W. Urban, Mol. Phys. **80**, 635 (1993).

[6] R.-D. Urban, K. Essig, and H. Jones, J. Chem. Phys. **99**, 1591 (1993).

[7] M. Beutel, K.D. Setzer, O. Shestakov, and E.H. Fink, J. Mol. Spectrosc. **179**, 79 (1996).

[8] O. Shestakov, R. Gielen, A.M. Pravilov, K.D. Setzer and E.H. Fink, J. Mol. Spectrosc. **191,** 199 (1998).

[9] X. Wang, P.F. Souter and L. Andrews, J. Phys. Chem. A **107**, 4244 (2003).

[10] K. Balasubramanian, N. Tanpipat and J.E. Bloor, J. Mol. Spectrosc. **124,** 458 (1987).

[11] A.B. Alekseyev, H.-P. Liebermann, R.M. Lingott, O. Bludsky and R.J. Buenker, J. Chem. Phys. **108**, 7695 (1998).

[12] S. Hirata, T. Yanai, W.A. de Jong, T. Nakajima and K. Hirao, J. Chem. Phys. **120**, 3297 (2004).

[13] S. Yu, D. Fu, A. Shayesteh, I.E. Gordon, D.R.T. Appadoo and P.F. Bernath, J. Mol. Spectrosc. **229**, 257 (2005).

[14] B. Edlen, Metrologia, **2**, 71 (1966).

[15] W. Whaling, W.H.C. Anderson, M.T. Carle, J.W. Brault and H.A. Zarem, J. Res. Natl. Inst. Stand. Technol. **107**, 149 (2002).

[16] G. Herzberg, *Molecular Spectra and Molecular Structure, Volume 1, Spectra of Diatomic Molecules*, Van Nostrand, Princeton, NJ, 1950.

[17] C.R. Brazier, R.S. Ram and P.F. Bernath, J. Mol. Spectrosc. **120**, 381 (1986).

Chapter 4

Fourier transform infrared emission spectroscopy of TeH and TeD

4.1 Introduction

The TeH molecule has not been studied as much as the earlier group VI hydrides, OH, SH and SeH. The TeH radical was first observed in 1964 by Radford using electron paramagnetic resonance techniques; the molecular *g*-factor, Λ-type doubling and hyperfine structure of the $X\ ^2\Pi$ state were determined, and the rotational constants were estimated from second-order shifts of the lines [1]. Eight years later, Donovan *et al*. [2] studied the UV absorption spectra of TeH and observed thirteen bands associated with transitions from the $X\ ^2\Pi$ state to several Rydberg states. From the Rydberg series, they derived an ionization potential of 9.1 eV. Donovan *et al*. [2] did not carry out a rotational analysis, and they could not assign all the observed bands. Little *et al.* [3] studied the spin-orbit relaxation of the $X\ ^2\Pi_{1/2}$ state of TeH by the flash photolysis of H_2Te, and the production of TeH ($X\ ^2\Pi_{1/2}$) in the primary photochemical step was discussed. Balkis *et al.* [4] estimated the bond-dissociation energy of TeH as 1.9 eV by the appearance potentials for electron impact ionization of H_2Te. More recently, Gal *et al*. [5] obtained a value of 2.65 eV for the dissociation energy of TeH from the gas-phase acidity of H_2Te and a thermochemical cycle. Friedhoff *et al.* [6] studied the photodetachment spectrum of TeH^- and determined the electron affinity of TeH as 2.102 eV for the $X\ ^2\Pi_{3/2}$ spin component. Recently, Fink *et al*. [7] recorded the near infrared emission spectra of the $X\ ^2\Pi_{1/2} - X\ ^2\Pi_{3/2}$ transition for TeH and TeD with a Fourier transform spectrometer with experimental uncertainties of 0.001 cm^{-1}. Towle *et al.* [8] and Gillett *et al.* [9] studied the infrared spectra of the $X\ ^2\Pi_{3/2}$ spin component for TeH and TeD by CO laser magnetic resonance with experimental uncertainties of 0.01 cm^{-1}. Theoretical investigations of TeH have been carried by Balasubramanian *et al*. [10-11], Pisani *et al*. [12] and Setzer *et al*. [13].

The previous data for the ground $X\ ^2\Pi$ state of TeH are relatively sparse. Fink *et al*. measured primarily the 0 – 0 bands of the $X\ ^2\Pi_{1/2} - X\ ^2\Pi_{3/2}$ transition near 4000 cm^{-1} for TeH and TeD. In addition, a few lines were measured for the 1 – 1 band of the $X\ ^2\Pi_{1/2} - X\ ^2\Pi_{3/2}$ transition of TeH and the 2 – 0 vibrational overtone band of the $X\ ^2\Pi_{3/2}$ spin component of TeH. The laser magnetic resonance data of Gillett *et al*. are only for $X\ ^2\Pi_{3/2}$, because the $X\ ^2\Pi_{1/2}$ spin component does not tune sufficiently with magnetic field to obtain spectra. They saw five low *J* transitions for TeH and eleven transitions for TeD covering the 1 – 0, 2 – 1 and 3 – 2 bands.

In this chapter, extensive observations and analysis of the $\Delta v = 1$ infrared vibration-rotation bands of the $X\ ^2\Pi_{3/2}$ spin component and the $\Delta v = 0$ sequence bands of the $X\ ^2\Pi_{1/2} - X\ ^2\Pi_{3/2}$ transition for both TeH and TeD are reported. An interesting perturbation with $\Delta v = 2$ was found between the $X\ ^2\Pi_{1/2}$ and $X\ ^2\Pi_{3/2}$ spin components of TeH. Two kinds of fits were carried out for each of the ten observed isotopologues: ^{130}TeD, ^{128}TeD, ^{126}TeD, ^{130}TeH, ^{128}TeH, ^{126}TeH, ^{125}TeH, ^{124}TeH, ^{123}TeH and ^{122}TeH. Lines of each of the isotopologues of TeD were fitted first as Hund's case (a) states, and then as Hund's case (c) states. Lines of each of the isotopologues of TeH were fitted first as Hund's case (a) states with a modified Hund's case (a) matrix to account for the perturbation, and then as Hund's

case (c) states with the perturbed lines deweighted. The results presented in this chapter have been published in Ref. [14].

4.2 Experimental details

The TeH and TeD molecules were generated with a high temperature tube furnace with an electrical discharge, as has been described in Section 2.1.1. About 10 grams of tellurium metal powder was placed inside an alumina tube and was heated to 500°C to produce about 1 Torr of tellurium vapor. A mixture of 1.5 Torr of hydrogen or deuterium and 2 Torr of argon was flowed through the alumina tube, and a DC discharge (300 mA and 3 kV) was created between the electrodes installed at the two ends of the alumina tube. The emitted infrared radiation was focused by a CaF_2 lens into the entrance aperture of a Bruker IFS 120 HR Fourier transform spectrometer.

A spectrum of TeH was measured at a resolution of 0.01 cm^{-1} in the 1800 – 4000 cm^{-1} region with a KBr beamsplitter and a liquid nitrogen-cooled InSb detector. With the same beamsplitter and detector, a spectrum of TeD was measured at a resolution of 0.02 cm^{-1} in the 1800 – 7000 cm^{-1} region. The recording time was about two hours (120 scans) for TeH, and about one hour (100 scans) for TeD. Because the vibration-rotation bands of TeD fall outside the InSb region, about 400 scans were recorded at a resolution of 0.02 cm^{-1} in the 1200 – 3000 cm^{-1} region with a KBr beamsplitter and a liquid nitrogen-cooled HgCdTe (MCT) detector. The recording time was about four hours.

In the process of optimizing the experimental conditions, a high resolution spectrum in the 1800 – 7000 cm^{-1} region was obtained, which contains strong $H^{35}Cl$ and $H^{37}Cl$ lines from the 1 – 0 and 2 – 1 vibration-rotation bands. HCl lines from Ref. [15] were used to calibrate the very strong atomic lines in this spectrum. These strong atomic lines are present in all the TeH and TeD spectra, and thus were used to calibrate the TeH and TeD spectra to the same wavenumber scale. The lines should have an absolute accuracy of about 0.001 cm^{-1} for the vibration-rotation bands and about 0.005 cm^{-1} for the $X\,^2\Pi_{1/2} - X\,^2\Pi_{3/2}$ transition.

4.3 Results and discussion

A $^2\Pi$ state has $^2\Pi_{3/2}$ and $^2\Pi_{1/2}$ ($\Lambda = 1$, $\Sigma = \pm 1/2$) spin components. The spin-orbit constant A of the $X\,^2\Pi$ state is around -3800 cm^{-1} [7], so the $^2\Pi_{1/2}$ component lies 3800 cm^{-1} higher than the $^2\Pi_{3/2}$ component. A Hund's case (a) limit $X\,^2\Pi_{1/2} - X\,^2\Pi_{3/2}$ electronic transition is strictly forbidden. The observation of the $X\,^2\Pi_{1/2} - X\,^2\Pi_{3/2}$ electronic transition in TeH probably indicates a partial tendency towards Hund's case (c) in the $X\,^2\Pi$ state. An energy level diagram of the $X\,^2\Pi$ state of TeH is shown in Figure 4.1. Each level is labeled by quantum number J, rotationless (e/f) parity and total (+/–) parity. Each rotational level is split into a doublet due to Λ-doubling. In the near-infrared region for the $X\,^2\Pi_{1/2} - X\,^2\Pi_{3/2}$ transition, the selection rule $\Delta J = \pm 1$, $e - e$ and $f - f$ or $\Delta J = 0$ and $e - f$ gives rise to six branches, P_{ee}, P_{ff}, Q_{ef}, Q_{fe}, R_{ee}, and R_{ff} (doubled P, Q and R branches). In the infrared region for the vibration-rotation transition of the $X\,^2\Pi_{3/2}$ component, the selection rule $\Delta J = \pm 1$, $e - e$ and $f - f$ gives rise to four strong branches, P_{ee}, P_{ff}, R_{ee} and R_{ff}, and $\Delta J = 0$ and $e - f$ gives rises to two weak branches, Q_{ef} and Q_{ef}.

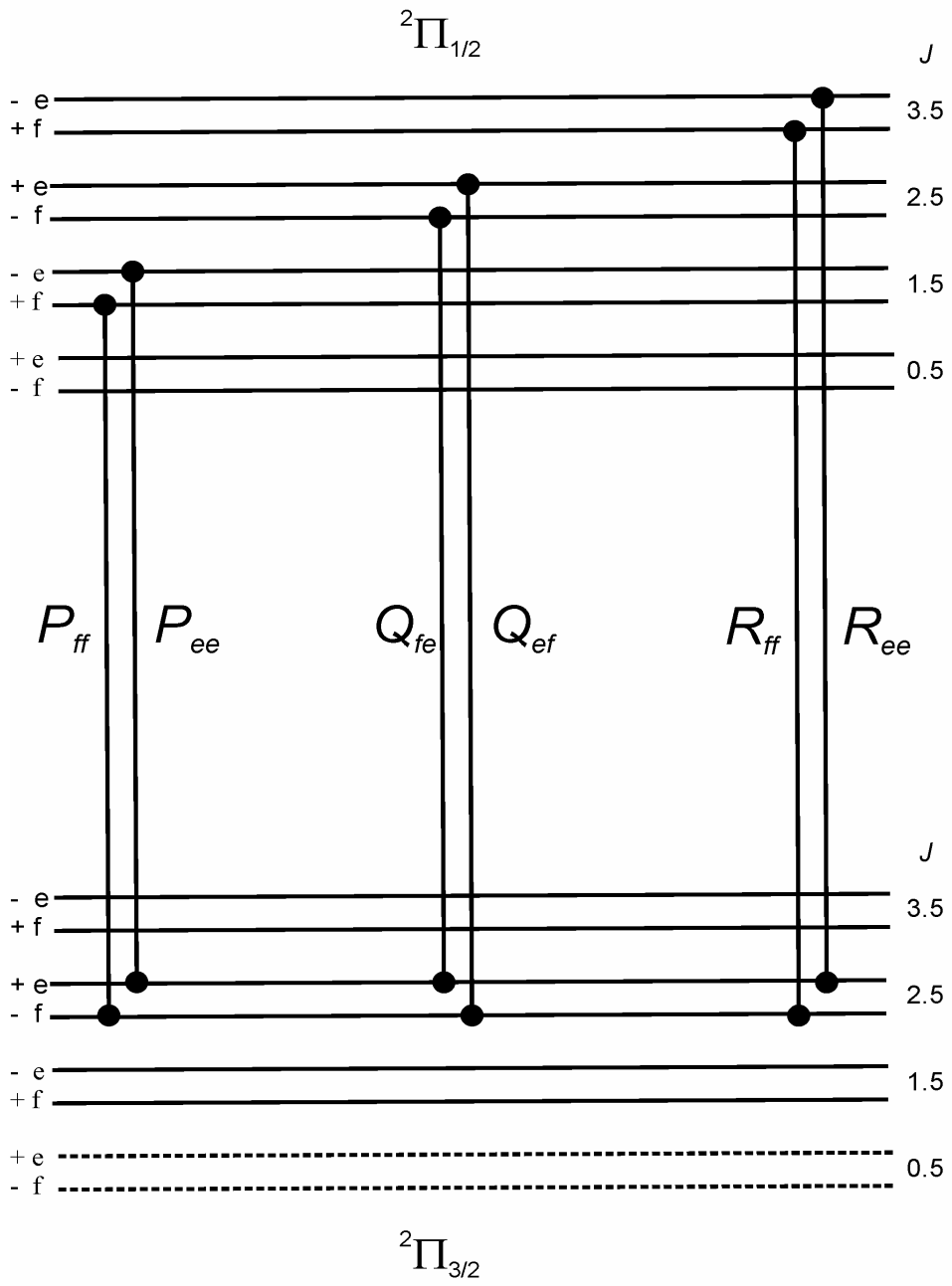

Figure 4.1 An energy level diagram of the $X\ ^2\Pi$ state of TeH. Each level is labeled by quantum number J, rotationless (e/f) parity and total (+/–) parity. Each rotational level is split into a doublet due to Λ-doubling. The six allowed branches of the $X\ ^2\Pi - X\ ^2\Pi$ transition are labeled by the branch notation $\Delta J_{P',P''}$ (P = e or f).

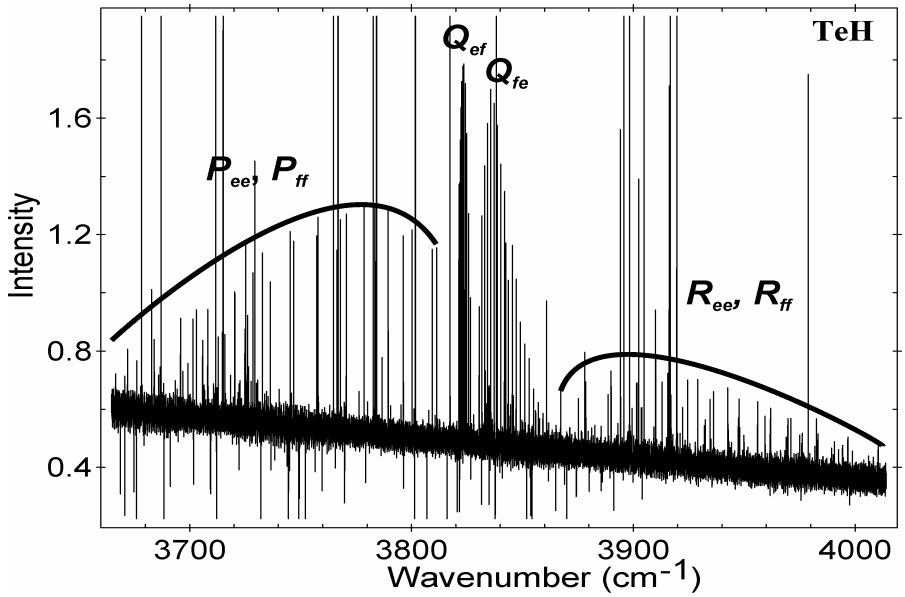

Figure 4.2 An overview of the $X\ ^2\Pi_{1/2} - X\ ^2\Pi_{3/2}$ transition of TeH recorded at a resolution of 0.01 cm^{-1}. The strong atomic lines are from argon, and the absorption lines are due to atmospheric H_2O vapor.

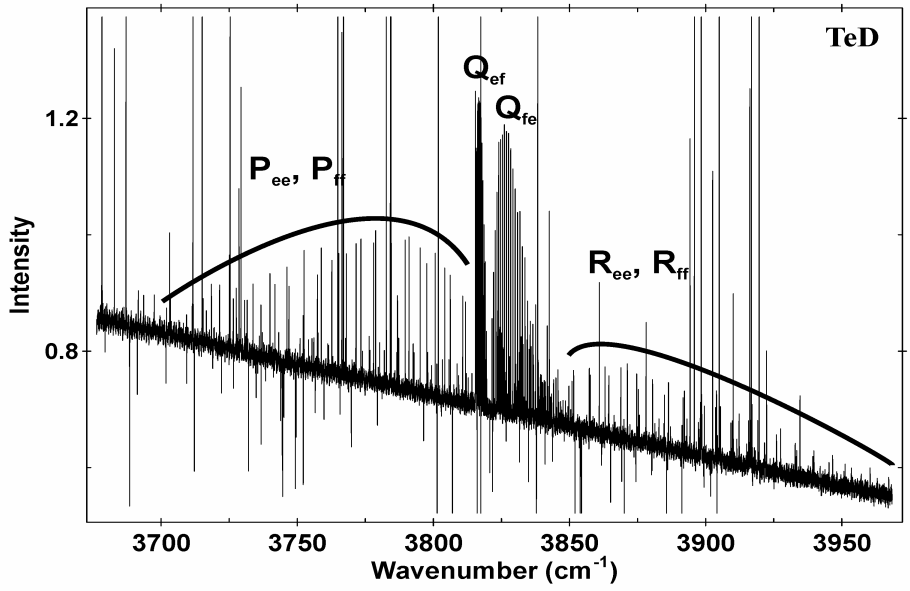

Figure 4.3 An overview of the $X\ ^2\Pi_{1/2} - X\ ^2\Pi_{3/2}$ transition of TeD recorded at a resolution of 0.02 cm^{-1}. The strong atomic lines are from argon, and the absorption lines are due to atmospheric H_2O vapor.

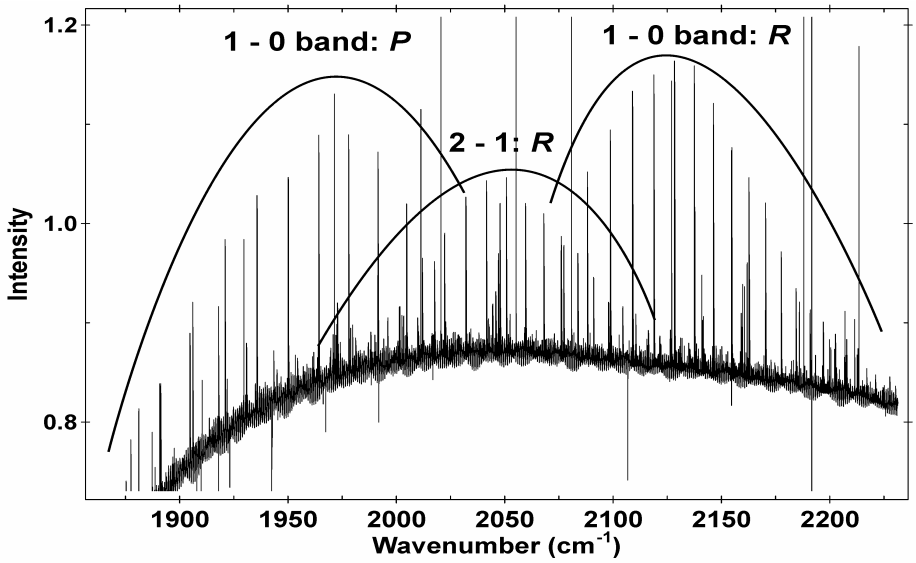

Figure 4.4 An overview of the infrared spectrum of the $X\ ^2\Pi_{3/2}$ spin component of TeH recorded at a resolution of 0.01 cm^{-1}.

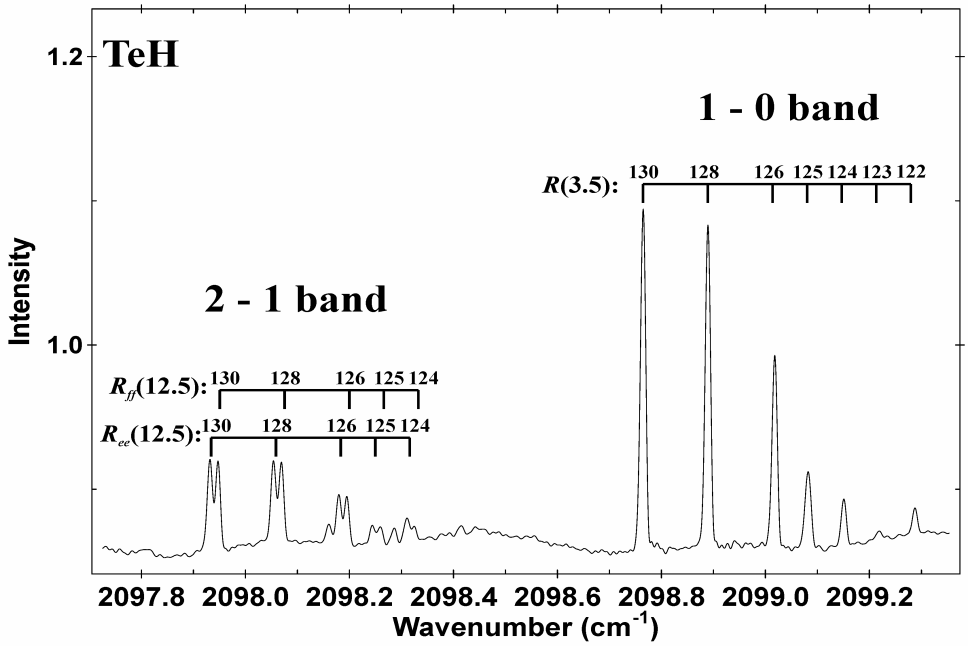

Figure 4.5 An expanded view of the infrared spectrum of the $X\ ^2\Pi_{3/2}$ spin component of TeH near 2098 cm^{-1}. The numbers on the top of the lines refer to the mass numbers of the tellurium atom. The low *J* line *R*(3.5) of the 1 – 0 band shows no *Λ*-doubling splitting, while the high *J* line *R*(12.5) of the 2 – 1 band shows *Λ*-doubling.

For the $X\,^2\Pi_{1/2} - X\,^2\Pi_{3/2}$ transition, all six branches were observed for the 0 – 0 and 1 – 1 bands of TeD and TeH. The TeD transition was relatively strong, and the doubled *Q* branches were also observed for its 2 – 2 band. Figures 4.2 and 4.3 show the overview spectra of the $X\,^2\Pi_{1/2} - X\,^2\Pi_{3/2}$ transition of TeH and TeD. The line positions agree well with those reported by Fink *et al*. [7] within their error limits of ±0.01 cm^{-1}, and many more lines were observed for both TeD and TeH. Since the $\Delta v = 0$ sequences of the $X\,^2\Pi_{1/2} - X\,^2\Pi_{3/2}$ system of TeH and TeD were observed, the isotopic splitting due to tellurium was only observed for a few high *J* lines in the *P* and *R* branches.

In the infrared region, extensive lines of the $X\,^2\Pi_{3/2}$ component were obtained for both TeD and TeH. The 1 – 0 and 2 – 1 bands were observed for the three most abundant isotopologues of TeD: ^{130}TeD, ^{128}TeD and ^{126}TeD. TeH lines were much stronger, and transitions for seven of the eight naturally occurring isotopologues of TeH were observed. The natural abundances of Te are: ^{130}Te: 33.80%, ^{128}Te: 31.69%, ^{126}Te: 18.95%, ^{125}Te: 7.14%, ^{124}Te: 4.816%, ^{123}Te: 0.908%, ^{122}Te: 2.60%, ^{120}Te: 0.096%. [16]. The 1 – 0, 2 – 1 and 3 – 2 bands were observed for the five most abundant isotopologues, the 1 – 0 and 2 – 1 bands for ^{122}TeH, and the 1 – 0 band for ^{123}TeH. Figures 4.4 and 4.5 show an overview and an expanded view of the TeH spectrum obtained. The *J* values of lines observed for the $X\,^2\Pi_{3/2}$ spin component were high enough so that the Λ-doubling splitting was resolved.

4.3.1 Hund's Case (a) Fits for ^{130}TeD, ^{128}TeD and ^{126}TeD

First, a least-squares fit was performed for each of the three main isotopologues of TeD. There was no problem in assigning the lines for all bands, except for the 2 – 2 band of the $X\,^2\Pi_{1/2} - X\,^2\Pi_{3/2}$ transition. Since only the two *Q* branches were observed for this band, the *J* assignments for these two branches were shifted until a reasonable *Λ*-doubling constant *p* and rotational constant *B* were obtained for v = 2. In addition to the present data, the following data set was also included in the fit: the $X\,^2\Pi_{1/2} - X\,^2\Pi_{3/2}$ lines from Fink *et al*. [7] and the predicted infrared laser magnetic resonance lines from Gillett *et al*. [9]. Because the absolute accuracy of the measurements of Fink *et al*. is about ±0.01 cm^{-1} [7], while that for the present data is 0.001 cm^{-1}, the strong TeD lines from the present experiment were used to recalibrate their line positions. Since the isotopic splitting due to tellurium was only observed for a few high *J* lines of the $X\,^2\Pi_{1/2} - X\,^2\Pi_{3/2}$ transition, the data were almost identical for ^{130}TeD, ^{128}TeD and ^{126}TeD.

The energy levels of the ground $X\,^2\Pi$ state of TeD were calculated by use of the Brown's $\hat{N}^2$ Hamiltonian matrix for $^2\Pi$ states with matrix elements derived using Hund's case (a) basis functions (see Chapter 1). An explicit listing of these matrix elements is provided in Section 1.4. The TeD data are fitted well by this model and the spectroscopic constants obtained are given in Table 4.1. The output files of the fits (including complete lists of all data) have been published in the supplementary tables of Ref. [14]. A systematic trend in the observed minus calculated line positions, caused by the unresolved tellurium isotopic lines of the $X\,^2\Pi_{1/2} - X\,^2\Pi_{3/2}$ transition, was found as expected for all bands of the $X\,^2\Pi_{1/2} - X\,^2\Pi_{3/2}$ transition. The same effect was noted in the previous study of SbH and SbD, and is discussed in more detail in Section 3.3.

Table 4.1 Hund's case (a) constants (in cm^{-1}) for the $X\ ^2\Pi$ state of ^{130}TeD, ^{128}TeD and ^{126}TeD.[a]

		v = 0	v = 1	v = 2
^{130}TeD	T_v	0	1473.87232(47)	2910.03175(73)
	A_v	-3814.34537(36)	-3822.14283(66)	-3829.87714(96)
	$10^3 A_{Dv}$	-7.9978(31)	-8.3034(89)	-8.5372(82)
	$10^8 A_{Hv}$	-5.39(22)	-3.9(12)	…
	B_v	3.070917(18)	3.012218(17)	2.953232(20)
	$10^5 D_v$	5.2396(62)	5.2319(56)	5.2357(83)
	$10^{10} H_v$	5.94(66)	5.87(53)	6.5(11)
	$10^4 q_v$	-8.75(58)	-8.47(64)	-8.64(90)
	p_v	1.02778(14)	1.00209(20)	0.97708(28)
	$10^5 p_{Dv}$	-5.447(50)	-5.277(64)	-5.78(13)
	$10^9 p_{Hv}$	2.22(55)	…	…
^{128}TeD	T_v	0	1474.04309(47)	2910.36069(72)
	A_v	-3814.34450(30)	-3822.14381(56)	-3829.87605(82)
	$10^3 A_{Dv}$	-7.9957(26)	-8.2907(74)	-8.5344(70)
	$10^8 A_{Hv}$	-5.41(18)	-4.40(99)	…
	B_v	3.071454(16)	3.012736(15)	2.953773(18)
	$10^5 D_v$	5.1971(57)	5.1875(50)	5.2045(79)
	$10^{10} H_v$	2.76(61)	2.14(49)	3.7(11)
	$10^4 q_v$	-8.01(52)	-7.87(60)	-9.07(84)
	p_v	1.02766(13)	1.00207(18)	0.97717(25)
	$10^5 p_{Dv}$	-5.429(43)	-5.292(55)	-5.77(11)
	$10^9 p_{Hv}$	1.90(47)	…	…
^{126}TeD	T_v	0	1474.21983(50)	2910.70733(70)
	A_v	-3814.34298(34)	-3822.14229(63)	-3829.87440(76)
	$10^3 A_{Dv}$	-7.9954(29)	-8.2837(78)	-8.5337(65)
	$10^8 A_{Hv}$	-5.10(20)	-5.1(10)	…
	B_v	3.072370(19)	3.013634(20)	2.954634(25)
	$10^5 D_v$	5.2645(85)	5.2590(88)	5.282(13)
	$10^9 H_v$	1.10(11)	1.09(11)	1.50(18)
	p_v	1.026062(87)	1.00052(13)	0.97537(17)
	$10^5 p_{Dv}$	-5.450(45)	-5.317(56)	-5.79(10)
	$10^9 p_{Hv}$	2.26(48)	…	…

[a] All uncertainties are 1σ.

Table 4.2 Hund's case (c) constants (in cm^{-1}) for the $X\ ^2\Pi$ state of ^{130}TeD, ^{128}TeD and ^{126}TeD.[a]

		v = 0	v = 1	v = 2
^{130}TeD $X\ ^2\Pi_{3/2}$	T_v	0	1470.01765(29)	2902.35417(52)
	B_v	3.064474(18)	3.005721(17)	2.946715(20)
	$10^5 D_v$	5.2268(62)	5.2182(55)	5.2185(83)
	$10^{10} H_v$	5.81(66)	5.76(54)	6.4(11)
	$10^6 p_{Dv}$	-2.141(89)	-2.017(97)	-1.97(13)
^{130}TeD $X\ ^2\Pi_{1/2}$	T_v	3820.48543(42)	5298.18307(85)	6738.1350(21)
	B_v	3.077200(19)	3.018566(24)	2.959645(60)
	$10^5 D_v$	5.2505(66)	5.250(11)	5.298(42)
	$10^{10} H_v$	5.89(69)	6.7(14)	16.9(84)
	p_v	-1.025696(62)	-1.00037(15)	-0.97541(28)
	$10^5 p_{Dv}$	5.468(15)	5.492(68)	6.06(19)
^{128}TeD $X\ ^2\Pi_{3/2}$	T_v	0	1470.18749(35)	2902.68322(57)
	B_v	3.065012(16)	3.006245(15)	2.947256(18)
	$10^5 D_v$	5.1846(57)	5.1746(49)	5.1874(79)
	$10^{10} H_v$	2.63(62)	2.05(49)	3.5(11)
	$10^6 p_{Dv}$	-2.008(81)	-1.911(91)	-2.03(13)
^{128}TeD $X\ ^2\Pi_{1/2}$	T_v	3820.48581(35)	5298.35494(77)	6738.4641(18)
	B_v	3.077734(17)	3.019081(21)	2.960186(52)
	$10^5 D_v$	5.2064(60)	5.2053(91)	5.266(36)
	$10^{10} H_v$	2.53(64)	3.0(12)	14.0(72)
	p_v	-1.025771(51)	-1.00047(12)	-0.97541(24)
	$10^5 p_{Dv}$	5.468(14)	5.495(58)	6.07(16)
^{126}TeD $X\ ^2\Pi_{3/2}$	T_v	0	1470.36410(34)	2903.02990(55)
	B_v	3.065904(19)	3.007130(19)	2.948098(24)
	$10^5 D_v$	5.2373(87)	5.2368(87)	5.252(13)
	$10^{10} H_v$	8.7(11)	9.4(11)	12.9(17)
	$10^6 p_{Dv}$	-1.54(16)	-1.50(17)	-1.73(23)
^{126}TeD $X\ ^2\Pi_{1/2}$	T_v	3820.48626(38)	5298.53203(86)	6738.8106(16)
	B_v	3.078623(20)	3.019951(25)	2.961032(49)
	$10^5 D_v$	5.2587(89)	5.262(12)	5.335(34)
	$10^{10} H_v$	8.6(12)	9.7(15)	24.3(66)
	p_v	-1.025736(53)	-1.00047(13)	-0.97542(21)
	$10^5 p_{Dv}$	5.409(19)	5.470(60)	6.05(15)

[a] All uncertainties are 1σ.

4.3.2 Hund's Case (c) Fits for ^{130}TeD, ^{128}TeD and ^{126}TeD

A Hund's case (c) fit was also performed for each of three observed isotopologues of TeD. In this case, the energy levels of the $X\,^2\Pi_{1/2}$ and $X\,^2\Pi_{3/2}$ spin components were fitted separately using the following expression, which was described in Section 1.4,

$$F(J) = T_v + B_v J(J+1) - D_v[J(J+1)]^2 + H_v[J(J+1)]^3 \pm \tfrac{1}{2}[p_v(J+1/2) + p_{Dv}(J+1/2)^3 + p_{Hv}(J+1/2)^5], \quad (4.1)$$

with $p_v = 0$ for the $X\,^2\Pi_{3/2}$ spin component (p_v, p_{Dv} and p_{Hv} are the Λ-doubling constants). Data for the three isotopologues of TeD are also well described by this model, and the obtained spectroscopic constants are given in Table 4.2.

4.3.3 Hund's Case (a) Fits for ^{130}TeH, ^{128}TeH, ^{126}TeH, ^{125}TeH, ^{124}TeH, ^{123}TeH and ^{122}TeH

An attempt was made to analyze the TeH data in the same way. It was found that the Hund's case (a) model cannot fit the TeH data. It was necessary to deweight lines with $J > 16.5$ from the 0 – 0 band of the $X\,^2\Pi_{1/2} - X\,^2\Pi_{3/2}$ transition and from the 2 – 1 vibration-rotation band of the $X\,^2\Pi_{3/2}$ spin component. The lines of the 1 – 1 band of the $X\,^2\Pi_{1/2} - X\,^2\Pi_{3/2}$ transition stop abruptly. For the 3 – 2 band of the $X\,^2\Pi_{3/2}$ spin component, just a few *R* branches lines can be fitted, but there are almost one hundred lines in this region (these lines appear as strong quintets, and are from the five most abundant isotopologues of TeH) and there are no *Λ*-doubling patterns as were observed in the 1 – 0 and 2 – 1 bands of the $X\,^2\Pi_{3/2}$ component.

Similar problems in the infrared spectra of SeD were found by Ashworth *et al*. [18], and more weakly for SeH by Ram *et al*. [19]. The problems are all associated with strong perturbations in the spectra. TeH has a large spin-orbit splitting of about 3800 cm^{-1}, and the band origin of the 2 – 0 vibration-rotation band of the $X\,^2\Pi_{3/2}$ spin component is around 4000 cm^{-1}. The $X\,^2\Pi_{1/2}$, v = 0 and $X\,^2\Pi_{3/2}$, v = 2 levels thus lie close to each other, and can interact. The obtained ^{128}TeH constants of v = 0 and 1 were used to extrapolate the constants for v = 2, 3 and 4, and then used to predict the term values for the $X\,^2\Pi$ state of ^{128}TeH. Figure 4.6 shows these term values plotted against $(J+1/2)(J+3/2)$. It turns out that $X\,^2\Pi_{1/2}$, v = 0 and $X\,^2\Pi_{3/2}$, v = 2 cross at around $J = 24.5$, and $X\,^2\Pi_{1/2}$, v = 1 and $X\,^2\Pi_{3/2}$, v = 3 cross at around $J = 7.5$. It is necessary to take these strong perturbations into account in order to obtain a successful fit for TeH.

The usual Hund's case (a) matrix for a $^2\Pi$ state was modified, and the following 4×4 matrix was constructed:

$$\widehat{\mathbf{H}} = \begin{pmatrix} H_{11} & H_{12} & H_{13} & H_{14} \\ H_{12} & H_{22} & H_{14} & H_{24} \\ H_{13} & H_{14} & H_{33} & H_{34} \\ H_{14} & H_{24} & H_{34} & H_{44} \end{pmatrix} \quad (4.2)$$

to calculate the energy levels for the v = 0, 1, 2 and 3 of the $X\,^2\Pi_{3/2}$ and $X\,^2\Pi_{1/2}$ components. The matrix elements for v = 0 and v = 2 are now in one 4×4 matrix, and the same is true for v = 1 and v = 3. In Eq. (4.2), H_{11}, H_{12} and H_{22} are the usual case (a) matrix elements for v = 0 or v = 1, and H_{33}, H_{34} and H_{44} are the usual case (a) matrix elements for v = 2 or v = 3. H_{13}, H_{14} and H_{24} are the

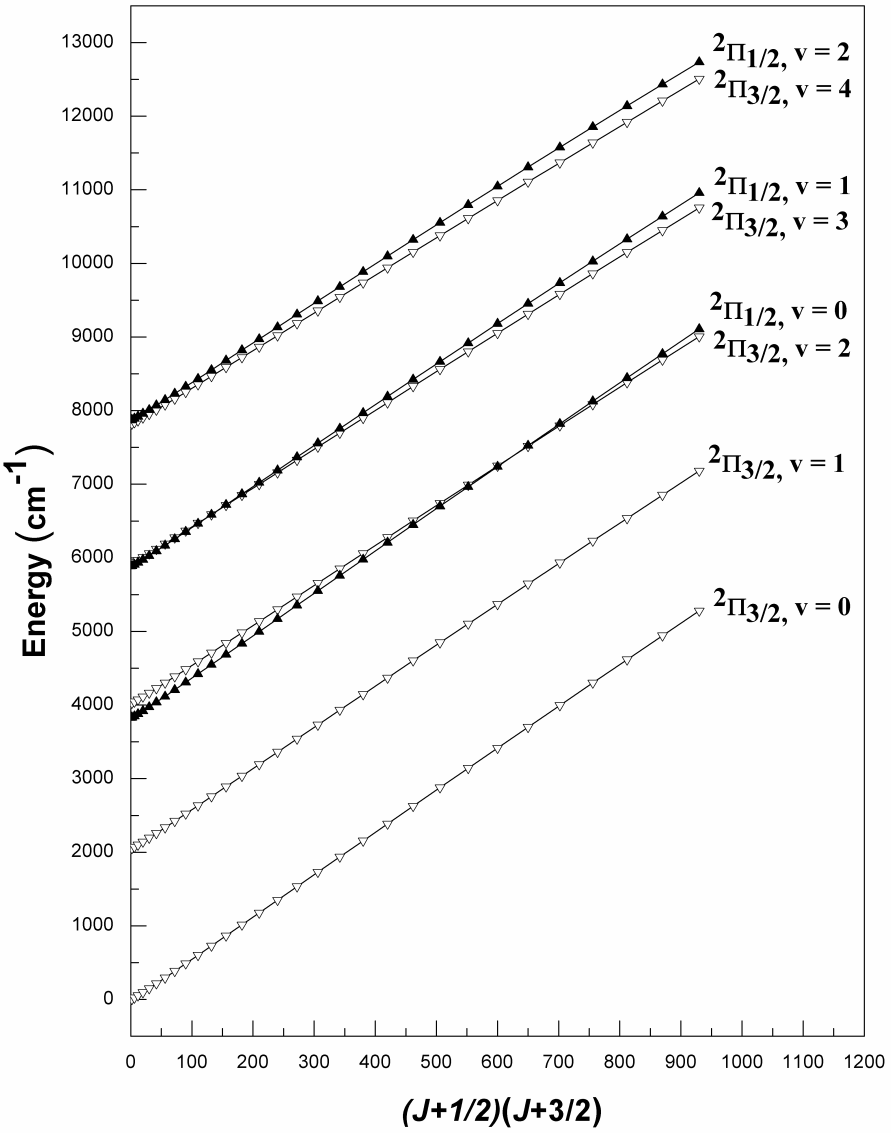

Figure 4.6 Term values of the ground $X\ ^2\Pi$ state plotted against $(J+1/2)(J+3/2)$, which shows that $X\ ^2\Pi_{1/2}$, v = 0 and $X\ ^2\Pi_{3/2}$ v = 2 cross at around $J = 24.5$ and $X\ ^2\Pi_{1/2}$, v = 1 and $X\ ^2\Pi_{3/2}$, v = 3 cross at around $J = 7.5$.

vibrational perturbation terms which account for the interaction of $X\,^2\Pi_{1/2}$, v = 0 (or $X\,^2\Pi_{1/2}$, v = 1) and $X\,^2\Pi_{3/2}$, v = 2 (or $X^2\Pi_{3/2}$, v = 3).

Brown's $\hat{N}^2$ effective rotational Hamiltonian [20] was used,

$$\hat{H}_{\rm rot}^{\,eff} = B\hat{N}^2 - D\hat{N}^4 \tag{4.3}$$

to derive the following matrix elements:

$$H_{13} = \left\langle {}^2\Pi_{1/2}, \mathrm{v}\left| H_{\rm rot}^{\,eff} \right| {}^2\Pi_{1/2}, \mathrm{v'} \right\rangle = B_{\mathrm{v'v''}}(\mathrm{x} + \tfrac{5}{4}) - D_{\mathrm{v'v''}}(\mathrm{x}^2 + \tfrac{7}{2}\mathrm{x} + \tfrac{13}{16}), \tag{4.4}$$

$$H_{14} = \left\langle {}^2\Pi_{1/2}, \mathrm{v}\left| H_{\rm rot}^{\,eff} \right| {}^2\Pi_{3/2}, \mathrm{v'} \right\rangle = -B_{\mathrm{v'v''}}\sqrt{(\mathrm{x} - \tfrac{3}{4})} + D_{\mathrm{v'v''}}(\mathrm{x} + \tfrac{1}{4})\sqrt{(4\mathrm{x} - 3)}\,, \tag{4.5}$$

$$H_{24} = \left\langle {}^2\Pi_{3/2}, \mathrm{v}\left| H_{\rm rot}^{\,eff} \right| {}^2\Pi_{3/2}, \mathrm{v'} \right\rangle = B_{\mathrm{v'v''}}(\mathrm{x} - \tfrac{3}{4}) - D_{\mathrm{v'v''}}(\mathrm{x}^2 + \tfrac{1}{2}\mathrm{x} + \tfrac{3}{16}), \tag{4.6}$$

where x = J(J+1). The $B_{\mathrm{v'v''}}$ and $D_{\mathrm{v'v''}}$ constants account for the vibrational perturbation between $X\,^2\Pi_{1/2}$, v = v' and $X\,^2\Pi_{3/2}$, v = v''. The rotational dependence of the 2×2 perturbation matrix is the same as in the usual 2×2 block for a $^2\Pi$ state on the diagonal.

After the perturbation terms were included in the matrix, all the lines can be fitted easily, including those that caused problems in the previous fits with the usual case (a) matrix. The constants obtained are given in Tables 4.3 – 4.6, where B_{02} and D_{02} are the constants which account for the vibrational perturbation between $X^2\Pi_{1/2}$, v = 0 and $X\,^2\Pi_{3/2}$, v = 2, and B_{13} and D_{13} for the vibrational perturbation between $X\,^2\Pi_{1/2}$, v = 1 and $X\,^2\Pi_{3/2}$, v = 3. The output files of the fits (including complete lists of all data) have been published in the supplementary tables of Ref. [14].

For the five most abundant isotopologues of TeH, the fits included data from the present experiments (1 – 0, 2 – 1 and 3 – 2 bands of the $X\,^2\Pi_{3/2}$ component, the 0 – 0 and 1 – 1 bands of the $X\,^2\Pi_{1/2} - X\,^2\Pi_{3/2}$ transition), recalibrated data from Fink *et al*. [7] (the 2 – 0 band of the $X\,^2\Pi_{3/2}$ component, the 0 – 0 and 1 – 1 bands of the $X\,^2\Pi_{1/2} - X\,^2\Pi_{3/2}$ transition), and data from Gillett *et al*. [9] (calculated lines matching the observations for the 1 – 0 and 2 – 1 bands of the $X\,^2\Pi_{3/2}$ component). Because the 2 – 2 and 3 – 3 bands of the $X\,^2\Pi_{1/2} - X\,^2\Pi_{3/2}$ transition were not observed for all the isotopologues of TeH, the spin-orbit constants and Λ-doubling constants cannot be determined for the v = 2 and 3 levels. Therefore, the A, $A_{\rm D}$, p and $p_{\rm D}$ were fixed for v = 2 and 3 levels for all the isotopologues of TeH.

The constants $A_{\rm v}$, $A_{\rm Dv}$, $p_{\rm v}$ and $p_{\rm Dv}$ (v = 0, 1 and 2) from the Hund's case (a) fits for ^{128}TeD were used to derive the equilibrium constants A_{lm} and p_{lm} for ^{128}TeD using the following formulas:

$$A_{\rm v} = \sum_{l=0}^{l=2} A_{l0}(\mathrm{v} + \tfrac{1}{2})^l \;; \tag{4.7}$$

$$A_{\rm Dv} = \sum_{l=0}^{l=2} A_{l1}(\mathrm{v} + \tfrac{1}{2})^l \;; \tag{4.8}$$

$$p_{\rm v} = \sum_{l=0}^{l=2} p_{l1}(\mathrm{v} + \tfrac{1}{2})^l \;; \tag{4.9}$$

$$p_{\rm Dv} = \sum_{l=0}^{l=1} p_{l2}(\mathrm{v} + \tfrac{1}{2})^l \;. \tag{4.10}$$

The resulting equilibrium constants for ^{128}TeD were used to derive the corresponding equilibrium constants for all the isotopologues of TeH *via*:

$$A_{lm}^{(\alpha)} = A_{lm}^{(1)}\left(\frac{\mu_1}{\mu_\alpha}\right)^{m+l/2}, \tag{4.11}$$

$$p_{lm}^{(\alpha)} = p_{lm}^{(1)}\left(\frac{\mu_1}{\mu_\alpha}\right)^{m+l/2}, \tag{4.12}$$

in which the superscript "(1)" is an index for ^{128}TeD, and the superscript "(α)" is the index for the isotopologue of TeH. The constant μ_1 is the reduced mass of ^{128}TeD and μ_α is the reduced mass of isotopologue α of TeH. The resulting equilibrium constants were used to calculate the fixed values for A_v, A_{Dv}, p_v and p_{Dv} in the case (a) fits using Eq. (4.7) to Eq. (4.10).

The 3 – 2 band of the $X\,^2\Pi_{3/2}$ component was not observed for ^{122}TeH and ^{123}TeH, and 2 – 1 band of the $X\,^2\Pi_{3/2}$ component was also not observed for ^{123}TeH, so the T_v, B_v, D_v and H_v needed for the fit were fixed at values calculated from the corresponding equilibrium constants of ^{128}TeH similar to the way used to obtain the fixed values of A, A_D, p and p_D for v = 2 and 3 levels of the isotopologues of TeH.

Values for the vibrational perturbation constants B_{02} and B_{13} of ^{128}TeH were estimated to verify the experimental ones in the following way: the equilibrium constants derived from the fitted parameters in the case (c) fit of ^{128}TeH were used to calculate the RKR potentials for the spin components of the ground $X\,^2\Pi$ state using Le Roy's RKR1 program [21]; the two resulting potentials were used to calculate B_{02},

$$B_{02} = (-\hbar^2/2\mu)\left\langle {}^2\Pi_{1/2}, \mathrm{v}=0 \left| 1/R^2 \right| {}^2\Pi_{3/2}, \mathrm{v}=2 \right\rangle, \tag{4.13}$$

and B_{13},

$$B_{13} = (-\hbar^2/2\mu)\left\langle {}^2\Pi_{1/2}, \mathrm{v}=1 \left| 1/R^2 \right| {}^2\Pi_{3/2}, \mathrm{v}=3 \right\rangle, \tag{4.14}$$

using Le Roy's LEVEL program [22]. A value of 0.16 was obtained for B_{02} and 0.27 for B_{13}. If the parameters in the case (a) fit of ^{128}TeH were used instead, calculated values of 0.13 for B_{02} and 0.22 for B_{13} were obtained. The experimental values of 0.2596 for B_{02} and 0.26349 for B_{13} are therefore quite reasonable.

4.3.4 Hund's Case (c) Fits for ^{130}TeH, ^{128}TeH, ^{126}TeH, ^{125}TeH, ^{124}TeH, ^{123}TeH and ^{122}TeH

A Hund's case (c) fit was also performed for each isotopologue of TeH. The energy expression of the ground $X\,^2\Pi$ state was represented in the same way (Eq. (4.1)) as in the case (c) fits of ^{130}TeD, ^{128}TeD and ^{126}TeD. The data for the isotopologues of TeH are not well described by this model, and the perturbed lines were simply deweighted in these fits. The obtained spectroscopic constants are given in Tables 4.7 – 4.10.

Table 4.3 Hund's case (a) constants (in cm^{-1}) for the $X\,^2\Pi$ state of ^{130}TeH and ^{128}TeH.[a]

	Constants	v = 0	v = 1	v = 2	v = 3	Vibrational [c] perturbation
^{130}TeH	T_v	0	2053.83998(50)	4032.35331(45)	5935.07609(56)	
	A_v	-3816.38124(42)	-3827.33580(70)	-3837.69552[b]	-3848.37276[b]	
	$10^2 A_{Dv}$	-1.76111(89)	-1.8189(13)	-1.7306[b]	-1.7662[b]	
	$10^7 A_{Hv}$	1.47(12)	…	…	…	
	B_v	6.065439(26)	5.900939(23)	5.734325(20)	5.567038(20)	
	$10^4 D_v$	1.8881(17)	1.8688(16)	2.2095(28)	2.2309(13)	
	$10^9 H_v$	-9.95(35)	14.03(37)	16.04(45)	-9.33(27)	
	$10^3 q_v$	-3.924(39)	-4.262(37)	-3.088(60)	-4.622(62)	
	$10^7 q_{Dv}$	-1.28(58)	…	…	…	
	p_v	2.02931(17)	1.95907(29)	1.88869[b]	1.82367[b]	
	$10^4 p_{Dv}$	-2.088(17)	-2.143(29)	-1.957[b]	-1.871 [b]	
	$10^8 p_{Hv}$	1.91(41)	…	…	…	
	B_{02}					0.2572(17)
	$10^4 D_{02}$					1.227(19)
	B_{13}					0.26325(17)
	$10^5 D_{13}$					-6.230(85)
^{128}TeH	T_v	0	2053.95854(44)	4032.58234(42)	5935.40571(53)	
	A_v	-3816.38049(40)	-3827.33544(58)	-3837.69714 [b]	-3848.375 [b]	
	$10^2 A_{Dv}$	-1.76073(83)	-1.8202(11)	-1.7308 [b]	-1.7664 [b]	
	$10^7 A_{Hv}$	1.41(11)	…	…	…	
	B_v	6.066088(23)	5.901570(21)	5.734926(19)	5.567631(19)	
	$10^4 D_v$	1.8872(16)	1.8699(16)	2.2138(26)	2.2328(12)	
	$10^9 H_v$	-9.81(33)	14.14(34)	16.52(41)	-9.05(24)	
	$10^3 q_v$	-3.745(71)	-4.110(65)	-2.840(69)	-4.470(65)	
	$10^7 q_{Dv}$	-2.87(53)	…	…	…	
	p_v	2.02928(20)	1.95877(27)	1.88891 [b]	1.82387 [b]	
	$10^4 p_{Dv}$	-2.110(16)	-2.183(25)	-1.958 [b]	-1.872 [b]	
	$10^8 p_{Hv}$	2.50(38)	…	…	…	
	B_{02}					0.2596(15)
	$10^4 D_{02}$					1.247(17)
	B_{13}					0.26349(15)
	$10^5 D_{13}$					-6.115(74)

[a] All uncertainties are 1σ.
[b] Fixed at values calculated from the corresponding constants of ^{128}TeD by reduced mass relationships (see text).
[c] $B_{v'v''}$ and $D_{v'v''}$ are constants that account for the perturbation between the $X\,^2\Pi_{1/2}$ and $X\,^2\Pi_{3/2}$ components (see text).

Table 4.4 Hund's case (a) constants (in cm^{-1}) for the $X\,^2\Pi$ state of ^{126}TeH and ^{125}TeH.[a]

	Constants	v = 0	v = 1	v = 2	v = 3	Vibrational [c] perturbation
^{126}TeH	T_v	0	2054.08089(60)	4032.81886(51)	5935.74617(64)	
	A_v	-3816.37977(50)	-3827.33452(86)	-3837.69881[b]	-3848.37731[b]	
	$10^2 A_{Dv}$	-1.7556(12)	-1.8184(14)	-1.731[b]	-1.767[b]	
	$10^7 A_{Hv}$	1.06(15)	…	…	…	
	B_v	6.066713(31)	5.902200(28)	5.735589(23)	5.568239(25)	
	$10^4 D_v$	1.8928(23)	1.8609(23)	2.1916(45)	2.2308(18)	
	$10^9 H_v$	-9.70(57)	12.27(63)	13.45(79)	-8.90(41)	
	$10^3 q_v$	-3.51(2)	-3.88(11)	-2.84(11)	-4.36(10)	
	p_v	2.02860(31)	1.95800(41)	1.88913[b]	1.82409[b]	
	$10^4 p_{Dv}$	-2.101(19)	-2.154(33)	-1.958[b]	-1.872[b]	
	$10^8 p_{Hv}$	1.89(45)	…	…	…	
	B_{02}					0.2457(27)
	$10^4 D_{02}$					1.095(31)
	B_{13}					0.26405(19)
	$10^5 D_{13}$					-5.828(96)
^{125}TeH	T_v	0	2054.14381(56)	4032.94142(50)	5935.92060(68)	
	A_v	-3816.37823(41)	-3827.33372(85)	-3837.69967[b]	-3848.37849[b]	
	$10^2 A_{Dv}$	-1.7501(11)	-1.8120(20)	-1.7312[b]	-1.7667[b]	
	$10^7 A_{Hv}$	2.57(17)	…	…	…	
	B_v	6.067095(29)	5.902545(26)	5.735980(23)	5.568570(24)	
	$10^4 D_v$	1.9383(28)	1.8605(20)	2.1408(50)	2.2281(20)	
	$10^9 H_v$	-9.73(47)	10.98(51)	9.95(68)	-9.90(51)	
	$10^3 q_v$	-0.72(22)	-1.40(20)	-1.56(19)	-2.54(16)	
	p_v	2.02286(46)	1.95261(50)	1.88925[b]	1.82419[b]	
	$10^4 p_{Dv}$	-2.0736(52)	-2.051(36)	-1.958[b]	-1.872[b]	
	B_{02}					0.2066(45)
	$10^4 D_{02}$					1.099(36)
	B_{13}					0.26333(19)
	$10^5 D_{13}$					-6.054(93)

[a] All uncertainties are 1σ.
[b] Fixed at values calculated from the corresponding constants of ^{128}TeD by reduced mass relationships (see text).
[c] $B_{v'v''}$ and $D_{v'v''}$ are constants that account for the perturbation between the $X\,^2\Pi_{1/2}$ and $X\,^2\Pi_{3/2}$ components (see text).

Table 4.5 Hund's case (a) constants (in cm^{-1}) for the $X\ ^2\Pi$ state of ^{124}TeH and ^{123}TeH.[a]

	Constants	v = 0	v = 1	v = 2	v = 3	Vibrational [d] perturbation
^{124}TeH	T_v	0	2054.20799(52)	4033.06454(38)	5936.09814(60)	
	A_v	-3816.37858(31)	-3827.33385(89)	-3837.70053 [b]	-3848.37969 [b]	
	$10^2\ A_{Dv}$	-1.74447(61)	-1.8071(29)	-1.7313 [b]	-1.7668 [b]	
	B_v	6.067486(21)	5.902936(26)	5.736393(21)	5.569182(19)	
	$10^4\ D_v$	1.9376(36)	1.8615(16)	2.1452(36)	2.2604(10)	
	$10^9\ H_v$	-5.37(74)	10.68(52)	5.75(55)	…	
	$10^3\ q_v$	0.858(13)	…	…	…	
	p_v	2.01978(13)	1.94928(29)	1.88937 [b]	1.82430 [b]	
	$10^4\ p_{Dv}$	-2.095(15)	-1.952(44)	-1.959 [b]	-1.873 [b]	
	$10^8\ p_{Hv}$	1.35(38)	…	…	…	
	B_{02}					0.2053(31)
	$10^5\ D_{02}$					6.24(36)
	B_{13}					0.26469(61)
	$10^5\ D_{13}$					-5.46(32)
^{123}TeH	T_v	0	2054.27200(50)	4033.35389 [c]	5936.44356 [c]	
	A_v	-3816.37783(24)	-3827.33466(66)	-3837.70141 [b]	-3848.38091 [b]	
	$10^2\ A_{Dv}$	-1.7529(57)	-1.8163(26)	-1.7314 [b]	-1.7669 [b]	
	B_v	6.067958(43)	5.903456(41)	5.736875 [c]	5.569242 [c]	
	$10^4\ D_v$	1.891(33)	1.8510(22)	2.2152 [c]	2.2342 [c]	
	$10^9\ H_v$	-12.2(44)	…	…	…	
	$10^3\ q_v$	1.29(44)	1.08(39)	4.47 [c]	4.47 [c]	
	p_v	2.01895(88)	1.94671(81)	1.88948 [b]	1.82442 [b]	
	$10^4\ p_{Dv}$	-2.094(11)	-1.751(35)	-1.959 [b]	-1.873 [b]	
	$10^8\ p_{Hv}$	1.85(48)	…	…	…	
	B_{02}					0.248(26)
	$10^4\ D_{02}$					1.04(22)
	B_{13}					0.2802(14)
	$10^5\ D_{13}$					4.27(91)

[a] All uncertainties are 1σ.
[b] Fixed at values calculated from the corresponding constants of ^{128}TeD by reduced mass relationships (see text).
[c] Fixed at values calculated from the corresponding constants of ^{128}TeH by reduced mass relationships (see text).
[d] $B_{v'v''}$ and $D_{v'v''}$ are constants that account for the perturbation between the $X^2\Pi_{1/2}$ and $X^2\Pi_{3/2}$ components (see text).

Table 4.6 Hund's case (a) constants (in cm^{-1}) for the $X\,^2\Pi$ state of ^{122}TeH.[a]

	Constants	v = 0	v = 1	v = 2	v = 3	Vibrational [d] perturbation
^{122}TeH	T_v	0	2054.34030(43)	4033.31887(42)	5936.66158[c]	
	A_v	-3816.37541(34)	-3827.33397(64)	-3837.70231[b]	-3848.38215 [b]	
	$10^2 A_{Dv}$	-1.839(12)	-1.7562(34)	-1.7315 [b]	-1.7671 [b]	
	$10^7 A_{Hv}$	5.91(96)	…	…	…	
	B_v	6.068834(67)	5.903524(20)	5.73618(12)	5.577838 [c]	
	$10^4 D_v$	1.479(56)	1.9119(51)	2.612(55)	2.2345 [c]	
	$10^9 H_v$	-68.2(84)	42.2(32)	7.15(82)	…	
	$10^3 q_v$	1.42(19)	1.29(19)	4.92(47)	-4.47 [c]	
	p_v	2.01873(40)	1.94640(45)	1.88961 [b]	1.82453 [b]	
	$10^4 p_{Dv}$	-2.033(15)	-2.300(74)	-1.959 [b]	-1.873 [b]	
	$10^8 p_{Hv}$	3.86(37)				
	B_{02}					0.486(24)
	$10^4 D_{02}$					3.49(26)
	B_{13}					0.2378(25)
	$10^4 D_{13}$					-2.50(19)

[a] All uncertainties are 1σ.
[b] Fixed at values calculated from the corresponding constants of ^{128}TeD by reduced mass relationships (see text).
[c] Fixed at values calculated from the corresponding constants of ^{128}TeH by reduced mass relationships (see text).
[d] $B_{v'v''}$ and $D_{v'v''}$ are constants that account for the perturbation between the $X\,^2\Pi_{1/2}$ and $X\,^2\Pi_{3/2}$ components (see text).

Table 4.7 Hund's case (c) constants (in cm^{-1}) for the $X\,^2\Pi$ state of ^{130}TeH.[a]

	Constants	v = 0	v = 1	v = 2	v = 3
^{130}TeH $X\,^2\Pi_{3/2}$	T_v	0	2048.48616(26)	4021.94331(38)	5919.4523(13)
	B_v	6.047146(19)	5.882885(19)	5.717585(21)	5.55236(26)
	$10^4 D_v$	2.0379(11)	2.0339(12)	2.0367(14)	1.88(15)
	$10^9 H_v$	3.51(30)	3.07(27)	4.59(32)	0.00114(24)
	$10^5 p_{Dv}$	-1.731(13)	-1.764(12)	-1.561(63)	6.1(18)
	$10^5 p_{Hv}$	…	0.000060(14)	-0.00206(27)	-1.371(54)
^{130}TeH $X\,^2\Pi_{1/2}$	T_v	3828.50370(47)	5887.6139(18)		
	B_v	6.082728(19)	5.91647(36)		
	$10^4 D_v$	2.05709(77)	2.14(19)		
	$10^6 H_v$	…	-1.70(26)		
	p_v	-2.02124(11)	-1.9473(11)		
	$10^4 p_{Dv}$	2.2888(69)	-1.94(91)		
	$10^5 p_{Hv}$	…	2.47(15)		

[a] All uncertainties are 1σ.

Table 4.8 Hund's case (c) constants (in cm^{-1}) for the $X\ ^2\Pi$ state of ^{128}TeH and ^{126}TeH.[a]

	Constants	v = 0	v = 1	v = 2	v = 3
^{128}TeH $X\ ^2\Pi_{3/2}$	T_v	0	2048.60423(23)	4022.17104(36)	5919.7802(12)
	B_v	6.047765(16)	5.883491(17)	5.718165(20)	5.55276(25)
	$10^4 D_v$	2.0376(11)	2.0339(11)	2.0359(15)	1.73(14)
	$10^7 H_v$	0.0349(27)	0.0307(24)	0.0429(37)	8.4(21)
	$10^5 p_{Dv}$	-1.648(25)	-1.708(22)	-1.342(80)	7.6(18)
	$10^5 p_{Hv}$	…	0.000098(12)	-0.00279(36)	-1.387(55)
^{128}TeH $X\ ^2\Pi_{1/2}$	T_v	3828.50456(42)	5887.7340(14)		
	B_v	6.083329(17)	5.91679(26)		
	$10^4 D_v$	2.05604(56)	1.95(13)		
	$10^6 H_v$	…	-1.91(18)		
	p_v	-2.021480(99)	-1.94615(89)		
	$10^4 p_{Dv}$	2.2945(63)	-3.07(69)		
	$10^5 p_{Hv}$	…	2.56(12)		
^{126}TeH $X\ ^2\Pi_{3/2}$	T_v	0	2048.72721(28)	4022.40677(42)	5920.1184(15)
	B_v	6.048499(20)	5.884190(20)	5.718856(22)	5.55387(32)
	$10^4 D_v$	2.0352(13)	2.0320(13)	2.0371(14)	2.04(18)
	$10^6 H_v$	0.00367(39)	0.00324(34)	0.00516(32)	1.32(28)
	$10^5 p_{Dv}$	-1.630(36)	-1.646(32)	-1.372(60)	5.9(21)
	$10^5 p_{Hv}$	…	…	-0.00258(23)	-1.317(63)
^{126}TeH $X\ ^2\Pi_{1/2}$	T_v	3828.50508(56)	5887.8542(20)		
	B_v	6.084056(23)	5.91879(24)		
	$10^4 D_v$	2.05307(98)	2.924(59)		
	p_v	-2.02136(12)	-1.9512(15)		
	$10^4 p_{Dv}$	2.2844(84)	3.3(12)		
	$10^6 p_{Hv}$	…	9.5(24)		

[a] All uncertainties are 1σ.

Table 4.9 Hund's case (c) constants (in cm^{-1}) for the $X\ ^2\Pi$ state of ^{125}TeH and ^{124}TeH.[a]

	Constants	v = 0	v = 1	v = 2	v = 3
^{125}TeH $X\ ^2\Pi_{3/2}$	T_v	0	2048.78958(21)	4022.52757(35)	5920.2880(15)
	B_v	6.048921(15)	5.884587(15)	5.719202(17)	5.55516(35)
	$10^4 D_v$	2.03576(99)	2.03154(98)	2.0338(12)	2.62(19)
	$10^9 H_v$	1.97(27)	1.77(23)	3.40(27)	223(30)
	$10^5 p_{Dv}$	-0.641(59)	-0.863(50)	-0.768(66)	7.0(15)
	$10^5 p_{Hv}$	…	0.000152(24)	-0.00219(21)	-1.333(46)
^{125}TeH $X\ ^2\Pi_{1/2}$	T_v	3828.50384(39)	5887.9156(17)		
	B_v	6.084543(15)	5.91924(20)		
	$10^4 D_v$	2.06031(59)	2.939(47)		
	p_v	-2.021443(84)	-1.9511(11)		
	$10^4 p_{Dv}$	2.1914(77)	3.36(93)		
	$10^6 p_{Hv}$	…	8.8(18)		
^{124}TeH $X\ ^2\Pi_{3/2}$	T_v	0	2048.85444(20)	4022.65142(31)	
	B_v	6.049342(15)	5.884973(15)	5.719558(16)	
	$10^4 D_v$	2.0385(11)	2.0332(11)	2.0339(12)	
	$10^9 H_v$	2.73(34)	2.28(29)	3.43(29)	
	$10^6 p_{Dv}$	-4.35(60)	-6.89(52)	-4.81(69)	
	$10^8 p_{Hv}$	…	0.170(35)	-2.83(23)	
^{124}TeH $X\ ^2\Pi_{1/2}$	T_v	3828.50445(39)	5887.9804(16)		
	B_v	6.084931(15)	5.91963(19)		
	$10^4 D_v$	2.05985(67)	2.940(45)		
	p_v	-2.021384(82)	-1.9511(11)		
	$10^4 p_{Dv}$	2.1659(78)	3.34(89)		
	$10^6 p_{Hv}$	…	8.8(17)		

[a] All uncertainties are 1σ.

Table 4.10 Hund's case (c) constants (in cm^{-1}) for the $X\ ^2\Pi$ state of ^{123}TeH and ^{122}TeH.[a]

	Constants	v = 0	v = 1	v = 2
^{123}TeH $X\ ^2\Pi_{3/2}$	T_v	0	2048.91695(32)	
	B_v	6.049740(18)	5.885448(22)	
	$10^4 D_v$	2.0395(14)	2.0461(21)	
	$10^9 H_v$	2.18(34)	6.32(66)	
^{123}TeH $X\ ^2\Pi_{1/2}$	T_v	3828.50416(30)	5888.0430(12)	
	B_v	6.085347(19)	5.92010(13)	
	$10^4 D_v$	2.0629(12)	2.950(31)	
	p_v	-2.02118(10)	-1.95105(75)	
	$10^4 p_{Dv}$	2.086(15)	3.27(63)	
	$10^6 p_{Hv}$	0.0126(52)	8.9(12)	
^{122}TeH $X\ ^2\Pi_{3/2}$	T_v	0	2048.98463(17)	4022.90202(27)
	B_v	6.050120(12)	5.885721(12)	5.720305(15)
	$10^4 D_v$	2.0379(11)	2.03230(93)	2.0382(13)
	$10^9 H_v$	2.33(30)	1.62(25)	4.57(39)
	$10^6 p_{Dv}$	…	0.90(48)	1.45(86)
	$10^8 p_{Hv}$	…	-0.63(26)	-3.62(46)
^{122}TeH $X\ ^2\Pi_{1/2}$	T_v	3828.50425(30)	5888.1106(12)	
	B_v	6.085722(12)	5.92038(14)	
	$10^4 D_v$	2.06068(52)	2.940(33)	
	p_v	-2.02119(10)	-1.95105(78)	
	$10^4 p_{Dv}$	2.086(16)	3.27(65)	
	$10^6 p_{Hv}$	0.0125(53)	8.8(13)	

[a] All uncertainties are 1σ.

Table 4.11 shows a comparison of parameters for ^{130}TeH determined in present study with those reported by Fink *et al.* from their Fourier transform study [7] and by Gillett *et al.* from their laser magnetic resonance work [9]. Because relatively few lines were observed for the 3 – 2 bands of the $X\ ^2\Pi_{3/2}$ spin component, B_3 was slightly deweighted when the constants B_0, B_1, B_2 and B_3 from the case (a) fit were used to determine the equilibrium constants of B_e, α_e and γ_e. In the previous work by Fink *et al.*, the tellurium isotopic splitting was resolved only for the few lines found for the 2 – 0 band of the $X\ ^2\Pi_{3/2}$ spin component. The laser magnetic resonance technique used in Gillett *et al.*'s experiment limited their data to low J lines only. In contrast to the previous works, the present work observed many more lines for which the tellurium isotopic splitting was resolved: the 1 – 0 , 2 – 1 and 3 – 2 bands of the $X\ ^2\Pi_{3/2}$ spin component with J values up to 29.5. The new constants are determined from a much larger range of data, and the present Hund's case (a) fits reliably describe all the lines, including those which suffer from perturbations.

Table 4.11 A comparison of the present and previously determined parameters in Hund's case (a) fits for ^{130}TeH in the $X\ ^2\Pi$ state.

	Fink *et al.*[a]	Gillett *et al.*[b]	Present work
T_{2-0}	4032.6159(7)	4032.625(25)	4032.35331(45)
ω_e	…	2128.214(13)	2129.1666(12)[d]
$\omega_e x_e$	…	37.0358(25)	37.66332(42)[d]
B_0	6.06512(6)	6.065064(37)	6.065439(26)
B_e	6.14776(9)	6.147229(53)	6.14152(48)[c]
α_e	0.16528(6)	0.164330(31)	0.15671(75) [c]
γ_e	…	…	-0.00246(24) [c]
$10^3 D_0$	0.2037(7)	0.2086(11)	0.18881(11)
$10^7 H_0$	0.064(56)	0.165(74)	-0.0995(35)
A_0	-3816.3693(1)	-3815.4832(58)	-3816.38124(42)
A_{D0}	-0.017234(4)	-0.014326(21)	-0.0176111(89)
$(p + 2q)_0$	2.0213(5)	2.021435(92)	2.037158(17)
$10^2 q_0$	-0.28(2)	-0.311(24)	-0.3924(39)
r_0 (Å)	1.667110(9)	1.6671173(61)	1.6670657(36)
r_e (Å)	1.65587(1)	1.6559383(81)	1.6567077(65)

[a] Ref. [7].
[b] Ref. [9].
[c] Obtained by fitting the constants B_0, B_1, B_2 and B_3 from the Hund's case (a) fit for ^{130}TeH.
[d] Obtained by exact fits from the corresponding constants; their uncertainties were obtained by propagation of errors.

4.4 Conclusions

The vibration-rotation emission spectra for the $X\,^2\Pi$ ground state and for the near infrared emission spectra of the $X\,^2\Pi_{1/2} - X\,^2\Pi_{3/2}$ system of the TeH and TeD free radicals have been measured at high resolution using a Fourier transform spectrometer. TeH and TeD were generated in a tube furnace with a D.C. discharge of a flowing mixture of argon, hydrogen (or deuterium) and tellurium vapor. In the infrared region for the $X\,^2\Pi_{3/2}$ spin component, the 1 – 0, 2 – 1 and 3 – 2 vibrational bands were observed for most of the eight isotopologues of TeH and the 1 – 0 and 2 – 1 bands for three isotopologues of TeD. For the $X\,^2\Pi_{1/2} - X\,^2\Pi_{3/2}$ transition, the 0 – 0 and 1 – 1 bands were observed for TeH and the 0 – 0, 1 – 1 and 2 – 2 bands for TeD. Except for a few lines, the tellurium isotopic shift was not resolved for the $X\,^2\Pi_{1/2} - X\,^2\Pi_{3/2}$ transitions of TeH and TeD. Local perturbations with $\Delta v = 2$ were found between the two spin components of the $X\,^2\Pi$ state of TeH: $X\,^2\Pi_{1/2}$, v = 0 with $X\,^2\Pi_{3/2}$, v = 2; $X\,^2\Pi_{1/2}$, v = 1 with $X\,^2\Pi_{3/2}$, v = 3. The new data were combined with the previous data from the literature, and two kinds of fits (Hund's case (a) and Hund's case (c)) were carried out for each of the ten observed isotopologues: ^{130}TeD, ^{128}TeD, ^{126}TeD, ^{130}TeH, ^{128}TeH, ^{126}TeH, ^{125}TeH, ^{124}TeH, ^{123}TeH and ^{122}TeH. The spectroscopic constants for the ground $X\,^2\Pi$ state of both TeH and TeD have been extended and improved.

4.5 References

[1] H. E. Radford, J. Chem. Phys. 40 (1964) 2732 – 2733.

[2] R.J. Donovan, D.J. Little and J. Konstantatos, J. Chem. Soc. Faraday Trans. 2. **68**, 1812 (1972).

[3] D. J. Little, R. J. Donovan and R. J. Butcher, J. Photochem. 2 (1973) 451 – 457.

[4] T. Balkis, A. F. Gaines, G. Özegen, I. T. Özegen and M. C. Flowers, J. Chem. Soc. Faraday Trans. 2. **72**, 524 (1975).

[5] J.-F. Gal, P.-C. Maria and M. Decouzon, Int. J. Mass Spectrosc. Ion Processes, **93**, 87 (1989).

[6] C.B. Friedhoff, J.T. Snodgrass, J.V. Coe, K.M. McHugh, and K.H. Bowen, J. Chem. Phys. **84** 1051 (1986).

[7] E.H. Fink, and K.D. Setzer, D.A. Ramsay and M. Vervloet, J. Mol. Spectrosc. **138,** 19 (1989).

[8] J.P. Towle and J.M. Brown, Mol. Phys. **74**, 465 (1991).

[9] D.A. Gillett, J.P. Towle, M. Islam and J.M. Brown, J. Mol. Spectrosc. **163**, 459 (1994).

[10] K. Balasubramanian, M. Han and M.Z. Liao, J. Chem. Phys. **86**, 4979 (1987).

[11] T.K. Balasubramanian and O. Narayanan, J. Mol. Spectrosc. **155**, 221 (1992).

[12] L. Pisani and E. Clementi, J. Chem. Phys. **103,** 9321 (1995).

[13] K.D. Setzer, E.H. Fink, A.B. Alekseyev, H.-P. Liebermann and R.J. Buenker, J. Mol. Spectrosc. **206**, 181 (2001).

[14] S. Yu, A. Shayesteh, D. Fu and P. Bernath, J. Mol. Spectrosc. **230**, 105 (2005).

[15] R.B. LeBlanc, J.B. White and P.F. Bernath, J. Mol. Spectrosc. **164**, 574 (1994).

[16] I. Mills, T. Cvitas, K. Homann, N. Kallay and K. Kuchitsu, *Quantities, units and symbols in physical chemistry*, Blackwell Scientific, Oxford, 1988.

[17] C. Amiot, J.-P. Maillard and J. Chauville, J. Mol. Spectrosc. **87**, 196 (1981).

[18] S.H. Ashworth and J.M. Brown, J. Chem. Soc. Faraday Trans. **86,** 1995 (1990).

[19] R.S. Ram and P.F. Bernath, J. Mol. Spectrosc. **203**, 9 (2000).

[20] J. M. Brown and A. Carrington, *Rotational Spectroscopy of Diatomic Molecules*, Cambridge University Press, Cambridge (2003).

[21] R.J. Le Roy, *RKR1 2.0, A Computer Program Implementing the First-Order RKR Method for Determining Diatomic Molecule Potential Energy Function,* University Of Waterloo, Chemical Physics Research Report CP-657(2003), *http://leroy.uwaterloo.ca/programs.*

[22] R.J. Le Roy, *LEVEL 7.5, A Computer program for Solving the Radial Schrödinger Equation for Bound and Quasibound Levels,* University of Waterloo, Chemical Physics Research Report CP-655(2002), *http://leroy.uwaterloo.ca/programs.*

Chapter 5

Fourier transform infrared emission spectroscopy of HZnCl

5.1 Introduction

In the past twenty years, matrix-isolation techniques have been applied in the investigation of the reactions between HCl and metal atoms. The group 1 metal atoms K and Na react with HCl to give the ion pair M^+HCl^-, while Li reacts to give a metal atom adduct Li:HCl [1–3]. Fe and Hg can insert into the H–Cl bond to form the linear metal hydrochloride HMCl and Al inserts into the H–Cl bond to form the bent HAlCl molecule [4–6]. Recently, the reactions between HCl and the group 12 metal atoms, Zn, Cd and Hg were studied in solid argon matrices [7]. Zn and Cd can also insert into the H–Cl bond to form the linear metal hydrochloride HMCl. Macrae *et al*. [7] reported a value of 1952.3 cm^{-1} for the H–Zn stretching mode (ν_1), 449.6 cm^{-1} for the bending mode (ν_2) and ~ 420 cm^{-1} for the Zn–Cl stretching mode (ν_3), with assignments validated by the effects of isotopic substitution and by the results of density functional calculations.

The properties of HMCl (M = Zn, Cd and Hg) have been compared with those of the corresponding metal dihydrides [7]. HCl has a dissociation energy close to that of H_2, and the polar metal–chlorine bonds have higher dissociation energies than the corresponding metal–hydrogen bonds. The ground state reaction $M(^1S) + HCl(g) \rightarrow HMCl(g)$ was predicted to be exoergic by 30 kcal/mol, 17 kcal/mol and 1 kcal/mol for M = Zn, Cd and Hg, respectively [7]. The corresponding reactions with H_2 are consistently endoergic [8]. Therefore HCl offers a more energetically favorable opportunity for metal insertion than does H_2. ZnH_2, CdH_2 and HgH_2 have recently been observed in the gas phase [9–11]. Surprisingly, no gaseous metal hydrochloride has ever been observed.

In this chapter, the first observation of gaseous zinc hydrochloride is reported. The high resolution vibration-rotation emission spectrum of HZnCl was recorded using a Fourier transform spectrometer, and the H–Zn stretching mode (ν_1) has been detected near 1966 cm^{-1}. The spectra were analyzed with the guidance of DFT calculations performed by A. Shayesteh [12], and spectroscopic constants were obtained for four isotopologues of HZnCl: $H^{64}Zn^{35}Cl$, $H^{66}Zn^{35}Cl$, $H^{68}Zn^{35}Cl$ and $H^{64}Zn^{37}Cl$. The results presented in this chapter have been published in Ref. [12]. After this HZnCl paper was published, Kerkines *et al.* [13] investigated the geometric and energetic parameters of HZnCl using high level *ab initio* calculations (CCSD(T)). The theoretical H–ZnCl and HZn–Cl bond lengths were calculated to be 1.499 and 2.079 Å, respectively.

5.2 Experimental details

The HZnCl molecule was generated with the high temperature tube furnace with an electrical discharge, which has been described in Section 2.1.1. A Zn rod was placed inside an alumina tube (5 cm × 120 cm) and heated to 470°C to produce about one Torr of Zn vapor. About 0.6 Torr of pure HCl gas flowed slowly through the tube, and a D.C. discharge was used at a current of about 250 mA. The resulting radiation was focused by a BaF_2 lens into the entrance aperture of a Bruker IFS 120 HR Fourier transform spectrometer. Eleven hundred scans were recorded at a resolution of 0.01 cm^{-1} with

a KBr beamsplitter using a liquid nitrogen-cooled InSb detector. The recording time was about 19 hours. The spectral region was limited to 1800 – 2200 cm^{-1} by the detector response and a 2200 cm^{-1} long-wave pass filter.

5.3 Results and discussion

Figure 5.1 shows an overview of the spectrum of the ν_1 mode of HZnCl and Figure 5.2 is an expanded view. The spectrum contained lines from ZnH_2 [9] and strong emission lines from impurity CO, which were used for calibration. The accuracy of measured wavenumbers is approximately 0.001 cm^{-1} for lines from the fundamental band of the most abundant isotopologue $H^{64}Zn^{35}Cl$, and 0.002 cm^{-1} for the other bands. The band origin of the strongest band in the spectrum is 1966.87 cm^{-1}, which matches the matrix-isolation value of 1952.3 cm^{-1} if the matrix shift is taken into account [7]. The line spacing is about 0.3 cm^{-1}, which is close to the calculated value of 2*B* for the HZnCl molecule. Five series of lines were found with the help of a Loomis-Wood program [14].

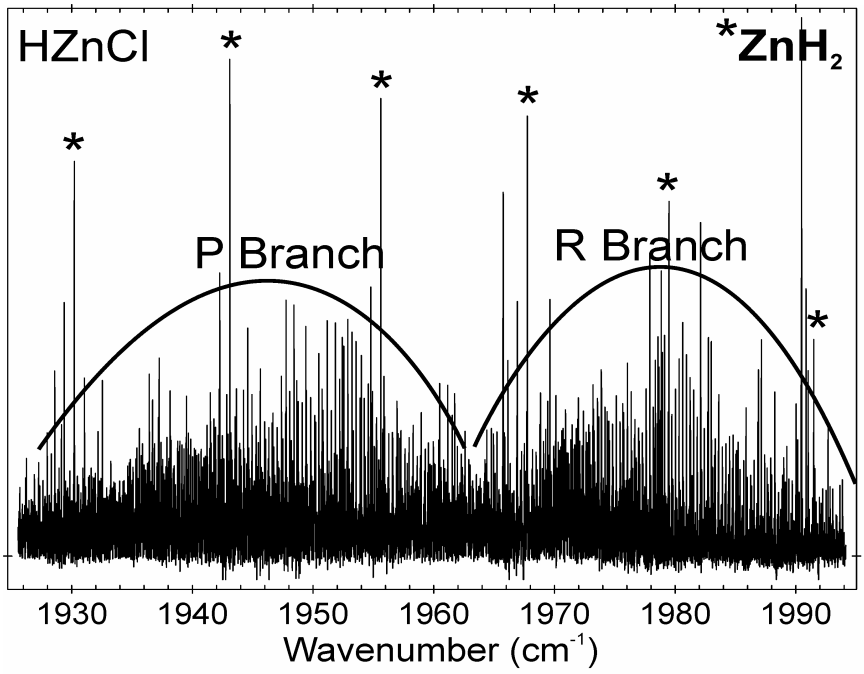

Figure 5.1 An overview of the vibration-rotation emission spectrum of HZnCl recorded at a resolution of 0.01 cm^{-1}. This spectrum was the result of 1100 coadditions and the recording time was about 19 hours. The baseline was corrected with the Bruker OPUS software and the strong lines are due to atomic zinc or the ZnH_2 molecule.

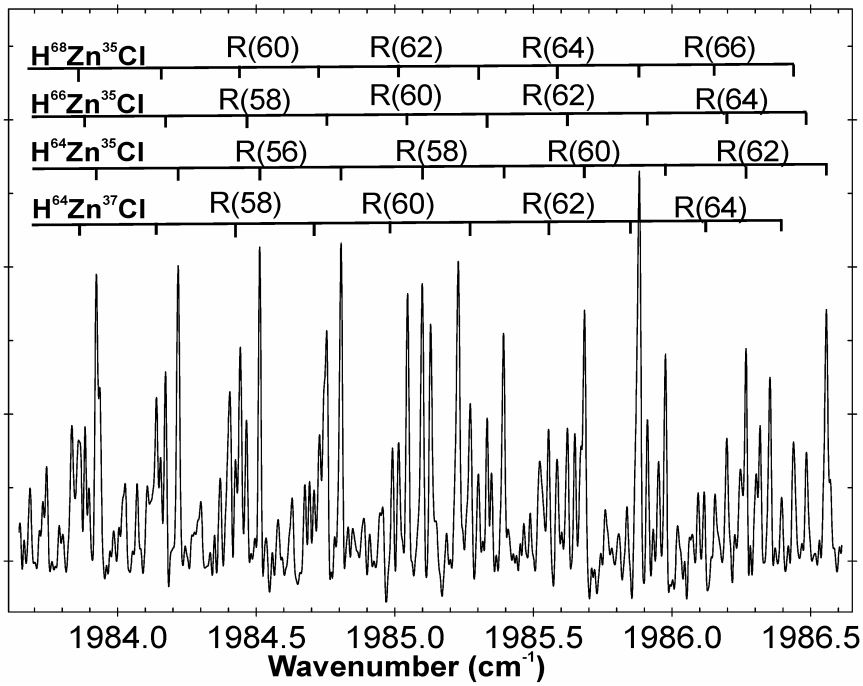

Figure 5.2 An expanded view of the *R* branch of the fundamental band of the ν_1 (H – Zn stretching) mode of HZnCl near 1984 cm^{-1}. The assignments were based on the relative intensities, band origin ratios and *B* value ratios of these four isotopologues of HZnCl.

The natural zinc isotope abundances are ^{64}Zn: 48.6%, ^{66}Zn: 27.9%, ^{67}Zn: 4.1%, ^{68}Zn: 18.8%, ^{70}Zn: 0.6%, and the natural chlorine abundances are ^{35}Cl: 75.77%, ^{37}Cl: 24.23% [15]. Four of the five bands were assigned to the fundamental bands of the H–Zn stretching mode (ν_1) of H^{64}Zn^{35}Cl, H^{66}Zn^{35}Cl, H^{68}Zn^{35}Cl and H^{64}Zn^{37}Cl according to their relative intensities and *B* values, and one band was assigned to the $2\nu_1 - \nu_1$ (200 – 100) hot band of H^{64}Zn^{35}Cl.

The spectrum is very dense, and the lines near the band origin overlap severely. It was not possible to assign the first *P* and *R* branch lines for the bands by looking at the spectrum, or even with the help of the Loomis-Wood program. A least-squares fit was performed separately for each of the five observed bands, and the lines were fitted using the simple energy level expression (Section 1.4):

$$E = G(\nu_1, \nu_2, \nu_3) + B_\nu J(J+1) - D_\nu [J(J+1)]^2, \qquad (5.1)$$

where $G(\nu_1, \nu_2, \nu_3)$ is the vibrational energy of the (ν_1, ν_2, ν_3) state relative to the zero point energy (ZPE), $G(0, 0, 0)$. It turned out that the *J* assignments for each band could be shifted and still the same standard deviations were obtained for the fits (i.e., if *J* was changed by +1, +2, etc., in the *P* branch and –1, –2, etc. in the *R* branch, then the standard deviation of the fit was unchanged).

The absolute *J* assignment of the main isotopologue H^{64}Zn^{35}Cl was finally obtained by fitting the fundamental band and the $2\nu_1 - \nu_1$ hot band together. Combination differences were used to

determine the relative *J* assignment of the 100 – 000 fundamental band and the 200 – 100 band of $H^{64}Zn^{35}Cl$. Although the standard deviations for the separate fits of these two bands did not change with the shifts of the *J* assignment, the standard deviation did change when these two bands were fitted together, and a minimum of 0.79 was found for the reduced standard deviation. The standard deviation increased by about 5% when the *J* assignment was changed by –1 in the *P* branch and +1 in the *R* branch, or by +1 in the P branch and –1 in the *R* branch. The standard deviation of the fits increased steadily for larger shifts in the *J* assignment. Although the minimum in the standard deviation is not very sharp, the assignments for the $H^{64}Zn^{35}Cl$ bands are believed to be correct.

To obtain the corresponding absolute *J* assignments for the other three isotopologues, some additional information was needed, such as the isotopic shifts for the band origins or for the *B* values. The *J* assignments for the three minor isotopologues were shifted and the observed band origin ratios and *B* value ratios were compared with the *ab initio* values calculated at the DFT(B3LYP) level [12]. The observed band origin ratios and *B* value ratios are very sensitive to the shifts in the *J* assignments, and the assignments of the three minor isotopologues relative to the main isotopologue $H^{64}Zn^{35}Cl$ were determined in this way. Table 5.1 gives the spectroscopic constants obtained for $H^{64}Zn^{35}Cl$, $H^{66}Zn^{35}Cl$, $H^{68}Zn^{35}Cl$ and $H^{64}Zn^{37}Cl$ from the least-squares fits. The agreement between the observed and calculated band origin shifts and ΔB value of the four isotopologues is quite good; this comparison is given in Table 5.2. The output files of the fits, including complete line lists, have been published in the supplementary tables of Ref. [12].

Table 5.1 Spectroscopic constants (in cm^{-1}) for the ν_1 (H – Zn stretching) mode of HZnCl.[a]

	Level	G_v – ZPE	$B_{v_1 v_2 v_3}$	$D_{v_1 v_2 v_3} / 10^{-8}$
$H^{64}Zn^{35}Cl$	000	0.0	0.16203125(96)	8.8287(61)
	100	1966.86928(12)	0.16179977(96)	8.8061(62)
	200	3923.72224(28)	0.16157547(98)	8.7827(65)
$H^{66}Zn^{35}Cl$	000	0.0	0.1605027(21)	8.685(13)
	100	1966.39405(20)	0.1602766(21)	8.660(13)
$H^{68}Zn^{35}Cl$	000	0.0	0.1590536(29)	8.523(24)
	100	1965.94646(26)	0.1588326(29)	8.497(24)
$H^{64}Zn^{37}Cl$	000	0.0	0.1564897(33)	8.272(32)
	100	1966.80602(26)	0.1562691(32)	8.251(30)

[a] All uncertainties are 1σ.

Table 5.2 A comparison of the observed and calculated band origin shifts and ΔB values (in cm^{-1}) for different isotopologues of HZnCl.

Molecule	$\Delta\nu_{1,\,obs.}$	$\Delta\omega_{1,\,calc.}$ [a]	$\Delta B_{000,\,obs.}$	$\Delta B_{e,\,calc.}$ [b]
$H^{64}Zn^{35}Cl$	0	0	0	0
$H^{66}Zn^{35}Cl$	–0.47523	–0.4819	–0.0015286	–0.001554
$H^{68}Zn^{35}Cl$	–0.92282	–0.9356	–0.0029777	–0.003022
$H^{64}Zn^{37}Cl$	–0.06326	–0.0007	–0.0055416	–0.005571

[a] ω_1 calculated at the DFT (B3LYP)/6-311++G(3df, 3pd) level [12] and $\Delta\omega_1$ are scaled by $\nu_{1,\,obs.}/\omega_{1,\,calc.}$ of $H^{64}Zn^{35}Cl$.
[b] B_e calculated at the DFT (B3LYP)/6-311++G(3df, 3pd) level [12] and ΔB_e are scaled by $B_{000,\,obs.}/B_{e,calc.}$ of $H^{64}Zn^{35}Cl$.

The four observed B_0 values of the four isotopologues were used to calculate the r_0 bond lengths for the v = 0 level of HZnCl. There were six pairwise combinations to calculate the $r_{H–Zn}$ and $r_{Zn–Cl}$ bond lengths by use of the moment of inertia equation [Eqs. (1.29) and (1.30)]. The $r_{H–Zn}$ values obtained from different combinations are quite different, and range from 1.596 Å to 1.789 Å. The $r_{Zn–Cl}$ values obtained are more consistent, and range from 2.079 Å to 2.088 Å. These results, especially the $r_{H–Zn}$ bond distances, were not very satisfactory.

The r_s bond length for the Zn–Cl bond was calculated for HZnCl by using Kraitchman's procedure for single isotopic substitutions [30]. The formula used for HZnCl is:

$$|z| = \left[\frac{1}{\mu}\left(I' - I\right)\right]^{1/2}, \tag{5.2}$$

where $|z|$ is the distance of the substituted atom from the center of mass of HZnCl; I is the moment of inertia of the parent molecule, $H^{64}Zn^{35}Cl$; I' is the moment of inertia of the isotopically substituted molecule, $H^{66}Zn^{35}Cl$, $H^{68}Zn^{35}Cl$ or $H^{64}Zn^{37}Cl$; μ is called the reduced mass for the isotopic substitution and defined as:

$$\mu = \frac{M\Delta m}{M + \Delta m}, \tag{5.3}$$

where M is the total mass of the parent molecule, $H^{64}Zn^{35}Cl$, and Δm is the mass difference between the isotopically substituted molecule and the parent molecule, $H^{64}Zn^{35}Cl$. A value of 1.37175 Å was obtained for the distance of ^{35}Cl from the center of the mass of $H^{64}Zn^{35}Cl$ by using the observed B_0 values of $H^{64}Zn^{35}Cl$ and $H^{64}Zn^{37}Cl$. An average value of 0.71171 Å was obtained for the distance of ^{64}Zn from the center of the mass of $H^{64}Zn^{35}Cl$ by using the observed B_0 values for the $H^{64}Zn^{35}Cl/H^{66}Zn^{35}Cl$ and $H^{64}Zn^{35}Cl/H^{68}Zn^{35}Cl$ pairs. Therefore, the $r_{Zn–Cl}$ bond length is equal to 2.08346 Å, which agrees well with the *ab initio* calculations (2.079 Å at the CCSD(T) level [13] and 2.08 Å at the DFT(B3LYP) level [12]) and with the r_0 values obtained from the moment of inertia equation (2.079 Å to 2.088 Å). Because DZnCl was not observed, it was not possible to calculate the $r_{H–Zn}$ bond length using Kraitchman's equation. The $r_{H\text{-}Zn}$ bond length was derived by substituting $r_{Zn–}$

$_{Cl}$ = 2.08346 Å for $H^{64}Zn^{35}Cl$ into the moment of inertia equation [Eq.(1.29)] and into the center of mass equation. The obtained values are 1.70480 Å and 1.75796 Å, respectively. These two values are quite different from the *ab initio* values (1.499 Å at the CCSD(T) level [13] and 1.52 Å at the DFT(B3LYP) level [12]). Furthermore, when the $r_{H–Zn}$ bond length was fixed at the theoretically calculated value of 1.52 Å, a value of 2.09218 Å was obtained for the $r_{Zn–Cl}$ bond length using the moment of inertia equation, which is rather close to the r_s value. The present experimental data are therefore not sufficient to provide information on the $r_{H–Zn}$ bond length for HZnCl. The spectra of DZnCl need to be measured to obtain an accurate $r_{H–Zn}$ bond length. At this moment, the best bond lengths are the partial r_s value of 2.08346 Å for the Zn–Cl bond length and the *ab initio* value of 1.499 Å from Ref. [13] for the H–Zn bond length.

5.4 Conclusions

Gaseous HZnCl has been synthesized for the first time in a high-temperature tube furnace with a D.C. discharge in a flowing mixture of pure HCl and Zn vapor. The vibration-rotation emission spectrum of HZnCl was recorded at high resolution using a Fourier transform spectrometer. The H–Zn stretching mode (ν_1) of the $H^{64}Zn^{35}Cl$, $H^{66}Zn^{35}Cl$, $H^{68}Zn^{35}Cl$, and $H^{64}Zn^{37}Cl$ species, as well as the $2\nu_1 – \nu_1$ hot band of the most abundant isotopologue $H^{64}Zn^{35}Cl$, were observed near 1966 cm^{-1}. The absolute J assignment of the most abundant isotopologue $H^{64}Zn^{35}Cl$ was obtained by fitting the fundamental band and the 200 – 100 hot band together. The relative assignment of the four isotopologues was established by using band origin ratios and B value ratios obtained from *ab initio* calculations. A least-squares fit was performed for each of four observed isotopologues and their spectroscopic constants were determined. J assignments are still not completely certain, and measurements of microwave spectra of HZnCl are desirable to determine these values.

5.5 References

[1] D.M. Lindsay, M.C.R. Symons, D.R. Herschbach, A.L. Kwiram, *J. Phys. Chem.* **86,** 3789 (1982).

[2] M.A. Davis, D.M. Lindsay, *Surf. Sci.* **156,**335 (1985).

[3] P.H. Kasai, *J. Phys. Chem. A* **104**, 4514 (2000).

[4] S.F. Parker, C.H.F. Peden, C.H.F. Barrett, R.G. Pearson, *J. Am. Chem. Soc.* **106**, 1304 (1984).

[5] R.Köppe, P.H. Kasai, *J. Am. Chem. Soc.* **118**, 135 (1996).

[6] N. Legay-Sommaire, F. Legay, *Chem. Phys. Lett.* **3**, 40**14** (1999).

[7] V.A. Macrae, J.C. Green, T.M. Green, A.J. Downs, *J. Phys. Chem.* **108**, 9500 (2004).

[8] T.M. Greene, W. Brown, L. Andrews, A.J. Downs, G.V. Chertihin, N. Runeberg, P. Pyykkö, *J. Phys. Chem.* **99**, 7925 (1995).

[9] A. Shayesteh, D.R.T. Appadoo, I. Gordon and P. Bernath, *J. Am. Chem. Soc.* **126**, 14356 (2004).

[10] A. Shayesteh, S. Yu, P. F. Bernath, *Chem. Eur. J.* **11**, 4709 (2005).

[11] S. Yu, A. Shayesteh, P. F. Bernath, *J. Chem. Phys.* **122**, 194301 (2005).

[12] S. Yu, A. Shayesteh, D. Fu, P. Bernath, *J. Phys. Chem.A* **109,** 4092 (2005).

[13] I.S.K. Kerkines, A. Mavridis and P.A. Karipidis, *J. Phys. Chem. A* **110**, 10899 (2006).

[14] F.W. Loomis and R.W. Wood, Phys. Rev. **32** 223 (1928).

[15] I. Mills, T. Cvitas, K. Homann, N. Kallay, K. Kuchitsu, *Quantities, units and symbols in physical chemistry*, 2nd ed., Blackwell Scientific, Oxford, 1993.

[16] W. Gordy, R.L Cook, *Microwave Molecular Spectra*, Interscience Publishers, New York, 1970.

Chapter 6

Fourier transform infrared emission spectroscopy of CdH_2 and CdD_2

6.1 Introduction

Many metal dihydrides have been identified at low temperatures by matrix isolation spectroscopy [1], but only FeH_2, BeH_2, MgH_2, ZnH_2 and HgH_2 have been observed in the gas phase [2–6]. This chapter reports the first observation of gaseous CdH_2 and CdD_2 and the complete analysis of their vibration-rotation emission spectra.

Barbaras *et al*. [7] synthesized solid CdH_2 in 1951 from the reaction of dimethylcadmium with lithium aluminum hydride in diethyl ether solution, and it was noticed that solid CdH_2 is unstable and rapidly decomposes into Cd atoms and molecular hydrogen above –20°C. It was reported recently that the reduction of aqueous Cd(II) with sodium tetrahydroborate ($NaBH_4$) leads to formation of both atomic and molecular cadmium species [8–10]. The molecule formed in the reduction reaction could be CdH_2, but this has not been confirmed yet. The interaction of Cd atoms in ^1P or ^3P excited states with H_2 or D_2 in the gas phase was investigated experimentally [11,12] and theoretically [12–15] , and it was speculated that bent CdH_2 and CdD_2 molecules in excited electronic states are reaction intermediates in the formation of CdH, CdD or linear CdH_2 and CdD_2.

The only spectroscopic studies on cadmium dihydride are measurements of the infrared spectra of CdH_2, CdHD and CdD_2 in argon, neon and hydrogen matrices [16,17]. Recently, CdH_2 was also observed as a byproduct in a few matrix-isolation experiments studying the reactions of Cd with SiH_4, HCl and H_2O in a solid argon matrix [18–20]. The equilibrium geometry of CdH_2 has been the subject of several theoretical investigations [1,14,16,21–23], and values ranging from 1.67 Å to 1.74 Å have been obtained for the Cd–H bond distance. A high level *ab initio* calculation (CCSD(T)) [16] showed that the overall reaction to form gaseous CdH_2 from ground state Cd and H_2 is endoergic by 17.0 kcal/mol.

In this present study, the fundamental bands were obtained for the antisymmetric stretching mode (ν_3) of CdH_2 and CdD_2 and the $002(\Sigma_g^+) - 001(\Sigma_u^+)$ and $011(\Pi_g) - 010(\Pi_u)$ hot bands for CdH_2. Lines from different isotopologues of CdH_2 and CdD_2 were fitted separately, and spectroscopic constants were determined for each of the twelve observed isotopologues: $^{110}CdH_2$, $^{111}CdH_2$, $^{112}CdH_2$, $^{113}CdH_2$, $^{114}CdH_2$, $^{116}CdH_2$, $^{110}CdD_2$, $^{111}CdD_2$, $^{112}CdD_2$, $^{113}CdD_2$, $^{114}CdD_2$, $^{116}CdD_2$. The obtained B_{000} values were used to calculate the average Cd–H and Cd–D r_0 bond distances and the average r_s structure. The results presented in this chapter have been published in Ref. [24].

6.2 Experimental details

CdH_2 and CdD_2 molecules were generated in an emission source with an electrical discharge inside a high temperature furnace, which has been described in Section 2.1.1. A tantalum boat containing

cadmium granules was placed inside an alumina tube (5 cm × 120 cm) and heated to 350°C. About 0.8 Torr of hydrogen or deuterium gas flowed slowly through the tube, and a D.C. discharge was used at a current of about 220 mA. The resulting radiation was focused by a BaF_2 lens into the entrance aperture of a Bruker IFS 120 HR Fourier transform spectrometer.

The infrared emission spectrum of CdH_2 was measured at a resolution of 0.01 cm^{-1} in the 1200 – 2200 cm^{-1} region with a KBr beamsplitter and a liquid nitrogen-cooled HgCdTe (MCT) detector, and the recording time was about five hours (about 300 scans). The spectrum also contained strong emission lines from impurity CO, which was used for calibration. The accuracy of measured wavenumbers is approximately 0.001 cm^{-1} for the CdH_2 lines.

The spectrum of CdD_2 was measured at a resolution of 0.01 cm^{-1} in the 800 – 1600 cm^{-1} region with the same beamsplitter and detector, and the recording time was about nine hours (about 500 scans). The calibration of this spectrum was based on thirteen lines that were common with the CdH_2 spectrum. The accuracy of the measured CdD_2 lines is of the same order, 0.001 cm^{-1}, as the CdH_2 lines.

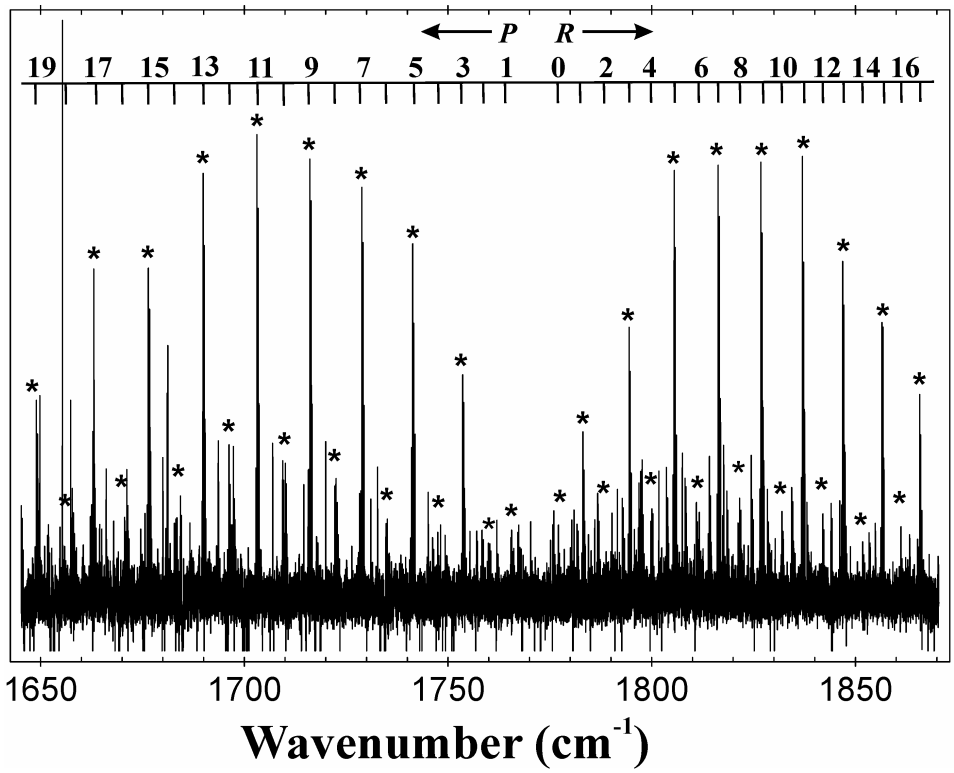

Figure 6.1 An overview of the infrared emission spectrum of CdH_2 recorded at a resolution of 0.01 cm^{-1}. The baseline was corrected with the Bruker OPUS software and the absorption lines are due to atmospheric H_2O vapor. The marked lines with a 3:1 intensity alternation are from the 001 – 000 band, and the unmarked lines are from the 002 – 001 and 011 – 010 hot bands.

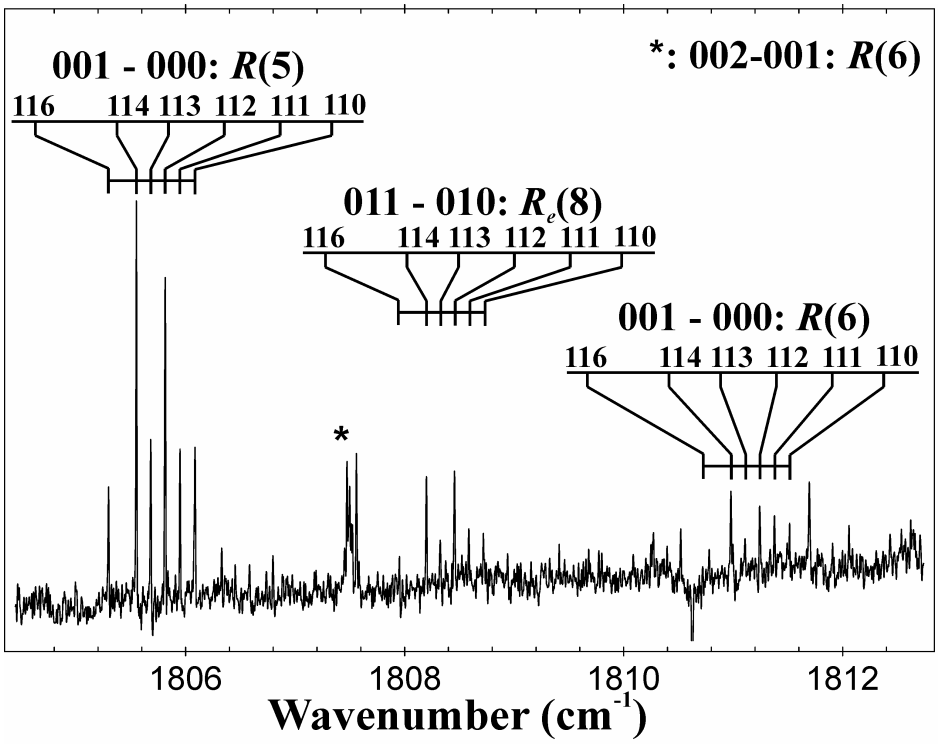

Figure 6.2 An expanded view of the infrared spectrum of CdH_2 near 1808 cm^{-1}. Six out of the eight isotopologues of CdH_2 were observed, and the numbers on the top of the lines are the mass numbers of the cadmium atom. The interaction between the 002 and the 200 vibrational levels makes the isotopic splitting of lines from the 002 – 001 band very small (see the text).

6.3 Results and discussion

Figure 6.1 shows the overview spectrum of CdH_2, which confirmed the predicted linear structure of CdH_2 [16]. The adjacent rotational lines have alternating 3:1 intensity ratio, due to the *ortho-para* nuclear spin statistical weights, $(I+1)/I$, with I = ½ for hydrogen [25]. Cadmium has eight naturally-occurring isotopes, ^{106}Cd (1.25%), ^{108}Cd (0.89%), ^{110}Cd (12.49%), ^{111}Cd (12.80%), ^{112}Cd, (24.13%), ^{113}Cd (12.22%), ^{114}Cd, (28.73%), and ^{116}Cd (7.49%) [26]. The observed series were assigned to $001(\Sigma_u^+) - 000(\Sigma_g^+)$, $002(\Sigma_g^+) - 001(\Sigma_u^+)$ and $011(\Pi_g) - 010(\Pi_u)$ bands for six of the eight possible isotopologues of CdH_2. Figure 6.2 shows an expanded view of the CdH_2 spectrum. Lines from the $002(\Sigma_g^+) - 001(\Sigma_u^+)$ hot band have smaller isotopic shifts as compared to lines of the $001(\Sigma_u^+) -$

$000(\Sigma_g^+)$ and $011(\Pi_g) - 010(\Pi_u)$ bands because of the interaction of the $002(\Sigma_g^+)$ state with the nearby $200(\Sigma_g^+)$ state (see below). The CdD_2 spectrum was much weaker than the CdH_2 spectrum, and only the $001(\Sigma_u^+) - 000(\Sigma_g^+)$ fundamental band was observed for six out of eight isotopologues of CdD_2.

The rotational assignment of the $001(\Sigma_u^+) - 000(\Sigma_g^+)$ fundamental band of CdH_2 was easily made because the first lines for both the *P* and *R* branches were observed. The assignments were confirmed by small perturbations at $J' = 12$ to 17, which are due to the interaction between the $001(\Sigma_u^+)$ and $030(\Pi_u$ or $\Phi_u)$ levels. The ν_3 and ν_2 fundamental bands were observed in an argon matrix at 1753.8 cm^{-1} and 601.7 cm^{-1}, and were calculated to be 1790 cm^{-1} and 574 cm^{-1} using the CCSD(T) method [16], respectively. Three times the matrix value for ν_2 is 1805 cm^{-1}, which is close to the ν_3 value of 1772 cm^{-1} observed in the present experiment. Combination differences were used to determine the absolute *J* assignment of the $002(\Sigma_g^+) - 001(\Sigma_u^+)$ hot band of CdH_2. For the $011(\Pi_g) - 010(\Pi_u)$ hot band, the assignment was based on perturbations at $J' = 9$ to 13 of the *e* component, which is caused by the interaction between the $011(\Pi_g)$ and $040(\Sigma_g^+, \Delta_g$ or $\Gamma_g)$ levels, and was confirmed by fitting together the *P* and *R* branches of both the *e* and *f* components of the $011(\Pi_g) - 010(\Pi_u)$ transition.

No perturbations were observed in the CdD_2 spectrum. The rotational assignment of the $001(\Sigma_u^+) - 000(\Sigma_g^+)$ fundamental band of CdD_2 was based on the mass relationship between the B_{000}'s of CdH_2 and CdD_2.

Lines from different isotopologues were fitted separately. The customary energy level expression for linear triatomic molecules:

$$E(J) = G(\nu_1, \nu_2, \nu_3) + BJ(J+1) - D[J(J+1)]^2 \qquad (6.1)$$

was used for the vibration-rotation levels of the $000(\Sigma_g^+)$ and $001(\Sigma_u^+)$ states of CdD_2. In Eq. (6.1), $G(\nu_1, \nu_2, \nu_3)$ is the vibrational energy of the (ν_1, ν_2, ν_3) state relative to the zero point energy (ZPE), $G(0, 0, 0)$. The constants obtained for CdD_2 are provided in Table 6.1. The observed line positions and the output files of the least-squares fits have been published in the supplementary tables of Ref. [24].

Table 6.1 Spectroscopic constants (in cm^{-1}) for CdD_2 (all uncertainties are 1σ).

	Level	*G*v -ZPE	$B_{v_1v_2v_3}$	$D_{v_1v_2v_3}/10^{-6}$
$^{110}CdD_2$	000	0.0	1.484200(17)	7.917(20)
	001	1279.08237(58)	1.472267(15)	7.944(19)
$^{111}CdD_2$	000	0.0	1.484197(18)	7.910(23)
	001	1278.88476(51)	1.472264(19)	7.920(26)
$^{112}CdD_2$	000	0.0	1.4842403(98)	7.973(11)
	001	1278.69003(29)	1.472317(10)	7.992(12)
$^{113}CdD_2$	000	0.0	1.484246(14)	7.974(24)
	001	1278.49847(39)	1.472329(13)	7.990(21)
$^{114}CdD_2$	000	0.0	1.4842084(96)	7.935(10)
	001	1278.31167(28)	1.4722946(98)	7.955(11)
$^{116}CdD_2$	000	0.0	1.484243(18)	7.988(19)
	001	1277.94301(66)	1.472355(19)	8.029(19)

The $001(\Sigma_u^+)$ – $000(\Sigma_g^+)$ fundamental band and the two hot bands, $002(\Sigma_g^+)$ – $001(\Sigma_u^+)$ and $011(\Pi_g)$ – $010(\Pi_u)$, were observed for each of six isotopologues of CdH_2. Since there is no connection between the $011(\Pi_g)$ – $010(\Pi_u)$ band and the other two bands, the $011(\Pi_g)$ – $010(\Pi_u)$ band was fitted separately. Perturbations were observed in the $001(\Sigma_u^+)$, $002(\Sigma_g^+)$ and $011(\Pi_g)$ vibrational states of CdH_2. We tried to consider these three perturbations in the fits, and succeeded in the deperturbation of the $001(\Sigma_u^+)$ state, but not in the deperturbation of $002(\Sigma_g^+)$ and $011(\Pi_g)$ states because the hot band lines involving these two excited states are very weak, and the most perturbed lines are missing. The energy level expression, Eq. (6.1), was used for the $002(\Sigma_g^+)$ state and the usual energy level expression for Π states:

$$E(J) = G(v_1, v_2, v_3) + B[J(J+1) - l^2] - D[J(J+1) - l^2]^2 \pm \tfrac{1}{2}[qJ(J+1) + q_D J^2(J+1)^2], \qquad (6.2)$$

for the $011(\Pi_g)$ and $010(\Pi_u)$ states. In Eq. (6.2), l is the vibrational angular momentum quantum number ($l = 1$ for Π states); q and q_D are l-type doubling parameters; the upper (lower) sign refers to e (f) parity. The observed line positions and the output files of the fits for $011(\Pi_g)$ – $010(\Pi_u)$ band of six CdH_2 isotopologues have been published in the supplementary tables of Ref. [24]. Since this band is relatively weak and suffers from perturbations, a weight of 0.002 cm^{-1} was used for most lines, and the perturbed excited state levels were fitted as term values. The constants obtained are given in Table 6.2. The l-type doubling parameter q is negative in the $011(\Pi_g)$ and $010(\Pi_u)$ vibrational states of CdH_2, so that the f parity level lies above the e parity level for a given J. The energy of the bending mode (v_2) cannot be determined directly from the fit, and therefore the value of $G(0, 1, 0) - G(0, 0, 0)$ was fixed at 0.0 in separate fits of the $011(\Pi_g)$ – $010(\Pi_u)$ band of each isotopologue of CdH_2. However, v_2 has been observed at 601.7 cm^{-1} in an argon matrix for CdH_2, and was calculated to be 574 cm^{-1} at the CCSD(T) level of theory [16]. Values for v_2 can also be estimated by deperturbation of the $001(\Sigma_u^+)$ state and from the relationship involving q_{010}, B_e, ω_2 and ω_3 [27–29] (see below).

The perturbations in the $001(\Sigma_u^+)$ state are small, and using the ordinary energy expression in Eq. (6.1), a reasonable fit of the $001(\Sigma_u^+) - 000(\Sigma_g^+)$ band could be obtained for each CdH_2 isotopologue by deweighting the perturbed lines. The perturbation in the $001(\Sigma_u^+)$ state could be caused by either the $03^10(\Pi_u)$ or the $03^30(\Phi_u)$ levels. The $001(\Sigma_u^+)$ rotational levels have *e* parity, and only interact with the $03^10(\Pi_u)$ or $03^30(\Phi_u)$ state *e* parity levels. The $03^10(\Pi_u)$ and $03^30(\Phi_u)$ levels also interact with each other, and the detailed theory of their interaction was derived by Maki *et al*. [27]. This interaction depends on the separation between the $03^10(\Pi_u)$ and $03^30(\Phi_u)$ levels. Because there was no information on this separation, this interaction was ignored. To find which state, $03^10(\Pi_u)$ or $03^30(\Phi_u)$, causes the perturbation in the $001(\Sigma_u^+)$ state, two different fits were performed for the $001(\Sigma_u^+) - 000(\Sigma_g^+)$ band. If the $03^30(\Phi_u)$ state is assumed to cause the perturbation, then the $001(\Sigma_u^+) - 000(\Sigma_g^+)$ band cannot be fitted, but this band can be easily fitted if the $03^10(\Pi_u)$ state is assumed to cause the perturbation. In addition, it can be clearly seen from the spectra of the $001(\Sigma_u^+) - 000(\Sigma_g^+)$ band that the perturbation shifts the $001(\Sigma_u^+)$ state $J = 12–14$ levels to lower energy, and shifts the $J = 15–17$ levels to higher energy, which means the perturbation in $001(\Sigma_u^+)$ state is caused by a state with a smaller B_{eff} value. Using B_{000} obtained from the fit of $001(\Sigma_u^+) - 000(\Sigma_g^+)$ band with perturbed lines deweighted, and B_{010} and q_{010} values obtained from the fits of the $011(\Pi_g) - 010(\Pi_u)$ band, the effective *B* values (B_{eff}) can be estimated for the *e* levels of the $03^10(\Pi_u)$ and $03^30(\Phi_u)$ states [28,29]. Compared with the *B* value for the $001(\Sigma_u^+)$ state, the estimated B_{eff} value of the $03^10(\Pi_u)$ state *e* levels is smaller, while the estimated B_{eff} value for the $03^30(\Phi_u)$ state *e* levels is larger. Therefore, the $03^10(\Pi_u)$ state is believed to be responsible for the perturbations in the $001(\Sigma_u^+)$ state.

The following Hamiltonian matrix was used for the interacting 001 (Σ_u^+) and $03^10(\Pi_u)$ *e* levels [27]:

$$\mathbf{H} = \begin{pmatrix} E_\Sigma^0 & W_{01} \\ W_{01} & E_\Pi^0 + W_{11} \end{pmatrix}, \tag{6.3}$$

where

$$E_\Sigma^0 = G(0,0,1) + B_{001}J(J+1) - D_{001}J^2(J+1)^2; \tag{6.4}$$

$$E_\Pi^0 = G(0,3^1,0) + B_{03^10}[J(J+1)-1] - D_{03^10}[J(J+1)-1]^2; \tag{6.5}$$

$$W_{11} = +\tfrac{1}{2}[q_{03^10}J(J+1) + q_{D03^10}J^2(J+1)^2]; \tag{6.6}$$

$$W_{01} = -k_{01}[J(J+1)]^{1/2}. \tag{6.7}$$

$E_\Sigma{}^0$ is the usual energy expression for a Σ^+ state, and $(E_\Pi{}^0 + W_{11})$ is the ordinary energy expression for Π ($l_2 = 1$) state *e* levels. W_{01} is the term connecting the $001(\Sigma_u^+)$ state with the $03^10(\Pi_u)$ state and k_{01} is the perturbation constant. The *J*-dependence of W_{01} was determined by applying the $\hat{J}_+$ operator to

the Π state basis function [Eq. (1.41)]. No transitions from the $03^10(\Pi_u)$ state were observed, so the only constants for this state that can be obtained from fitting the perturbed $001(\Sigma_u^+) - 000(\Sigma_g^+)$ band are the vibrational energy and the perturbation constant, k_{01}. For all six isotopologues of CdH_2, the B_{03^10} constant was fixed at 2.931915 cm^{-1}; the D_{03^10} constant was set to 3.3128×10^{-5} cm^{-1}; the q_{03^10} constant was $2q_{010} = -0.087598$ cm^{-1}; q_{D03^10} was $2q_{D010} = 3.378\times10^{-6}$ cm^{-1}. The above values were calculated in the following ways [27]:

$$B_{03^10} = B_{000} - 3\alpha_2 \text{ with } \alpha_2 = B_{000} - B_{010}; \tag{6.8}$$

$$D_{03^10} = D_{000} + 3\beta_2 \text{ with } \beta_2 = D_{010} - D_{000}; \tag{6.9}$$

$$q_{03^10} = 2q_{010}; \tag{6.10}$$

$$q_{D03^10} = 2\, q_{D010}. \tag{6.11}$$

B_{000}, B_{010}, D_{000}, D_{010}, q_{010} and q_{D010} from the main isotopologue $^{114}CdH_2$ were used in all of the above calculations for the different isotopologues of CdH_2. The observed line positions and the output files of the fits are provided in the supplementary tables of Ref. [24]. The fits are quite good, and most lines for these two bands can be fitted with residuals (observed – calculated values) of the order of 0.001 cm^{-1}.

Although the usual energy level expression [Eq. (6.1)] was used for the perturbed $002(\Sigma_g^+)$ state, the perturbed lines do not need to be deweighted because the perturbation of the $002(\Sigma_g^+)$ state by the $200(\Sigma_g^+)$ state is a global interaction [28,29]. The levels of the $002(\Sigma_g^+)$ and $200(\Sigma_g^+)$ states do not cross, and lines of the $002(\Sigma_g^+) - 001(\Sigma_u^+)$ transition can still be fitted with the ordinary energy level expression for the $002(\Sigma_g^+)$ state to produce effective molecular constants.

The constants obtained for CdH_2 are provided in Table 6.2. The band origins obtained for the $001(\Sigma_u^+) - 000(\Sigma_g^+)$ transition are 1771.52958(22) cm^{-1} for $^{114}CdH_2$ and 1278.31167(28) cm^{-1} for $^{114}CdD_2$, which agree well with the observed argon matrix values of 1753.8 cm^{-1} and 1264.9 cm^{-1}, and the *ab initio* values of 1790 cm^{-1} and 1278 cm^{-1} at the CCSD(T) level [16]. The difference between the band origins of the $001(\Sigma_u^+) - 000(\Sigma_g^+)$ transitions of $^{112}CdH_2$ and $^{114}CdH_2$, which is the isotopic frequency shift between $^{112}CdH_2$ and $^{114}CdH_2$, is 0.26459(32) cm^{-1}, and matches the observed isotopic splitting of 0.25 cm^{-1} in the matrix-isolation experiment and the *ab initio* value of 0.27 cm^{-1} [17]. However, the difference between the band origins of the $002(\Sigma_g^+) - 001(\Sigma_u^+)$ transitions of $^{112}CdH_2$ and $^{114}CdH_2$ is only 0.01810(64) cm^{-1}, which is much smaller than the isotopic splitting in the $001(\Sigma_u^+) - 000(\Sigma_g^+)$ transition (Fig. 6.2). The change in the isotopic splitting in the $002(\Sigma_g^+) - 001(\Sigma_u^+)$ band is caused by the mixing of $002(\Sigma_g^+)$ and $200(\Sigma_g^+)$ vibrational levels (ν_3 and ν_1 were calculated to be 1790 cm^{-1} and 1794 cm^{-1} at the CCSD(T) level [16]).

Table 6.2 Spectroscopic constants (in cm^{-1}) for CdD_2 (all uncertainties are 1σ).

	Level	*G*v -ZPE	$B_{v_1v_2v_3}$	$D_{v_1v_2v_3}/10^{-5}$	$q/10^{-2}$	$q_D/10^{-6}$	$(k_{01}/10^{-3})^b$
$^{110}CdH_2$	000	0.0	2.952567(12)	3.1871(21)			
	001	1772.06742(32)	2.919633(12)	3.1990(21)			4.75(14)
	03^10^a	1782.4790(63)					
	002	3541.10656(57)	2.877639(12)	3.0046(19)			
	010[c]	*E*	2.945723(43)	3.256(10)	-4.3584(83)	0.84(19)	
	011	*E* + 1759.08511(91)	2.912967(40)	3.2371(89)	-4.3026(81)	1.37(18)	
$^{111}CdH_2$	000	0.0	2.9525601(88)	3.1851(14)			
	001	1771.92991(24)	2.9196326(81)	3.1984(12)			4.97(11)
	03^10^a	1782.3252(53)					
	002	3540.96015(42)	2.8775653(86)	2.9994(13)			
	010[c]	*E*	2.945762(27)	3.2665(54)	-4.3462(56)	0.59(12)	
	011	*E* + 1758.94909(65)	2.913011(30)	3.2439(72)	-4.2941(62)	1.27(15)	
$^{112}CdH_2$	000	0.0	2.9525731(78)	3.18682(96)			
	001	1771.79417(24)	2.9196487(79)	3.1975(10)			4.96(12)
	03^10^a	1782.1914(55)					
	002	3540.81222(42)	2.8775436(85)	2.9990(12)			
	010[c]	*E*	2.945667(27)	3.2267(47)	-4.3717(53)	1.489(93)	
	011	*E* + 1758.81855(51)	2.912964(67)	3.2265(50)	-4.3097(54)	1.70(10)	
$^{113}CdH_2$	000	0.0	2.9525369(95)	3.1771(13)			
	001	1771.66028(28)	2.9196330(95)	3.1913(13)			5.03(12)
	03^10^a	1782.0735(53)					
	002	3540.67032(70)	2.877475(11)	2.9941(16)			
	010[c]	*E*	2.945816(31)	3.2681(60)	-4.3899(60)	1.86(12)	
	011	*E* + 1758.68932(64)	2.913088(30)	3.2585(60)	-4.3342(62)	2.33(12)	
$^{114}CdH_2$	000	0.0	2.9525385(77)	3.17921(99)			
	001	1771.52958(22)	2.9196443(79)	3.1942(11)			4.97(11)
	03^10^a	1781.9196(54)					
	002	3540.52953(36)	2.8774478(84)	2.9962(12)			
	010[c]	*E*	2.945659(22)	3.2222(38)	-4.3799(45)	1.689(76)	
	011	*E* + 1758.56158(50)	2.912946(23)	3.2142(43)	-4.3220(46)	2.035(84)	
$^{116}CdH_2$	000	0.0	2.952542(16)	3.1839(40)			
	001	1771.27382(34)	2.919674(15)	3.2027(32)			5.38(13)
	03^10^a	1781.6493(77)					
	002	3540.25933(56)	2.877355(16)	2.9915(40)			

[a] The vibrational energy of 03^10 (Π_u) state was obtained by the observed perturbation between 03^10 (Π_u) state and $001(\Sigma_u^+)$ state with *B* fixed at 2.931915 cm^{-1}, *D* at 3.3128×10^{-5} cm^{-1}, $q = -0.087598$ cm^{-1} and $q_D = 3.378\times10^{-6}$ cm^{-1} for the $03^10(\Pi_u)$ state.

[b] Perturbation constant connecting the $001(\Sigma_u^+)$ state with the $03^10(\Pi_u)$ state.

[c] The 011 – 010 hot band was fitted separately from the 001 – 000 and 002 – 001 bands, and the value of *E* was not determined from our experiment and was fixed at 0.0. The ν_2 value was estimated to be 594 cm^{-1} from our work (see the text). Also ν_2 has been observed as 601.7 cm^{-1} in an argon matrix and was calculated to be 574 cm^{-1} at CCSD(T) level of theory [16].

The $03^10(\Pi_u)$ state vibrational energies ($G(0, 3^1, 0) - G(0, 0, 0) = 3\omega_2 + 15x_{22} + \frac{3}{2}x_{12} + \frac{3}{2}x_{23} + g_{22}$ [29]) of the six CdH_2 isotopologues were used to estimate ν_2 ($G(0, 1^1, 0) - G(0, 0, 0) = \omega_2 + 3x_{22} + \frac{1}{2}x_{12} + \frac{1}{2}x_{23} + g_{22}$ [29]) for CdH_2. Because no information on g_{22}, x_{22}, x_{12} and x_{23} are available, ν_2 was estimated by using $\nu_2 \approx [G(0, 3^1, 0) - G(0, 0, 0)]/3$, and an average value of 594 cm^{-1} was obtained for ν_2. The value of ν_2 can also be estimated [27–29] from the *l*-type doubling constants q_{010} using:

$$q_{010} = -\frac{2B_e^{\,2}}{\omega_2}\left(1 + \frac{4\omega_2^{\,2}}{\omega_3^{\,2} - \omega_2^{\,2}}\right). \tag{6.12}$$

In Eq. (6.8), equilibrium constants are required but are not available, so B_{000}, ν_2 and ν_3 were used instead. The q_{010}, B_{000} and $G(0, 0, 1) - G(0, 0, 0)$ constants from different isotopologues of CdH_2 were used to calculate ν_2 for each isotopologue, and values ranging from 614 cm^{-1} to 640 cm^{-1} were obtained. The average value for ν_2 , estimated from Eq. (6.8), is 632 cm^{-1}, which differs by about 38 cm^{-1} from the estimated value of 594 cm^{-1} from $[G(0, 3^1, 0) - G(0, 0, 0)]/3$. The ν_2 value is very sensitive to the value of q_{010} and, for example, the $^{114}CdH_2$ q_{010} value is –0.043799(45) cm^{-1} (Table 6.2). A value of 622 cm^{-1} was obtained for ν_2 if a value of –0.043799 cm^{-1} was used for q_{010}, and values of 625 cm^{-1} and 618 cm^{-1} were obtained if –0.043754 cm^{-1} and –0.043844 cm^{-1} (–0.043799 cm^{-1} minus or plus its one sigma uncertainty) were used for q_{010}, respectively. A value of 594 cm^{-1} was obtained from $[G(0, 3^1, 0) - G(0, 0, 0)]/3$, which is closer to the argon matrix value of 601.7 cm^{-1} and the *ab initio* value of 574 cm^{-1} at the CCSD(T) level of theory [16].

Table 6.3 Spectroscopic constants (in cm^{-1}) for $^{114}CdH_2$ and $^{114}CdD_2$.

	$^{114}CdH_2$	$^{114}CdD_2$
B_0	2.9525385(77)	1.4842084(96)
r_0/Å	1.6830340(22)	1.6791717(54)
α_2	0.006880(23)	–
α_3	0.032894(11)	0.011914(14)
q_{010}	–0.0043799(45)	–
$\nu_2(\pi_u)$	594[a]	–
$\nu_3(\sigma_u)$	1771.52958(22)	1278.31167(28)
x_{23}	–12.96800(65)	–
x_{33}	–1.26482(65)[b]	–

[a] Estimated from $\nu_2 \approx [G(0, 3^1, 0) - G(0, 0, 0)]/3$ (see the text).

[b] Not reliable because the vibrational origin of the $002(\Sigma_g^+)$ state is perturbed by the $200(\Sigma_g^+)$ state (see the text).

The B_{000} value obtained for each isotopologue was used to calculate the corresponding Cd–H or Cd–D r_0 bond distance by use of the moment of inertia equation (Eq. (1.30)). The average Cd–H and Cd–D r_0 bond distances were calculated to be 1.683028(10) Å and 1.679161(16) Å, respectively, with

two standard deviation statistical errors enclosed in parentheses. These errors are obtained from the six values obtained from each isotopologue of CdH_2 or CdD_2. Since both dihydride and dideuteride were observed for each of the six isotopes of cadmium, the r_s structure could be calculated for CdH_2 by using Kraitchman's procedure for multiple isotopic substitutions [30]. The formula used for CdH_2 is:

$$r_s = \left[\frac{1}{2(m_D - m_H)} \left(I_z' - I_z \right) \right]^{1/2}, \tag{6.13}$$

where m_D and m_H are the masses of H and D atoms, respectively; I_z' and I_z are the moments of inertia of the H/D isotopologues with the same Cd atom. The average r_s bond distance is determined to be 1.675279(37) Å, with two standard deviation errors enclosed in parentheses. Again, the error was computed from the six possible CdH_2 and CdD_2 pairs. Both r_0 and r_s bond distances are reasonably close to the theoretical r_e values, which range from 1.67 Å to 1.74 Å [1,14,16,21–23]. Table 6.3 lists the constants obtained for the main isotopologues, $^{114}CdH_2$ and $^{114}CdD_2$. Since the $002(\Sigma_g^+)$ vibrational energy level obtained from the fit is perturbed by the nearby $200(\Sigma_g^+)$ state, the value of –1.26482(65) cm^{-1} obtained for the CdH_2 x_{33} equilibrium constant is not reliable.

6.4 Conclusions

The vibration-rotation emission spectra of CdH_2 and CdD_2 molecules have been recorded at high resolution using a Fourier transform spectrometer. The molecules were generated in a furnace-discharge emission source by reaction of cadmium vapor with molecular hydrogen or deuterium. The fundamental bands for the antisymmetric stretching mode (ν_3) of CdH_2 and CdD_2 were detected at about 1771.5 cm^{-1} and 1278.3 cm^{-1}, respectively. In addition, the $002(\Sigma_g^+) - 001(\Sigma_u^+)$ and $011(\Pi_g) - 010(\Pi_u)$ hot bands were observed for CdH_2. Spectroscopic constants were determined for each of the twelve observed isotopologues: $^{110}CdH_2$, $^{111}CdH_2$, $^{112}CdH_2$, $^{113}CdH_2$, $^{114}CdH_2$, $^{116}CdH_2$, $^{110}CdD_2$, $^{111}CdD_2$, $^{112}CdD_2$, $^{113}CdD_2$, $^{114}CdD_2$, $^{116}CdD_2$. The average Cd–H and Cd–D bond distances (r_0) were determined to be 1.683028(10) Å and 1.679161(16) Å, respectively.

6.5 References

[1] L. Andrews, Chem. Soc. Rev. **33**, 123 (2004).

[2] H. Körsgen, W. Urban and J.M. Brown, J. Chem. Phys. **110**, 3861 (1999).

[3] P.F. Bernath, A. Shayesteh, K. Tereszchuk and R. Colin, Science **297**, 1323 (2002).

[4] A. Shayesteh, D.R.T. Appadoo, I. Gordon and P.F. Bernath, J. Chem. Phys. **119**, 7785 (2003).

[5] A. Shayesteh, D.R.T. Appadoo, I. Gordon and P. Bernath, J. Am. Chem. Soc. **126**, 14356 (2004).

[6] A. Shayesteh, S. Yu and P.F. Bernath, Angew. Chem. Eur. J. **11**, 4709 (2005).

[7] G.D. Barbaras, C. Dillard, A.E. Finholt, T. Wartik, K.E. Wilzbach and H.I. Schlesinger, J. Am. Chem. Soc. **73**, 4585 (1951).

[8] A. Sanz-Medel, M.C. Valdés-Heviay Temprano, N. Bordel García and M.R. Fernández de la Campa, Anal. Chem. **67**, 2216 (1995).

[9] A.S. Luna, R.E. Sturgeon and R.C. de Campos, Anal. Chem. **72**, 3523 (2000).

[10] Y.L. Feng, R.E. Sturgeon and J.W. Lam, Anal. Chem. **75**, 635 (2003).

[11] I. Wallace, D.J. Funk, J.G. Kaup and W.H. Breckenridge, J. Chem. Phys. **97**, 3135 (1992).

[12] W.H. Breckenridge, J. Phys. Chem. **100**, 14840 (1996).

[13] W.H. Breckenridge and J.H. Wang, Chem. Phys. Lett. **139**, 28 (1987).

[14] J.A. Boatz, M. Gutowski and J. Simon, J. Chem. Phys. **96**, 6555 (1992).

[15] A. Ramírez-Solís and S. Castillo A., J. Chem. Phys. **100**, 8251 (1994).

[16] T.M. Greene, W. Brown, L. Andrews, A.J. Downs, G.V. Chertihin, N. Runeberg and P. Pyykkö, J. Phys. Chem. **99**, 7925 (1995).

[17] X. Wang and L. Andrews, J. Phys. Chem. A **108**, 11006 (2004).

[18] V.A. Macrae, T.M. Greene and A.J. Downs, J. Phys. Chem. A **108**, 1393 (2004).

[19] V.A. Macrae, J.C. Green, T.M. Greene and A.J. Downs, J. Phys. Chem. A 108, 9500 (2004).

[20] V.A. Macrae, T.M. Greene and A.J. Downs, Phys. Chem. Chem Phys. **6**, 4586 (2004).

[21] P. Pyykkö, J. Chem. Soc. Faraday Trans. 2 **75**, 1256 (1979).

[22] M. Kaupp and H.G.V. Schnering, Inorg. Chem. **33**, 4179 (1994).

[23] J. Cioslowski, P. Piskorz and P. Rez, J. Chem. Phys. 106 (1997), 3607.

[24] S. Yu, A. Shayesteh and P.F. Bernath, J. Chem. Phys. **122**, 194301 (2005).

[25] P.F. Bernath, *Spectra of Atoms and Molecules*, 2nd ed., Oxford University Press, New York (2005).

[26] I. Mills, T. Cvitas, K. Homann, N. Kallay and K. Kuchitsu, *Quantities, units and symbols in physical chemistry*, 2nd edition, Blackwell Scientific, Oxford, 1993.

[27] A.G. Maki, Jr. and D.R. Lide, Jr., J. Chem. Phys. **47**, 3026 (1967).

[28] D. Papoušek and M. R. Aliev, *Molecular Vibrational-Rotational Spectra*, Elsevier, Amsterdam, 1982.

[29] G. Herzberg, *Electronic Spectra of Polyatomic Molecules*, Van Nostrand Reinhold, New York, 1966.

[30] W. Gordy and R.L. Cook, *Microwave Molecular Spectra*, Interscience Publishers, New York, 1970.

Chapter 7

Fourier transform infrared emission spectroscopy of BeF_2

7.1 Introduction

In 1991, the Bernath group published a paper on the high-resolution infrared emission spectrum of BeF_2 [1]. A series of spectra were recorded at temperatures ranging from 500°C to 1000°C. The spectrum obtained at around 700°C was the best one (with the least amount of congestion but good intensity), and was analyzed. Eight vibration-rotation bands in the ν_3 fundamental region near 1550 cm^{-1} were assigned, and the antisymmetric stretching frequency ν_3 was determined. This chapter reports on the analysis of the spectrum recorded with the BeF_2 vapor at 1000°C, in which the combination bands are much stronger. The results presented in this chapter have been published in Ref.[2].

The geometry of triatomic metal halide molecules has been a topic of discussion in many papers. The extensive experimental and computational studies have been reviewed recently by Hargittai [3]. The experimental studies include electron diffraction, photoelectron spectroscopy, matrix isolation, Raman spectroscopy, infrared emission and absorption, and laser-induced fluorescence. The application of these experimental techniques to the determination of metal halide structure was reviewed recently by Beattie [4], and the problems and limits were discussed in detail [3,4]. The electron diffraction method was the most used, and the equilibrium structures determined by this method are tabulated in the review by Spiridonov *et al*. [5]. There are extensive low resolution spectroscopic studies, but very little high resolution data with resolved rotational structure is available. High resolution spectroscopy is one of the most reliable methods used to determine molecular geometries, and is available only for a few metal dihalides, e.g., BeF_2 [1], $FeCl_2$ [6], $NiCl_2$ [7,8], and $CuCl_2$ [9].

The major interest in metal dihalides concerns whether they are linear or bent. The early electron diffraction studies by Spiridonov *et al*. [10,11] suggested linear geometries for all alkaline earth dihalides, although the bending angles were determined with large uncertainties (±30°–40°). Simple bonding rules such as the valence-shell electron-pair repulsion (VSEPR) theory and Walsh's rules predicted linear geometries for all alkaline earth dihalides, and it was generally believed that these bonding rules were reliable. Klemperer and coworkers [14–14], however, used the technique of molecular beam deflection by an inhomogeneous electric field to show that CaF_2, $SrCl_2$, and SrF_2, and all of the barium dihalides have permanent dipoles, and are therefore bent. These results were confirmed later by the observation of the infrared and Raman spectra of the alkaline earth dihalides in matrices [1,3,15–22]. It was noted that the alkaline earth halides become increasingly bent as the metal becomes heavier and the halogen becomes lighter.

The failure of the VSEPR model and Walsh's rules to predict these bent structures prompted the development of improved models. Two physical models, *d*-orbital participation [23–32] and core polarization [12,13,33–46], were used to explain these unexpected bent structures, and have been discussed in detail in the reviews by Hargittai [3] and Kaupp [47]. In the *d*-orbital participation

model, the lighter metals (e.g., Be and Mg) have only valence *ns* and *np* orbitals for covalent bonding, leading to *sp* hybridization, which results in a linear structure. The heavier metals (e.g., Ca, Sr, and Ba) may employ their low-lying (*n*–1)*d* orbitals for *sd* hybridization, which results in a nonlinear structure. In the core polarization model, ionic ligands induce an angle-dependent dipole moment on the large, polarizable central ion of a MX_2 molecule, which stabilizes the bent structure relative to the linear structure. These two models appear to be inconsistent at first sight, and have been discussed over many years. It has been argued that both core polarization and *d*-orbital participation play a role in bonding in these molecules, and they are not strictly separable and "are the two sides of the same coin" [3,47–51]. For example, *d*-orbitals participate strongly in the bonding, as determined by *ab initio* calculations, and are also required to compute reliable polarizabilities. Szentpaly *et al*. [49,51] proposed the use of a "softness criterion", which combined elements of these two models. Unfortunately, this criterion does not account for the structures of all the alkaline earth dihalides [47,50]. No simple model has been found yet to account for the bent vs. linear structures.

It is now established that all beryllium and magnesium dihalides are linear, SrF_2 and the barium dihalides are bent, and the others are "quasilinear" with a small barrier to linearity [3,29,47]. The linear structure of BeF_2 was first confirmed by the failure to observe the refocusing of the molecular beam by an electric field [13]. Büchler and Klemperer [52] investigated the low resolution gas-phase infrared spectrum of BeF_2, and they assigned bands at 825 and 1520 cm^{-1} to the ν_2 and ν_3 vibrational frequencies, with the ν_2 frequency turning out to be a misassignment. In the matrix isolation work of Snelson [16], ν_2 and ν_3 were determined to be 345 and 1555 cm^{-1} with empirical correction for the matrix shifts. The previous Bernath laboratory study [1] was the first high-resolution study of BeF_2, and the ν_3 frequency and the equilibrium bond distance were determined to be 1555.04792(5) cm^{-1} and 1.3729710(95) Å, respectively. Later, an equilibrium bond length of 1.374(4) Å was re-determined from a gas-phase electron diffraction experiment [53]. In Hargittai's latest review [3], the gas-phase ν_1, ν_2 and ν_3 frequencies are estimated to be 760±14, 334 and 1544 cm^{-1}, respectively. The value of ν_1 was estimated to be 680 cm^{-1} by Snelson [16] from valence force constants and 594±60 cm^{-1} by Vogt *et al*. [53] based on force constants estimated from electron diffraction results. There are only a few calculations at correlated levels of theory [54–57] on the structure and vibrational frequencies of BeF_2. In the recent study by Lee and Wright [57], the best theoretical value for the equilibrium BeF bond length was estimated to be 1.380 ± 0.005 Å, and the ω_1, ω_2, and ω_3 harmonic frequencies were predicted to be in the ranges of 715 – 733, 345 – 357, and 1555 – 1597 cm^{-1}, respectively.

In the present work, the ν_3 fundamental band, the $\nu_1+\nu_2$, $\nu_1+\nu_3$, and $2\nu_2+\nu_3$ combination bands, and eighteen hot bands were assigned. The ν_1, ν_2, and ν_3 vibrational frequencies were directly determined by fitting most of these bands together. The traditional equilibrium vibrational and rotational constants were obtained for BeF_2 by simultaneously fitting the observed vibrational term values and *B* rotational constants.

7.2 Experimental details

The experimental details can be found in the previous BeF_2 paper by the Bernath group [1]. Gas-phase BeF_2 was produced by heating solid BeF_2 to about 1000°C in the high temperature tube

furnace, which has been described in Section 2.1.1. The experiments were carried out without a DC discharge. The emission spectrum was recorded at a resolution of 0.0055 cm^{-1} in the 500 – 2900 cm^{-1} region with the National Solar Observatory Fourier transform spectrometer at Kitt Peak [1].

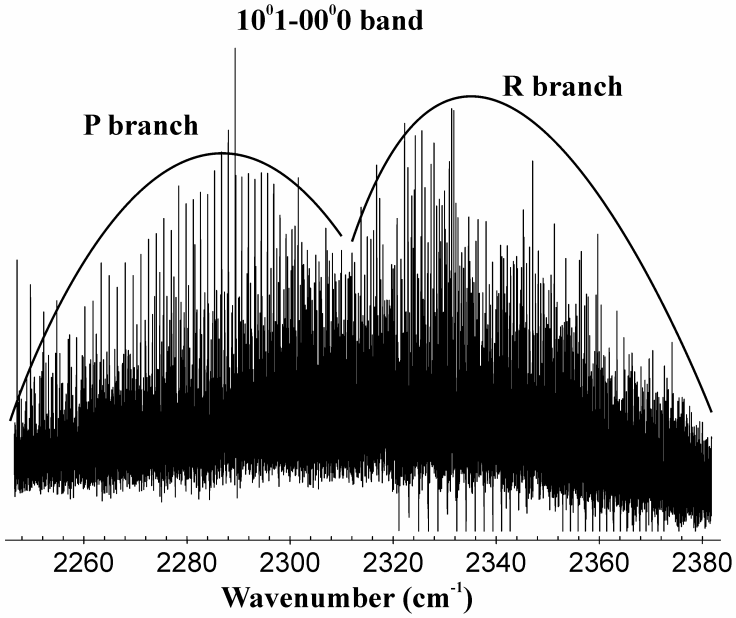

Figure 7.1 An overview of the infrared emission spectrum of BeF_2 in the region of the $\nu_1 + \nu_3$ combination band. This spectrum was recorded at the temperature of 1000°C, and the $10^0 1(\Sigma_u)$–$00^0 0(\Sigma_g)$ band is the strongest transition in this region.

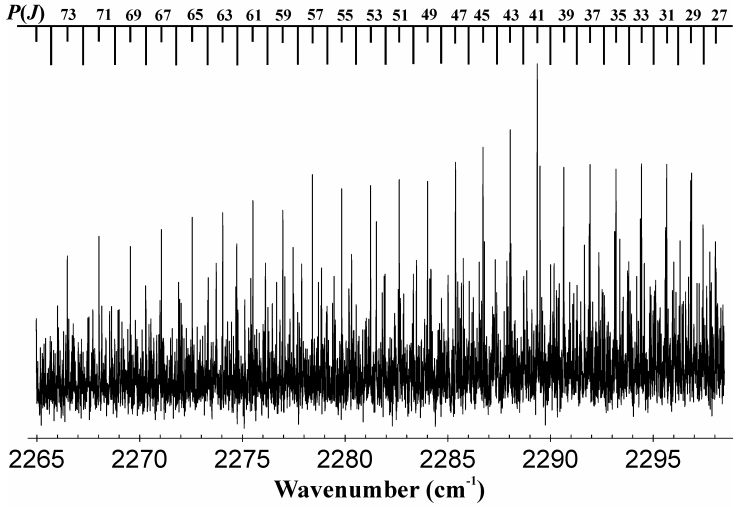

Figure 7.2 An expanded view of the *P* branch of the $10^0 1(\Sigma_u) – 00^0 0(\Sigma_g)$ transition for BeF_2. The 3:1 intensity alternation is due to fluorine nuclear spin statistics.

7.3 Results and discussion

At a temperature of 1000°C, the $\nu_1 + \nu_3$ and $2\nu_2 + \nu_3$ combination bands are roughly 10 times weaker, and the $\nu_1 + \nu_2$ combination band is about 40 times weaker than the ν_3 fundamental band. Figure 7.1 shows an overview spectrum in the region of the $\nu_1 + \nu_3$ combination band. The $10^0 1(\Sigma_u)$–$00^0 0(\Sigma_g)$ band was the strongest combination band, and an expanded view is shown in Figure 7.2. Nuclear spin statistics due to the equivalent fluorine nuclei (I=1/2) produces a 3:1 intensity alternation [58]. The program WSPECTRA written by Carleer [59] was used to determine the line positions. The temperature is sufficiently high that the spectrum contains strong impurity CO emission lines, which were used to calibrate the spectrum. Note that this calibration is an improvement over the previous calibration based on water absorption lines [1]. The absolute accuracy of the measured wavenumbers is approximately 0.001 cm^{-1} for the strong bands and 0.002 cm^{-1} for the weak transitions. A color Loomis-Wood program [60] was used to pick out the bands.

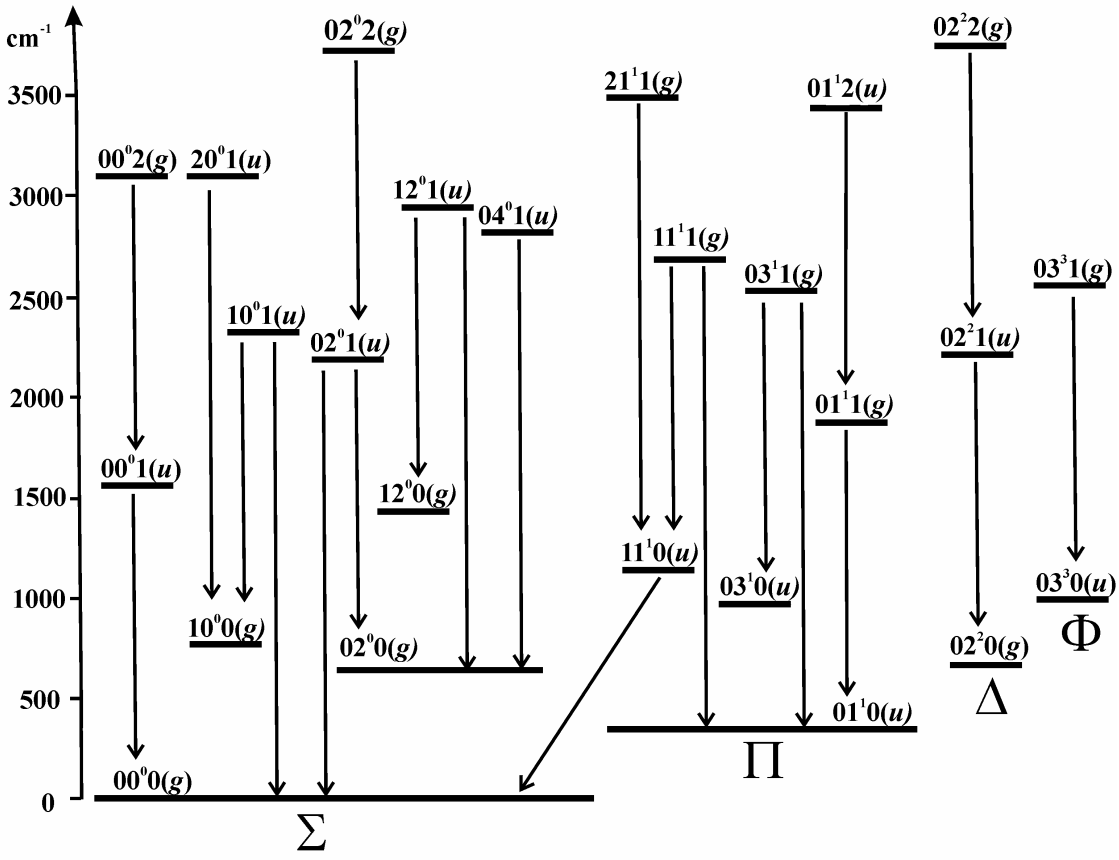

Figure 7.3 An energy level diagram indicating the assigned emission bands for BeF_2. The $11^1 0(\Pi_u)$–$00^0 0(\Sigma_g)$ combination band connects all the Π–Π and Σ–Σ transitions together.

Figure 7.3 shows an energy level diagram indicating the assigned transitions. In the initial stage of assignments, a least-squares fit was performed for each band that was picked out. The customary energy level expression for linear triatomic molecules was used (Chapter 1):

$$E(J) = G(\nu_1, \nu_2^l, \nu_3) + BJ(J+1) - DJ^2(J+1)^2 \pm \tfrac{1}{2}[qJ(J+1) + q_D J^2(J+1)^2], \quad (7.1)$$

where l is the vibrational angular momentum quantum number (l = 0, 1, 2, 3 for Σ, Π, Δ and Φ states, respectively); q and q_D are l-type doubling parameters, $q = q_D = 0$ for Σ and Φ states, q and q_D are non-zero for Π states, $q = 0$ and $q_D \neq 0$ for Δ states; the upper (lower) sign refers to the e (f) parity. In Eq. (7.1), $G(\nu_1, \nu_2^l, \nu_3)$ is the vibrational (J = 0) energy of the (ν_1, ν_2^l, ν_3) state relative to the zero point energy (ZPE), $G(0, 0^0, 0)$. The *ab initio* rotational constants B and D calculated by J. Koput [2] agree very well with those obtained from the previous study [1], and were thus used to guide the assignments of the new bands. The absolute J assignments of the new Σ–Σ and Π–Π bands were obtained by shifting the J assignments until the obtained rotational constants B and D matched the *ab initio* values.

The $11^10(\Pi_u)$–$00^00(\Sigma_g)$ transition connects all of the Σ–Σ and Π–Π transitions together (Figure 7.3). In the region of the $\nu_1 + \nu_2$ combination band, some fragmentary branches were picked out from the spectrum, but none of these branches could be fitted together to obtain a band. A different method was therefore used to assign this band. Because spectroscopic constants were available for the upper and lower vibrational levels from other bands, only the band origin of the $11^10(\Pi_u)$–$00^00(\Sigma_g)$ transition was needed to predict the line positions. A value of 1200 cm^{-1} was used for the band origin to predict the line positions and the differences between the adjacent lines were calculated for each of the three predicted branches, P, Q and R. The differences between the adjacent lines for the Q branch obtained from the experimental data were matched to the values from the predicted Q branch, and the absolute J assignment was obtained. The band origin obtained from the Q branch, 1138.003 cm^{-1}, was then used to pick out the P and R branches from the spectrum.

Finally all assigned Σ–Σ, Π–Π and Π–Σ transitions were fitted together. As no band connects the Δ–Δ and Φ–Φ transitions with the Σ and Π states (Figure 7.3), they were fitted separately. The vibrational energies of the $02^20(\Delta_g)$ and $03^30(\Phi_u)$ levels could not determined from the present experiment, and were set to zero in the separate fits. The spectroscopic constants obtained are given in Table 7.1. The ν_1, ν_2, and ν_3 frequencies were determined from the present study to be 769.09433(21), 342.61453(34) and 1555.04795(11) cm^{-1}, respectively. Table 7.1 also gives the difference between the observed and *ab initio* calculated values. The difference is in the order of 0.0002 cm^{-1} for the B rotational constants, and a few cm^{-1} for the vibrational energies. The observed line positions and the output files of the least-squares fits are provided in the supplementary Tables which have been published in Ref. [2]. The uncertainties of 0.001 and 0.002 cm^{-1} were used for most lines of the strong and weak bands, respectively. An uncertainty of 0.005 cm^{-1} was used for blended lines near band origins and band heads.

Table 7.1 Spectroscopic constants (in cm^{-1}) for BeF_2 and the difference between the observed and *ab initio* calculated values.

	G_v–ZPE		B		$D/10^{-7}$		$q/10^{-4}$		$q_D/10^{-9}$	
Level	Obs.	Obs.–Calc.	Obs.	Obs.–Calc.	Obs.	Obs.–Calc.	Obs.	Obs.–Calc.	Obs.	Obs.–Calc.
00^00	0.0	0.0	0.23498453(31)	0.00021	1.00876(21)	-0.0053				
00^01	1555.04795(11)	-2.8	0.23253814(31)	0.00020	1.00027(20)	-0.0054				
00^02	3092.55290(17)	-5.7	0.23011981(32)	0.00018	0.99142(22)	-0.0056				
02^00	645.96443(23)	-0.1	0.23654774(34)	0.00020	1.27599(26)	-0.0099				
02^01	2188.30472(19)	-3.0	0.23418088(34)	0.00019	1.26945(26)	-0.0081				
02^02	3717.80000(34)	-1.4	0.23182764(37)	0.00016	1.26408(32)	-0.0045				
12^00	1428.20766(56)	-1.2	0.23570200(59)	0.00019	1.14981(92)	-0.0493				
12^01	2960.06963(46)	-4.2	0.23332612(50)	0.00018	1.16047(72)	-0.0470				
04^01	2799.09736(53)	-3.5	0.23597627(50)	0.00019	1.45526(60)	-0.0348				
10^00	769.09433(21)	-0.6	0.23513871(34)	0.00022	0.83631(29)	-0.0196				
10^01	2312.36587(17)	-3.5	0.23265773(34)	0.00020	0.82993(30)	-0.0210				
20^01	3089.06939(36)	-3.8	0.23347313(42)	0.00021	0.67461(45)	-0.0052				
01^10	342.61453(34)	0.2	0.23623885(31)	0.00021	1.05599(19)	-0.0077	-3.8732(20)	0.0095	0.903(28)	-0.56
01^11	1890.44444(35)	-2.6	0.23381085(31)	0.00020	1.04844(19)	-0.0081	-3.8013(20)	0.0100	0.969(28)	-0.60
01^12	3420.84793(55)	-5.6	0.23140746(95)	0.00018	1.0077(38)	-0.0400	-3.7269(30)	0.0147	…	…
03^10	969.54450(45)	-0.2	0.23770372(35)	0.00021	1.26742(26)	-0.0130	-6.4366(28)	0.0059	5.533(38)	-0.44
03^11	2505.04752(41)	-3.1	0.23534237(34)	0.00020	1.26294(26)	-0.0119	-6.3709(26)	0.0042	5.601(38)	-0.47
11^10	1138.00398(22)	-0.5	0.23642646(33)	0.00022	0.93207(27)	-0.0133	-5.3166(17)	-0.0072	-2.261(37)	-0.53
11^11	2673.78563(29)	-3.5	0.23397640(32)	0.00020	0.92315(23)	-0.0143	-5.1351(19)	-0.0012	-2.084(34)	-0.65
21^11	3472.65828(31)	-4.4	0.23453944(38)	0.00020	0.81620(44)	-0.0080	-7.0698(31)	-0.0246	-4.510(66)	-0.17
02^20[a]	*c*	…	0.2374892(11)	0.00022	1.09750(54)	-0.0058	…	…	-2.868(50)	-0.83
02^21	*c*+1540.63644(13)	*-2.9*	0.2350794(11)	0.00020	1.08890(53)	0.0006	…	…	-2.770(50)	-0.67
02^22	*c*+3063.95627(31)	*-6.0*	0.2326986(11)	0.00019	1.09476(80)	0.0048	…	…	…	…
03^30[b]	*d*	…	0.2387284(11)	0.00022	1.15308(62)	-0.0021	…	…	…	…
03^31	*d*+1533.46539(14)	*-3.0*	0.2363385(11)	0.00021	1.14600(63)	0.0008	…	…	…	…

[a] The $02^21 - 02^20$ and $02^22 - 02^21$ bands were fitted separately, and the value of *c* was not experimentally determined. The theoretical value for *c* was 686.4 cm^{-1}.

[b] The $03^31 - 03^30$ band was fitted separately, and the value of *d* was not experimentally determined. The theoretical value for *d* was 1031.9 cm^{-1}.

Twenty two vibrational bands were assigned and twenty vibrational levels are connected with each other and with the ground state (Figure 7.3). These twenty levels allowed the equilibrium constants ω_i, x_{ij}, B_e, and α_i for BeF_2 to be determined. The ν_1 and ν_2 fundamental bands were determined to be 769.09433(21) and 342.61453(34) cm^{-1}, respectively (Table 7.1). Two times the ν_2 value is 685 cm^{-1}, which is close to the ν_1 value of 769 cm^{-1}. Both the $02^00(\Sigma_g)$ and $10^00(\Sigma_g)$ vibrational levels will interact with each other. This type of interaction is called a Fermi resonance [58], and the analysis must take this effect into account to obtain accurate constants. The same nonlinear least-squares fitting procedure as used by Cheng *et al*. [61] and Blanquet *et al*. [62] to treat CS_2 was used. This procedure is based on the method introduced by Pliva [63]. The vibrational ($J = 0$) term values and B rotational constants were fitted with effective Hamiltonians. The effective Hamiltonians take the Fermi resonance into account to give the deperturbed equilibrium constants.

Without Fermi resonance, the vibrational term values are given by the expression:

$$G(\mathrm{v}_1, \mathrm{v}_2^l, \mathrm{v}_3) = \sum_i \omega_i (\mathrm{v}_i + \tfrac{1}{2} d_i) + \sum_{i \le j} x_{ij} (\mathrm{v}_i + \tfrac{1}{2} d_i)(\mathrm{v}_j + \tfrac{1}{2} d_j) + g_{22} l^2 , \tag{7.2}$$

in which d_i is the degeneracy of the ith vibrational mode. These term values form the diagonal elements of the vibrational Hamiltonian matrix. The Fermi resonance shifts both the vibrational and rotational levels, and therefore adds off-diagonal terms which depend on the vibrational and rotational quantum numbers. The off-diagonal terms added to the vibrational ($J = 0$) Hamiltonian matrix are [61–63]:

$$\begin{aligned} W_{122} &= \langle \mathrm{v}_1, \mathrm{v}_2, l, \mathrm{v}_3, J = 0 \left| \hat{H} \right| \mathrm{v}_1 - 1, \mathrm{v}_2 + 2, l, \mathrm{v}_3, J = 0 \rangle \\ &= \frac{1}{2} \left\{ \mathrm{v}_1 \left[(\mathrm{v}_2 + 2)^2 - l^2 \right] \right\}^{1/2} \\ &\quad \times \left\{ \frac{-k_{122}}{\sqrt{2}} + \lambda_1 \mathrm{v}_1 + \lambda_2 (\mathrm{v}_2 + 2) + \lambda_3 \left(\mathrm{v}_3 + \frac{1}{2} \right) - \delta \times l^2 \right\} \end{aligned} \tag{7.3}$$

where the λ's are the higher-order vibrational corrections, and the constant δ is a vibration-rotation correction. The diagonalization of the vibrational Hamiltonian gives the vibrational energies. The extent of mixing of the vibrational levels is given by the eigenvectors of the vibrational matrix.

The Fermi resonance also changes the B rotational constants. The perturbed B_k values are given in terms of the deperturbed equilibrium constants as [61– 63]

$$B_k = \sum_{i,j} V_{ik} V_{jk} F_{ij} \tag{7.4}$$

where

$$F_{ii} = B_i^0 = B_e - \alpha_1 (\mathrm{v}_1 + \tfrac{1}{2}) - \alpha_2 (\mathrm{v}_2 + 1) - \alpha_3 (\mathrm{v}_3 + \tfrac{1}{2}) , \tag{7.5}$$

$$F_{ij} = \frac{1}{2} \delta (\mathrm{v}_1)^{1/2} \left[(\mathrm{v}_2 + 2)^2 - l^2 \right]^{1/2} , \tag{7.6}$$

and V_{ik} are the eigenvector components from the diagonalization of the vibrational Hamiltonian, with the assumption that the rotational effects are assumed to be too small (i.e., δ is a small correction) to change the eigenvector matrix, **V**. Therefore the observed *B* rotational constants can be fitted simultaneously with the vibrational (*J*=0) energy levels to give the equilibrium vibrational and rotational constants in Eqs. (7.2), (7.3), (7.5) and (7.6). This procedure avoids having to work with the complete set of vibration-rotation energy levels.

Not all the parameters of Eqs. (7.2), (7.3), (7.5) and (7.6) are independent, and a redundancy relationship between x_{22} and x_{ll} ($x_{ll} = g_{22} + B_0$ was fitted instead of g_{22} in the program) has been given by Amat and Pimbert [64] as

$$x_{22} + 3x_{ll} + \frac{(k_{122})^2}{2}\left[\frac{1}{\omega_1} - \frac{1}{2(2\omega_2 + \omega_1)}\right] = 0 \quad . \tag{7.7}$$

The dependence of the parameters can be removed by using the redundancy relation, Eq. (7.7). The redundancy condition is treated as a data point whose expected value is zero and fitted simultaneously with the observed vibrational energy levels and *B* rotational constants.

Since the least-squares fit is nonlinear, the initial values of the parameters have to be close to their true values. The Fermi resonance in BeF_2 is very strong, and it is not possible to obtain these initial values by hand calculation. These initial values were taken from the second-order perturbation theory calculation by J. Koput [2], and are listed in Table 7.2 for comparison. The equilibrium constants obtained from the experiment are given in Table 7.2, and the output file of the fit has been published in the supplementary Table of Ref. [2]. Note that the $02^02(\Sigma_g)$ state could not be fitted together with the other states, and it was not included. The predicted term value of 3713.1 cm^{-1} for the $02^02(\Sigma_g)$ level is about 5 cm^{-1} smaller than the observed value, 3717.80000(34) cm^{-1}. One possible reason for this discrepancy is that the $02^02(\Sigma_g)$ state is perturbed by the nearby $42^00(\Sigma_g)$ and/or $50^00(\Sigma_g)$ and/or other states, which were not considered in the fit.

The experimental value of the Fermi resonance constant, k_{122} = 90.202 cm^{-1}, is close to the value of ~80 cm^{-1} for the isoelectronic molecule CO_2 [65], and larger than the value of ~40 cm^{-1} for CS_2 [61]. The constant g_{22} is -2.660 cm^{-1}, which means that for the vibrational states with the same vibrational quantum numbers, as the vibrational angular momentum quantum number *l* increases, the states go to lower energy if the Fermi resonance is neglected. However, the $02^00(\Sigma_g)$, $02^01(\Sigma_u)$, $02^02(\Sigma_g)$, $03^10(\Pi_u)$ and $03^11(\Pi_g)$ states are pushed down by the Fermi resonance, and finally, the $02^20(\Delta_g)$, $02^21(\Delta_u)$, $02^22(\Delta_g)$ states lie about 40 cm^{-1} higher than the $02^00(\Sigma_g)$, $02^01(\Sigma_u)$, $02^02(\Sigma_g)$ states, respectively, and the $03^30(\Phi_u)$ and $03^31(\Phi_g)$ states lie about 60 cm^{-1} higher than the $03^10(\Pi_u)$ and $03^11(\Pi_g)$ states, respectively (from the variational calculation; see Table 7.1). The equilibrium rotational constant (B_e) from this fit was used to determine the equilibrium beryllium fluorine distance (r_e) from the moment of inertia equation [Eq.(1.30)], and a value of 1.37298(12) Å (Table 7.2) was obtained.

The present analysis of BeF_2 spectra has confirmed the previous tentative assignment of the $\nu_1+\nu_2$ combination band [1]. The experimental values of ν_1 and ω_1 obtained from the present study are 769.09433(21), and 731.853(52) cm^{-1}, respectively (Tables 7.1 and 7.2), and ν_1 was estimated to lie between 780 and 890 cm^{-1} in the previous paper [1]. (Note that ν_1 is the observed fundamental

vibrational frequency while ω_1 is the estimated harmonic frequency with the effects of Fermi resonance removed.) However, this assignment was disputed by Lee and Wright [57] based on their harmonic calculations which obtained ω_1=720±10 cm^{-1}, in good agreement with the present experimental value of 731.853(52) cm^{-1}. However, their calculations neglected the strong Fermi resonance between the ν_1 and $2\nu_2$ vibrational levels which shifts the ν_1 vibrational frequency by about 40 cm^{-1}. So their conclusion about the value of ν_1 and assignment of the $\nu_1+\nu_2$ band were incorrect.

Table 7.2 Spectroscopic constant (cm^{-1}) for BeF_2.

Constant	Perturbation calculation[a]	Experiment
ω_1	732.34	731.853(52)
ω_2	341.00	342.075(19)
ω_3	1587.87	1584.716(24)
x_{11}	-1.331	-1.636(16)
x_{12}	-6.155	-5.328(75)
x_{22}	1.309	3.149(21)
x_{13}	-10.197	-10.079(13)
x_{23}	-7.336	-7.1708(54)
x_{33}	-8.990	-8.7408(67)
g_{22}	-2.838	-2.660(19)[b]
k_{122}	91.15	90.202(44)
λ_1	…	0.986(17)
λ_2	…	1.093(11)
λ_3	…	-0.0531(59)
B_e	0.235105	0.235354(41)
α_1	0.000728	0.000803(25)
α_2	-0.001289	-0.001247(11)
α_3	0.002480	0.002424(16)
δ	…	0.0004337(84)
$\nu_1(\sigma_g)$	766.1	769.09433(21)
$\nu_2(\pi_u)$	335.3	342.61543(34)
$\nu_3(\sigma_u)$	1557.5	1555.04795(11)
r_e	1.374	1.37298(12)

[a] In the calculation by Koput, the Fermi resonance constants λ_1, λ_2, λ_3 and δ were not calculated in the perturbation approach.
[b] Calculated from $g_{22} = x_{ll} - B_0$ (x_{ll} = -2.425(19) cm^{-1} from the fit).

7.4 Conclusions

The high-resolution infrared emission spectrum of BeF_2 vapor at 1000°C was rotationally analyzed. The ν_3 fundamental band, the $\nu_1+\nu_2$, $\nu_1+\nu_3$ and $2\nu_2+\nu_3$ combination bands, and eighteen hot bands were assigned. The symmetric stretching (ν_1), bending (ν_2), and antisymmetric streching (ν_3) mode frequencies were determined to be 769.0943(2), 342.6145(3) and 1555.0480(1) cm^{-1}, respectively, from the band origins of the ν_3, $\nu_1+\nu_3$ and $\nu_1+\nu_2$ bands. The observed vibrational term values and B rotational constants were fitted simultaneously to an effective Hamiltonian model with Fermi resonance taken into account, and deperturbed equilibrium vibrational and rotational constants were obtained for BeF_2. The equilibrium rotational constant (B_e) was determined to be 0.235354(41) cm^{-1}, and the associated equilibrium bond distance (r_e) is 1.3730(1) Å. As in the isoelectronic CO_2 molecule, the Fermi resonance in BeF_2 is very strong, and the interaction constant k_{122} was found to be 90.20(4) cm^{-1}.

7.5 References

[1] C.I. Frum, R. Engleman, Jr., and P.F. Bernath, J. Chem. Phys. **95**, 1435 (1991).

[2] S. Yu, A. Shayesteh and P.F. Bernath, J. Chem. Phys. **123**, 134303 (2005).

[3] M. Hargittai, Chem. Rev. **100**, 2233 (2000).

[4] I. R. Beattie, Angew. Chem. Int. Ed. **38**, 3294 (1999).

[5] V. P. Spiridonov, N. Vogt, and J. Vogt, Struc. Chem. **12**, 349 (2001).

[6] S.H. Ashworth, P.J. Hodges, and J.M. Brown, Phys. Chem. Chem. Phys. **4**, 5923 (2002).

[7] S.H. Ashworth and J.M. Brown, J. Mol. Spectrosc. **191**, 276 (1998).

[8] G. van den Hoek and J.M. Brown, J. Mol. Spectrosc. **182**, 163 (1997).

[9] E. Bosch, P. Crozet, A.J. Ross, and J.M. Brown, J. Mol. Spectrosc. **202**, 253 (2000).

[10] P.A. Akishin and V.P. Spiridonov, Kristallografiya **2**, 475 (1957).

[11] P.A. Akishin, V.P. Spiridonov, and G.A. Sobolev, Dokl. Akad. Nauk. SSSR **118**, 1134 (1958).

[12] L. Wharton, R.A. Berg, and W. Klemperer, J. Chem. Phys. **39**, 2023 (1963).

[13] A. Büchler, J.L. Stauffer, and W. Klemperer, J. Am. Chem. Soc. **86**, 4544 (1964).

[14] A. Büchler, J.L. Stauffer, and W. Klemperer, J. Chem. Phys. **40**, 3471 (1964).

[15] M. Hargittai, Coord. Chem. Rev. **91**, 35 (1988).

[16] A. Snelson, J. Phys. Chem. **70**, 3208 (1966).

[17] D.E. Mann, G.V. Calder, K.S. Seshadri, D. White, and M.J. Linevsky, J. Chem. Phys. **46**, 1138 (1967).

[18] V. Calder, D.E. Mann, K.S. Seshadri, M. Linevsky, and D. White, J. Chem. Phys. **51**, 2093 (1969).

[19] D. White, G.V. Calder, S. Hemple, and D.E. Mann, J. Chem. Phys. **59**, 6645 (1973).

[20] R.H. Hague, J.L. Margrave, and A.S. Kana'an, J. Chem. Soc. Faraday Trans. 2 **71**, 1082 (1975).

[21] M.L. Lesiecki and J.W. Nibler, J. Chem. Phys. **64**, 871 (1976).

[22] F. Ramondo, V. Rossi, and L. Bencivenni, Mol. Phys. **64**, 513 (1988).

[23] E.F. Hayes, J. Phys. Chem. **70**, 3740 (1966).

[24] J.L. Gole, A.K.Q. Siu, and E.F. Hayes, J. Chem. Phys. **58**, 857 (1973).

[25] C.A. Coulson, Isr. J. Chem. **11**, 683 (1973).

[26] N.M. Kilmenko, D.G. Musaev, and O.P. Charkin, Russ. J. Inorg. Chem. **29**, 639 (1984).

[27] U. Salzner and P. von R. Schleyer, Chem. Phys. Lett. **172**, 461 (1990).

[28] D.M. Hassett and C.J. Marsden, Chem. Comm. 667 (1990).

[29] L. Seijo, Z. Barandiarán, and S. Huzinaga, J. Chem. Phys. **94**, 3762 (1991).

[30] T.G. Wright, E.P.F. Lee, and J.M. Dyke, Mol. Phys. **73**, 941 (1991).

[31] M. Kaupp and P.v.R. Schleyer, J. Am. Chem. Soc. **114**, 491 (1992).

[32] D.M. Hasset and C.J. Marsden, J. Mol. Struct. **346**, 249 (1995).

[33] D. Cubiciotti, J. Phys. Chem. **65**, 1058 (1961).

[34] T.E. Brackett and E.B. Brackett, J. Phys. Chem. **66**, 1542 (1962).

[35] A. Büchler, W. Klemperer, and A.G. Emslie, J. Chem. Phys. **36**, 2499 (1962).

[36] I. Eliezer, Theor. Chim. Acta **18**, 77 (1970).

[37] I. Eliezer and A. Reger, Theor. Chim. Acta **26**, 283 (1972).

[38] Y.S. Kim and R.G. Gordon, J. Chem. Phys. **60**, 4332 (1974).

[39] M. Guido and G. Gigli, J. Chem. Phys. **65**, 1397 (1976).

[40] M. Guido and G. Gigli, J. Chem. Phys. **66**, 3920 (1977).

[41] D.L. Hildenbrand, J. Electrochem. Soc. **126**, 1396 (1979).

[42] M Spoliti, G. DeMaria, L. D'Alessio, and M. Maltese, J. Mol. Struct. **67**, 159 (1980).

[43] G. Galli and M. P. Tosi, I1 Nuovo Cimento **4D**, 413 (1984).

[44] W. Andreoni, G. Galli, and M. Tosi, Phys. Rev. Lett. **55**, 1734 (1985).

[45] I. Bytheway, R.J. Gillespie, T.-H. Tang, and R.F.W. Bader, Inorg. Chem. **34**, 2407 (1995).

[46] K.J. Donald and W.H. Mulder, and L.V. Szentpály, J. Chem. Phys. **119**, 5423 (2003).

[47] M. Kaupp, Angew. Chem. Int. Ed. **40**, 3534 (2001).

[48] R.L. De Kock, M.A. Peterson, L.K. Timmer, E.J. Baerends, and P. Vernooijs, Polyhedron **9**,1919 (1990).

[49] L. von Szentpaly and P. Schwerdtfeger, Chem. Phys. Lett. **170**, 555 (1990).

[50] M. Kaupp, P.v.R. Schleyer, H. Stoll, and H. Preuss, J. Am. Chem. Soc. **113**, 6012 (1991).

[51] L. von Szentály, J. Phys. Chem. A **106**, 11945 (2002).

[52] A. Büchler and W. Klemperer, J. Chem. Phys. **29**, 121 (1958).

[53] N. Vogt, G.V. Girichev, J. Vogt, and A.G. Girichev, J. Mol. Struct. **352/353**, 175 (1995).

[54] J.M. Dyke and G. Wright, Chem. Phys. Lett. **169**, 138 (1990).

[55] F. Ramondo, L. Bencivenni, and M. Spoliti, J. Mol. Struct. (THEOCHEM) **277**, 171 (1992).

[56] T.P. Pogrebnaya, V.V. Sliznev, and V.G. Solomonik, Koord. Khim. **23**, 498 (1997).

[57] E.P.F. Lee and T.G. Wright, J. Phys. Chem. A **104**, 974 (2000).

[58] P.F. Bernath, *Spectra of Atoms and Molecules*, 2nd ed., Oxford University Press, New York (2005).

[59] M. Carleer, "Wspectra: a Windows program to measure accurately the line intensities of highesolution Fourier Transform spectra", In: Russel JE, "Remote sensing of clouds and the atmosphere, EOS/SPIE. Proceedings series", **4168**, 337 (2001).

[60] F.W. Loomis and R.W. Wood, Phys. Rev. **32** 223 (1928).

[61] C.-L. C. Cheng, J.L. Hardwick, and T.R. Dyke, J. Mol. Spectrosc. **179**, 205 (1996).

[62] G. Blanquet, E. Baeten, I. Cauuet, J. Walrand, and C.P. Courtoy, J. Mol. Spectrosc. **112**, 55 (1985).

[63] J. Pliva, J. Mol. Spectrosc. **27**, 461 (1968).

[64] G. Amat and M. Pimbert, J. Mol. Spectrosc. **16**, 278 (1965).

[65] S.A. Tashkun, V.I. Perevalov, J.-L. Teffo, L.S. Rothman, and V.G. Tyuterev, J. Quant. Spectrosc. Radiat. Transfer **60**, 785 (1998).

Chapter 8

Fourier transform near-infrared emission spectroscopy of CoS

8.1 Introduction

The electronic spectra of 3*d* transition metal oxides and sulfides are generally very complex. The metal atom often has many unpaired electrons that can produce a huge number of low-lying electronic states with high values of spin multiplicity and orbital angular momentum, as well as large spin-orbit interactions. These electronic states may perturb one other, thereby complicating their spectra and making analysis difficult. Theoretical calculations are plagued with similar problems, and it is hard to predict the energy order and properties of the low-lying electronic states. Despite these difficulties, most of the 3*d* transition metal monoxides have been well studied partly due to their importance in astrophysics, and as models in understanding the chemical bonding in simple metal systems [1]. In contrast, little data is available for the corresponding sulfides [2,3].

Theoretical calculations and isovalent arguments suggest that CoS has a similar ordering of electronic states as CoO [3,4]. The ground state of CoO has been established as $^4\Delta_i$ with an electron configuration of $\sigma^2\delta^3\pi^2$ by experiments [5–10] as well as theoretical calculations [3,11–14]. Three $^4\Delta$ states and two $^4\Phi$ states of CoO [8] have been identified by visible Doppler-limited intracavity spectroscopy and jet-cooling methods. A $^4\Pi_i - X\,^4\Delta_i$ transition of CoO has been observed in the near infrared region by high-resolution Fourier transform spectroscopy [7], and it was suggested that a $^4\Sigma^-$ state should lie nearby because of the large Ω-doubling observed on some of the spin components of this $^4\Pi_i$ state. Four transitions have been reported in the near infrared region for matrix-isolated CoO: one was assigned to the 0-0 band of the $^4\Pi_{5/2} - X\,^4\Delta_{7/2}$ sub-band, and three others were assigned tentatively to transitions involving $^4\Sigma^-$, $^6\Delta$ and $^2\Delta$ states, in the absence of gas-phase data [15]. Dolg *et al*. [11] predicted that the first excited state of CoO is a $^4\Sigma^-$ state, and that it lies 0.5 eV (4032 cm^{-1}) above the $X\,^4\Delta_i$ ground state. Gutsev *et al*. [12] predicted that this $^4\Sigma^-$ excited state lies just 0.11 eV (887 cm^{-1}) above the $X\,^4\Delta_i$ ground state. Using the B1LYP exchanged-correlation functional, Uzunova *et al*. [13] calculated the properties of several excited states lying within 1 eV of the ground state, and predicted low-lying $^4\Sigma^-$, $^6\Delta$ and $^2\Delta$ states for CoO, but failed to predict low-lying $^4\Pi$ or $^4\Phi$ states. Using DFT and TDDFT methods, Dai *et al*. [14] predicted many low-lying excited states for CoO, such as $^4\Sigma^-$, $^4\Pi$, $^4\Phi$, $^4\Delta$, $^2\Pi$, $^2\Delta$, etc., but this paper does not provide unambiguous electronic assignments for most of these low-lying states. All of the above calculations predict a low-lying $^4\Sigma^-$ state with an internuclear distance shorter than that of the $X\,^4\Delta$ ground state.

The number of spectroscopic studies on CoS, however, is limited. An early *ab initio* calculation by Anderson *et al*. [16] predicted a $X\,^4\Sigma^-$ ground state, while later theoretical calculations by Bauschlicher *et al*. [3] and Bridgeman *et al*. [4] predicted a $X\,^4\Delta$ ground state. The only available experimental study on CoS is the microwave study by Flory *et al*. [2], in which the ground state of CoS was established as $^4\Delta_i$ with a $\sigma^2\delta^3\pi^2$ electron configuration.

This chapter reports on the first observation of two electronic transitions of CoS in the 3200 – 6000 cm^{-1} region, which have been assigned as the $A\,^4\Phi_i - X\,^4\Delta_i$ and $B\,^4\Pi_i - X\,^4\Delta_i$ transitions. A rotational

analysis of the 0 – 0 bands for all four sub-bands of the $A\ ^4\Phi_i - X\ ^4\Delta_i$ transition, and the 0 – 0, 0 – 1, 1 – 0 and 1 – 1 bands for the 5/2 – 7/2 sub-band of the $B\ ^4\Pi_i - X\ ^4\Delta_i$ transition is described and discussed. The results presented in this chapter have been published in Ref. [17].

8.2 Experimental details

Gas-phase CoS was produced by the reaction of cobalt vapor and CS_2 vapor. Cobalt vapor was obtained by heating cobalt metal to about 3000 K in a carbon tube furnace (King furnace), which has been described in Section 2.1.2. A mixture of ~150 Torr He and ~ 30 mTorr CS_2 vapor was present in the furnace. The emission from CoS was focused using a CaF_2 lens into the entrance aperture of a Bruker IFS 120 HR Fourier transform spectrometer.

The near-infrared spectrum of CoS was measured at a resolution of 0.04 cm^{-1} in the 1800–8000 cm^{-1} region using a CaF_2 beamsplitter and a liquid nitrogen-cooled InSb detector, with a total recording time of about one hour (80 scans). The spectrum also contained strong emission lines from impurities (CO, HF and HCl), which were used for calibration. The accuracy of the CoS line positions is estimated to be approximately 0.005 cm^{-1}.

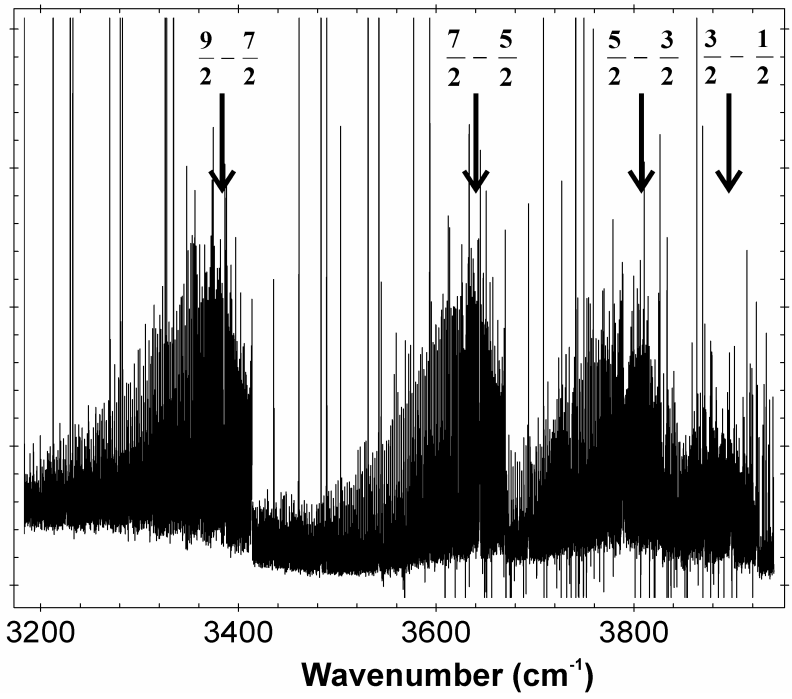

Figure 8.1 An overview of the 0 – 0 band of the $A\ ^4\Phi_i - X\ ^4\Delta_i$ transition in CoS recorded at a resolution of 0.04 cm^{-1}. Four unevenly-spaced sub-bands with strong *R* heads are labeled and arise from the $\frac{9}{2}-\frac{7}{2}$, $\frac{7}{2}-\frac{5}{2}$, $\frac{5}{2}-\frac{3}{2}$ and $\frac{3}{2}-\frac{1}{2}$ sub-bands. Perturbations were observed in the $\frac{5}{2}-\frac{3}{2}$ sub-band (see text). The strong emission lines are from the impurity HF.

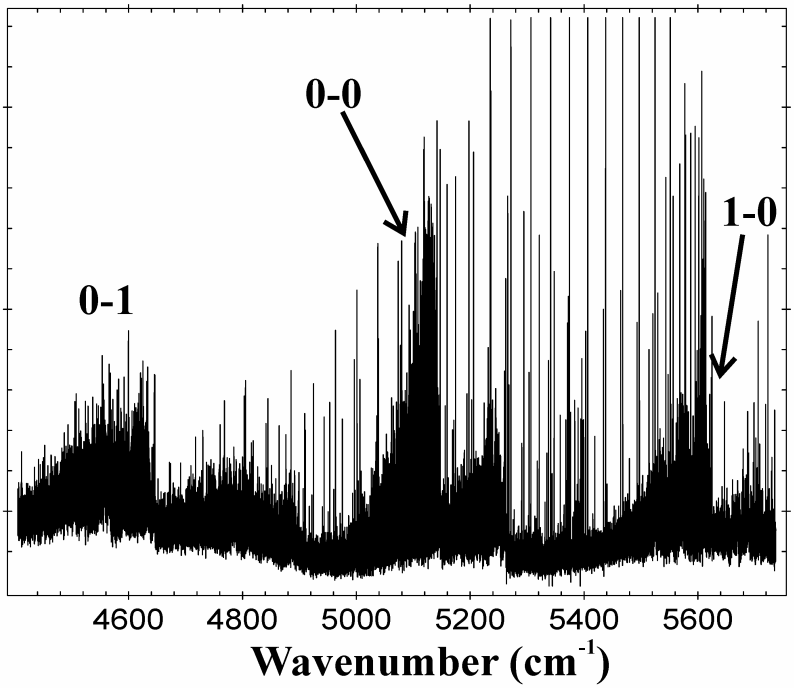

Figure 8.2 An overview of the $B\ ^4\Pi_i - X\ ^4\Delta_i$ transition of CoS recorded at a resolution of 0.04 cm^{-1}. The 0 – 0, 0 – 1, and 1 – 0 bands of the $^4\Pi_{5/2} - X\ ^4\Delta_{7/2}$ sub-band are labeled. The 1 – 1 band was also identified, but not shown in this figure. Additional weak bands are present in this region, and probably arise from other sub-bands of the $B\ ^4\Pi_i - X\ ^4\Delta_i$ transition. However, these bands could not be assigned due to their weak intensity. The spectrum also contained strong emission lines from the impurity HF, which were used for calibration.

8.3 Results and discussion

The program WSPECTRA, written by M. Carleer [18], was used to determine the line positions, and a color Loomis-Wood program [19] was used to pick out the branches. The CoS bands assigned to the $A\ ^4\Phi_i - X\ ^4\Delta_i$ transition were observed in the 3200 – 4000 cm^{-1} spectral region as shown in Figure 8.1. A $^4\Phi_i - {}^4\Delta_i$ transition should consist of four sub-bands: $^4\Phi_{9/2} - {}^4\Delta_{7/2}$, $^4\Phi_{7/2} - {}^4\Delta_{5/2}$, $^4\Phi_{5/2} - {}^4\Delta_{3/2}$, and $^4\Phi_{3/2} - {}^4\Delta_{1/2}$. For Hund's case (a) states, these four sub-bands should be separated by the difference between the spin-orbit separations of the upper and lower states. Four unevenly-spaced bands with *R* heads near 5624, 5147, 4634, and 3925 cm^{-1} were observed in the experiments (Figure 8.1), and the lower states of these bands were confirmed to be the v = 0 levels of the four spin components of the $X\ ^4\Delta_i$ ground state using lower-state combination differences from the microwave study [2]. The three strongest sub-bands show clear single *P*, *Q* and *R* branches, while the weakest sub-band shows two *P*, two *Q*, and two *R* branches. The *Q* branch is much stronger than the *P* and *R* branches in each of these sub-bands, indicating that these sub-bands are perpendicular transitions ($\Delta\Omega = \pm 1$) arising from either

a $^4\Phi_i - {}^4\Delta_i$ transition or a $^4\Pi_i - {}^4\Delta_i$ transition. As the Ω-doubling splitting is small and present only in one of the four sub-bands, these observations are assigned to the four sub-bands of the 0-0 band of a $^4\Phi_i - {}^4\Delta_i$ transition. It is interesting to note that this low-lying $^4\Phi_i$ state has not yet been assigned in the isovalent CoO molecule [7,8,15].

Three additional bands, with *R* heads near 5147, 5624, and 4634 cm^{-1}, are also observed for CoS, and are shown in Figure 8.2. These features were assigned as the 0 – 0, 1 – 0 and 0 – 1 bands of the $\frac{5}{2} - \frac{7}{2}$ sub-band of the $B\ ^4\Pi_i - X\ ^4\Delta_i$ transition. Rotational assignments were made using lower state combination differences. The 1 – 1 band was then predicted and identified in the spectrum. Figure 8.3 shows an expanded view of the 0 – 0 band. The other two vibrational sub-bands have similar structure. The spectrum is very dense and lines from different branches overlap with each other. The Ω-doubling splitting in these bands begins to be resolved at $J \approx 60$. Weak bands with *R* heads near 4645, 4646, 4891, 4899, 5260, and 5262 cm^{-1}, as shown in Figure 8.2, could not be rotationally assigned because of their relatively weak intensity. Some of these bands probably arise from the $\frac{3}{2} - \frac{5}{2}$, $\frac{1}{2} - \frac{3}{2}$ and $(-\frac{1}{2}) - \frac{1}{2}$ sub-bands of the $B\ ^4\Pi_i - X\ ^4\Delta_i$ transition. The analogous low-lying $^4\Pi_i$ state has been observed in CoO [7,8,15].

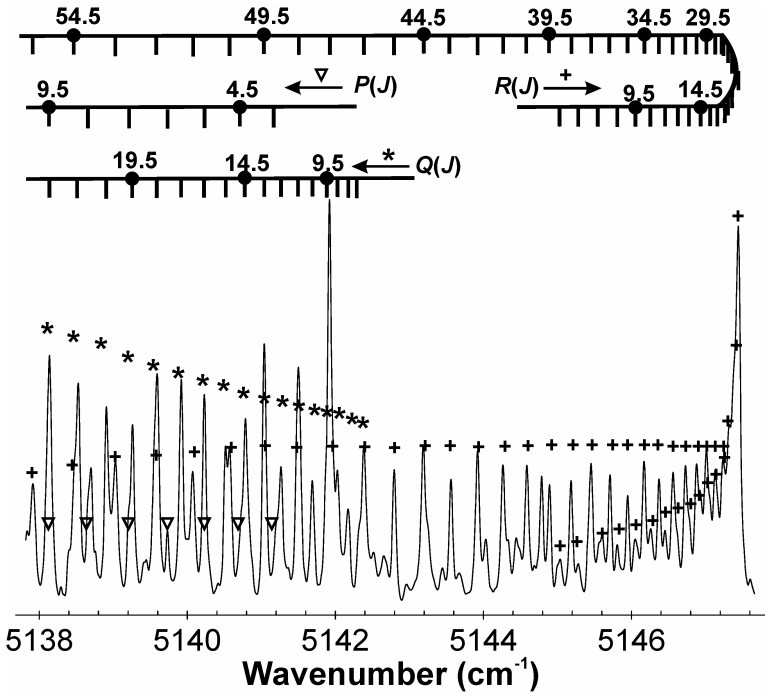

Figure 8.3 An expanded view of the 0 – 0 band of the $B\ ^4\Pi_{5/2} - X\ ^4\Delta_{7/2}$ sub-band of CoS. A strong *R* branch head is present. Rotational assignments are shown above the spectrum. The spectrum is very dense, and lines from different branches overlap with each other. The Ω-doubling, which is resolved starting at $J \approx 60$, is not shown

For data analysis, Hund's case (c) fits were first performed for the observed bands. The usual empirical energy level expression was used for each of the spin components of the $X\,^4\Delta_i$, $A\,^4\Phi_i$, and $B\,^4\Pi_i$ states (Chapter 1):

$$F(J) = T_v + B_v J(J+1) - D_v[J(J+1)]^2 \pm \tfrac{1}{2}[p_v(J+1/2) + p_{Dv}(J+1/2)^3 + p_{Hv}(J+1/2)^5 + p_{Lv}(J+1/2)^7], \quad (8.1)$$

in which the upper (lower) sign refers to *e* (*f*) parity, and p_v, p_{Dv} , p_{Hv} and p_{Lv} are Ω-doubling constants. The *e*- and *f*-parity assignments were arbitrarily chosen for bands with resolved Ω-doubling. The Hund's case (c) spectroscopic constants obtained for CoS are provided in Table 8.1. Lines from the 0 – 0, 1 – 1, 0 – 1, and 1 – 0 bands of the $B\,^4\Pi_{5/2} - X\,^4\Delta_{7/2}$ sub-band, and the 0 – 0 band of the $A\,^4\Phi_{9/2} - X\,^4\Delta_{7/2}$ sub-band were fitted together because they are all connected. The 0 – 0 bands of the $\frac{7}{2}-\frac{5}{2}$, $\frac{5}{2}-\frac{3}{2}$ and $\frac{3}{2}-\frac{1}{2}$ sub-bands of the $A\,^4\Phi_i - X\,^4\Delta_i$ transition were fitted separately An estimated uncertainty of 0.005 cm^{-1} was used for most lines, and an uncertainty of 0.05 cm^{-1} was used for blended lines near band origins and band heads. The hyperfine-free pure rotational line positions in the four spin components of the $X\,^4\Delta_i$ state (extracted using the data published in Ref. [2]) were also included in the fits. The output files of the fits (including complete lists of all data) have been published in the supplementary tables of Ref. [17].

For the $^4\Phi_{9/2} - {}^4\Delta_{7/2}$ and $^4\Phi_{7/2} - {}^4\Delta_{5/2}$ sub-bands, lines with J'' up to 160 were assigned, and for the $^4\Phi_{3/2} - {}^4\Delta_{1/2}$ sub-band which has resolved Ω-doubling, lines with J'' up to 80 were assigned. However, strong perturbations were observed in the 0 – 0 band of the $^4\Phi_{5/2} - {}^4\Delta_{3/2}$ sub-band. As a result, only lines with $J'' < 60$ could be assigned, and lines with $J'' > 40$ were deweighted in order to obtain a successful fit. In addition, there are many strong lines observed in the region in which the $A\,^4\Phi_{5/2} - X\,^4\Delta_{3/2}$ sub-band high *J* lines are expected (Figure 8.1), but could not be assigned. Due to the perturbations, a relatively large value was obtained for the D_0 centrifugal constant (1.845×10^{-7} cm^{-1}) for the $A\,^4\Phi_{5/2}$ spin component (Table 8.1), as compared to those for the other spin components of the $A\,^4\Phi_i$ state . Based only on the observations in this experiment, the source of these perturbations could not be identified.

As given in Table 8.1, the 0 – 0, 1 – 1, 0 – 1, and 1 – 0 bands of the $B\,^4\Pi_{5/2} - X\,^4\Delta_{7/2}$ sub-band required p_H and p_L Ω-doubling constants for the $B\,^4\Pi_{5/2}$ spin component. The Ω-doubling splitting increases as $\sim J^5$, and is present entirely in the $B\,^4\Pi_{5/2}$ spin component. In the fit for the 0-0 band of the $A\,^4\Phi_{3/2} - X\,^4\Delta_{1/2}$ sub-band, only *p* and p_D were needed for the $X\,^4\Delta_{1/2}$ spin component, where the Ω-doubling splitting increases linearly with *J*. The spectroscopic constants in Table 8.1 provide vibrational intervals $\Delta G_{1/2}$ = 514.55244(31) cm^{-1} for the $X\,^4\Delta_{7/2}$ spin component, and $\Delta G_{1/2}$ = 476.82124 (44) cm^{-1} for the $B\,^4\Pi_{5/2}$ spin component. Equilibrium constants B_e =0.20773952 (23) cm^{-1}, α_e = 0.00010672 (23) cm^{-1}, r_e = 1.9786450 (11) Å were determined for the $X\,^4\Delta_{7/2}$ spin component, while B_e = 0.19903465 (81) cm^{-1}, α_e = 0.00104902 (81) cm^{-1}, r_e = 2.0214505 (39) Å were obtained for the $B\,^4\Pi_{5/2}$ spin component.

Table 8.1 Hund's case (c) constants (in cm^{-1}) for the $X\ ^4\Delta_i$, $A\ ^4\Phi_i$, and $B\ ^4\Pi_i$ states of CoS (all uncertainties are 1σ).

State	T_v	B_v	$D_v/10^{-7}$	$p_v/10^{-3}$	$p_{Dv}/10^{-9}$	$p_{Hv}/10^{-10}$	$p_{Lv}/10^{-13}$
$X\ ^4\Delta_{7/2}$, v=0	0	0.207205911(46)	1.33499(15)				
$X\ ^4\Delta_{7/2}$, v=1	514.55244(31)	0.20613870(23)	1.33990(79)				
$A\ ^4\Phi_{9/2}$, v=0	3408.92170(51)	0.19911315(11)	1.31204(16)				
$B\ ^4\Pi_{5/2}$, v=0	5142.73509(43)	0.19851015(39)	1.23015(68)	…	…	0.476(28)	-0.2141(52)
$B\ ^4\Pi_{5/2}$, v=1	5619.55633(45)	0.19746112(71)	1.1925(23)	…	…	2.31(12)	-1.478(41)
$X\ ^4\Delta_{5/2}$, v=0	0	0.207666544(41)	1.35157(15)				
$A\ ^4\Phi_{7/2}$, v=0	3665.04287(42)	0.199226807(94)	1.31806(16)				
$X\ ^4\Delta_{3/2}$, v=0	0	0.207934000(57)	1.35742(39)				
$A\ ^4\Phi_{5/2}$, v=0	3821.9041(14)	0.1993555(26)	1.845(11)				
$X\ ^4\Delta_{1/2}$, v=0	0	0.208226134(38)	1.36260(14)	-3.9383(28)	-8.06(93)	…	…
$A\ ^4\Phi_{3/2}$, v=0	3920.56439(56)	0.19952061(34)	1.34676(44)				

As all four spin components of the $X\,^4\Delta_i$ and $A\,^4\Phi_i$ states in CoS were observed, a Hund's case (a) fit was also performed for the 0 – 0 band of the $A\,^4\Phi_i - X\,^4\Delta_i$ transition. The observed lines were fitted to the usual $\hat{N}^2$ Hamiltonian for $^4\Delta$ and $^4\Phi$ states as given by Brown *et al*. [20]. An explicit listing of the matrix elements was provided by Brown *et al*. [21] for $^4\Delta$ states, and by Merer *et al*. [22] for $^4\Phi$ states. The output files of this fit have been published in the supplementary table of Ref. [17]. The spectroscopic constants obtained are given in Table 8.2. The spin-orbit constant A and spin-spin constant λ for the $X\,^4\Delta_i$ ground state could not be determined, and they were fixed at the values from the previous microwave study [2]. As no transitions that cross spin components were observed, the Hund's case (a) constants obtained here are not very reliable (especially the spin-orbit constant A, the spin-spin constant λ and the high order spin-orbit constant η). At this moment, the constants obtained from the Hund's case (c) fit for CoS are preferred.

Table 8.2 Hund's case (a) constants (in cm^{-1}) for the $X\,^4\Delta_i$ and $A\,^4\Phi_i$ states of CoS.[a]

Constant	$X\,^4\Delta_i$		$A\,^4\Phi_i$
	Present work	Microwave[b]	Present work
T_0	0	0	3704.13298(32)
A_0	-160.3[b]	-160.3(11)	-163.141624(66)
$A_{D0}/10^{-5}$	-2.62379(29)	-2.652(97)	1.3282(38)
B_0	0.207759165(17)	0.207759119(20)	0.19927642(27)
$D_0/10^{-7}$	1.351809(66)	1.351480(87)	1.319618(68)
$p_0/10^{-9}$	-3.94(57)	-4.00(60)	…
$o_0/10^{-6}$	-1.83(15)	-1.86(13)	…
$n_0/10^{-4}$	-6.5645(43)	-6.5632(37)	…
λ_0	22.3[c]	22.28(93)	2.60388(15)
$\lambda_{D0}/10^{-5}$	3.75701(38)	3.55(22)	2.028(13)
$\lambda_{H0}/10^{-11}$	…	-4.20(60)	…
η_0	-0.71510(91)	-2.97(63)	-2.75155(63)
$\eta_{D0}/10^{-5}$	…	-1.26(24)	-2.286(18)

[a] All uncertainties are 1 σ.
[b] Ref. [2].
[c] Fixed at values from the microwave study by Flory *et al*. [2].

The $^4\Phi_i$– $^4\Delta_i$ transition is a fully allowed transition with $\Delta\Lambda = +1$ and $\Delta S = 0$, and in the present experiments on CoS, the $A\ ^4\Phi_i - X\ ^4\Delta_i$ transition was stronger than the $B\ ^4\Pi_i$–$X\ ^4\Delta_i$ transition. Ram *et al*. [7] did not observe the analogous $^4\Phi_i - {}^4\Delta_i$ transition in their study of CoO because they used a green glass filter, which cuts off the spectral region where this transition should be found. Surprisingly, this $^4\Phi_i$–$^4\Delta_i$ transition in CoO was not assigned in the matrix isolation study by Danset *et al*. [15], in which four electronic transitions were observed in the near-infrared region: the strongest transition at 5887 cm^{-1} was assigned to the 0-0 band of the $^4\Pi_{5/2} - X\ ^4\Delta_{7/2}$ sub-band, and the other three weaker transitions at 3387, 7010 and 10162 cm^{-1} were tentatively assigned to $^4\Sigma^- - X\ ^4\Delta_{7/2}$, $^6\Delta - X\ ^4\Delta_{7/2}$, and $^2\Delta - X\ ^4\Delta_{7/2}$ transitions, respectively. Attempts were made to generate the CoO molecule with the carbon tube furnace and to record its spectrum in the near infrared region, but they failed. The most likely reason is that CoO was reduced to Co by carbon at high temperature [23]. Investigations of CoO using other experimental methods, such as a hollow cathode lamp, are desirable in order to locate the expected $^4\Phi$ state with an energy of about 4000 cm^{-1} based on CoS. Indeed, it is likely that the $^4\Phi_{9/2}$ spin component has already been located (but misassigned) in matrix isolation experiments of Danset *et al*. [15]. The $^4\Sigma^-_{3/2} - X\ ^4\Delta_{7/2}$ transition is expected to be strongly forbidden ($\Delta\Omega = 2$), and appear rather weakly (if at all) in the matrix absorption spectrum. We therefore tentatively reassign this CoO transition at 3387 cm^{-1} in a neon matrix to the $A\ ^4\Phi_{9/2} - X\ ^4\Delta_{7/2}$ transition.

The $X\ ^4\Delta_i$ ground states of CoO and CoS have been determined to arise from a $\sigma^2\delta^3\pi^2$ electron configuration [2,5–10], and the $X\ ^4\Delta_i$ ground states of CoO and CoS have been found to have similar ^{59}Co nuclear hyperfine splittings [2,10]. Ram *et al*. [7] suggested that the $A\ ^4\Pi_i$ state of CoO arises from a mixture of two configurations ($\sigma^2\delta^2\pi^3$ and $\sigma^1\delta^3\pi^3$) based on observations of anomalous lineshapes in the $A\ ^4\Pi_{5/2} - X\ ^4\Delta_{7/2}$ sub-band. These anomalous lineshapes were assigned to partly resolved ^{59}Co nuclear hyperfine structure in the $A\ ^4\Pi_{5/2}$ state. No anomalous lineshapes were observed in the $A\ ^4\Phi_i - X\ ^4\Delta_i$ and $B\ ^4\Pi_i - X\ ^4\Delta_i$ transitions in CoS. It is more likely that the $B\ ^4\Pi_i$ state in CoS arises solely from the $\sigma^2\delta^2\pi^3$ configuration, since the $\sigma^1\delta^3\pi^3$ configuration with an unpaired electron in the Co 4*s* orbital would give rise to states with a large Fermi contact hyperfine parameter (b_F) and large magnetic hyperfine splittings. One possible reason for no observation of hyperfine structure in CoS could be that the resolution was 0.02 cm^{-1} in the experiment for CoO [7], while the resolution was 0.04 cm^{-1} in the present CoS experiment. The observed linewidths are 0.06 cm^{-1} for CoS. However, this explanation is not satisfactory, since the largest linewidth for the anomalous lines in CoO is 0.1 cm^{-1} [7]. Ram *et al*. [7] also suggested that in CoO there is a $^4\Sigma^-$ state lying close to the $^4\Pi_i$ state because of the large Ω-doubling observed in the $^4\Pi_{3/2}$ spin component. A similar situation exists in CoS, which is supported by the Ω-doubling observed in the $^4\Pi_{5/2}$ spin component in the present experiments.

The following configurations give rise to $^4\Phi$ states in CoO and CoS: $\sigma^1\delta^3\pi^3$, $\sigma^2\delta^3\pi^1\sigma^1$, and $\sigma^1\pi^4\sigma^2\delta^3\pi^3$ [8, 14]. The $\sigma^2\delta^3\pi^1\sigma^1$ configuration is the only one consistent with the lack of hyperfine structure in the CoS $A\ ^4\Phi_i$ state, because the mainly Co 4*s*σ orbital is filled and the unpaired σ electron is in a mainly 3*d*σ orbital. However, Barnes *et al*. [8] proposed that the $D\ ^4\Phi$ state of CoO observed in the visible region in their experiment arises from this configuration. High level ab initio calculations on CoO and CoS are desirable in order to locate all of the low-lying states and determine their configurations.

8.4 Conclusions

The near-infrared emission spectrum of CoS has been recorded at a resolution of 0.04 cm^{-1} using a Fourier transform spectrometer. Gas-phase CoS was produced by the reaction of cobalt vapor and CS_2 vapor at about 3000 K in a carbon tube furnace. Two electronic transitions were observed for the first time in the 3200 – 6000 cm^{-1} region, and have been assigned to the $A\ ^4\Phi_i - X\ ^4\Delta_i$ and $B\ ^4\Pi_i - X\ ^4\Delta_i$ transitions. The 0 – 0 bands for all four sub-bands of the $A\ ^4\Phi_i - X\ ^4\Delta_i$ transition, and the 0 – 0, 0 – 1, 1 – 0 and 1 – 1 bands for the 5/2 – 7/2 sub-band of the $B\ ^4\Pi_i - X\ ^4\Delta_i$ transition were rotationally analyzed. Combined with the previous microwave data from the literature, the present data were fitted using the usual Hund's case (c) energy level expressions, and spectroscopic constants were obtained for the $X\ ^4\Delta_i$, $A\ ^4\Phi_i$, and $B\ ^4\Pi_i$ states of CoS. A Hund's case (a) fit was also carried out for the $A\ ^4\Phi_i - X\ ^4\Delta_i$ transition.

The presence of a low-lying $^4\Phi_i$ state for both CoS and CoO was not anticipated based on previous experimental and theoretical work. The analogous $^4\Pi_i$ state for CoO has been observed previously, while the analogous $^4\Phi_i$ state in CoO remains to be located in the gas phase. Co nuclear hyperfine structure, which has been tentatively observed in the $^4\Pi_i$–$X\ ^4\Delta_i$ transition of CoO, was not observed in the analogous transition of CoS. More work, both experimental and theoretical, is desirable on the low-lying electronic states of CoS and CoO.

8.5 References

[1] A.J. Merer, Annu. Rev. Phys. Chem. **40**, 407 (1989).

[2] M.A. Flory, S.K. McLamarrah and LM. Ziurys, J. Chem. Phys. **123**, 164312 (2005).

[3] C.W. Bauschlicher Jr. and P. Maitre, Theor. Chim. Acta **90,** 189 (1995).

[4] A.J. Bridgeman and J. Rothery, J. Chem. Soc., Dalton Trans. 211 (2000).

[5] A.G. Adam, Y. Azuma, J.A. Barry, G. Huang, M.P.J. Lyne, A.J. Merer and J.O. Schröder, J. Chem. Phys. **86**, 5231 (1987).

[6] D.J. Clouthier, G. Huang, A.J. Merer and E.J. Friedman-Hill. J. Chem. Phys. **99**, 6336 (1993).

[7] R.S. Ram, C.N. Jarman and P.F. Bernath, J. Mol. Spectrosc. **160**, 574 (1993).

[8] M. Barnes, D.J. Clouthier, P.G. Hajigeorgiou, G. Huang, C.T. Kingston, A.J. Merer, G.F. Metha, J.R.D. Peers and S.J. Rixon, J. Mol. Spectrosc. **186**, 374 (1997).

[9] K.C. Namiki and S. Saito, J. Chem. Phys. **114**, 9390 (2001).

[10] S.K. McLamarrah, P.M. Sheridan and L.M. Ziurys, Chem. Phys. Lett. **414**, 301 (2005).

[11] M. Dolg, U. Wedig, H. Stoll and H. Preuss, J. Chem. Phys. **86**, 2123 (1987).

[12] G.L. Gutsev, B.K. Rao and P. Jena, J. Phys. Chem. A. **104**, 5374 (2000).

[13] E.L. Uzunova, G.St. Nikolov and H. Mikosch, J. Phys. Chem. A. **106**, 4104 (2002).

[14] B. Dai, K. Deng, J. Yang and Q. Zhu, J. Phys. Chem. **118**, 9608 (2003).

[15] D. Danset and L. Manceron, J. Phys. Chem. A. **107**, 11324 (2003).

[16] A.B. Anderson, S.Y. Hong and J.L. Smialek, J. Phys. Chem. **91**, 4250 (1987).

[17] S. Yu, I.E. Gordon, P.M. Phillip and P.F. Bernath, J. Mol. Spectrosc. **236**, 255 (2006).

[18] M. Carleer, "Wspectra: a Windows program to measure accurately the line intensities of high resolution Fourier Transform spectra", In: Russel JE, "Remote sensing of clouds and the atmosphere, EOS/SPIE. Proceedings series", **4168**, 337 (2001).

[19] F.W. Loomis and R.W. Wood, Phys. Rev. **32** 223 (1928).

[20] J.M. Brown, E.A. Colbourn, J.K.G. Watson and F.D. Wayne, J. Mol. Spectrosc. **74**, 294 (1979).

[21] J.M. Brown, A.S.-C. Cheung and A.J. Merer, J. Mol. Spectrosc. **124**, 464 (1987).

[22] A.J. Merer, G. Huang, A.S.-C. Cheung and A.W. Taylor, J. Mol. Spectrosc. **125**, 465 (1987).

[23] S. Budavari, M.J. O'Neil, A. Smith and P.E. Heckelman, *The Merck Index,* 11th ed., Merck & CO., Inc, Rahway, NJ, 1989.

Chapter 9

Laser excitation spectroscopy of SrOD

9.1 Introduction

The spectroscopy of the alkaline earth monohydroxides has been an active topic of discussion in many papers. Their extensive experimental and computational studies have been reviewed by Bernath [1,2] and Ellis [3]. For the SrOH/SrOD free radical, high-resolution studies have been limited to the $\widetilde{X}^2\Sigma^+$ ground state and the low-lying $\widetilde{A}^2\Pi$ and $\widetilde{B}^2\Sigma^+$ excited states. Additional excited states lie high in energy, and as a result, high-resolution studies using laser excitation spectroscopy are difficult to perform. The Bernath group has recently reported the first high-resolution study of the $\widetilde{C}^2\Pi - \widetilde{A}^2\Pi\ 0_0^0$ transition of SrOH using optical-optical double resonance (OODR) spectroscopy [4]. This chapter reports the first high-resolution study of the $\widetilde{C}^2\Pi - \widetilde{A}^2\Pi\ 0_0^0$ transition of SrOD using OODR spectroscopy, as well as the first high-resolution study of the $\widetilde{A}^2\Pi - \widetilde{X}^2\Sigma^+\ 0_0^0$ transition of SrOD using laser excitation spectroscopy.

The spectrum of SrOH was first described by Herschel in 1823 [5], who observed band systems centered at 660 and 610 nm. These bands were also observed by Barrow and Caldin [6], but were not identified as arising from SrOH until 1955 when James and Sugden [7] recognized the similarity between the alkaline-earth monohydroxide bands and the alkaline-earth halide bands. No rotational analysis of these bands was reported until 1983 when Nakagawa *et al*. [8] examined the 0_0^0, 1_1^1 and 2_1^1 bands of the $\widetilde{B}^2\Sigma^+ - \widetilde{X}^2\Sigma^+$ transition for both SrOH and SrOD. Later, Brazier *et al*. [9] rotationally analyzed the 0_0^0 bands of the $\widetilde{A}^2\Pi - \widetilde{X}^2\Sigma^+$ transition of SrOH using a combination of laser-induced fluorescence and Fourier transform spectroscopy. Additional investigations of vibrationally excited bands of the $\widetilde{A}^2\Pi - \widetilde{X}^2\Sigma^+$ and $\widetilde{B}^2\Sigma^+ - \widetilde{X}^2\Sigma^+$ transitions of SrOH were carried out by Presunka and Coxon [10-12] using high-resolution laser excitation spectroscopy. Also Zhao *et al*. [16] used supersonic jet-cooled molecular beam methods to observe the $\widetilde{B}^2\Sigma^+ - \widetilde{X}^2\Sigma^+$ transition of SrOD. The pure rotational spectra of the ground state of SrOH and SrOD have been examined by Anderson *et al*. [13] and Fletcher *et al*. [14,15].

Recently, using low-resolution laser excitation and dispersed fluorescence spectroscopy, Beardah and Ellis [17,18] have located the following five higher energy electronic states for SrOH: $\widetilde{B}'^2\Sigma^+$ (25997 cm^{-1}), $\widetilde{C}^2\Pi$ (27303 cm^{-1}), $\widetilde{D}^2\Sigma^+$ (27698 cm^{-1}), $\widetilde{E}^2\Sigma^+$ (29990 cm^{-1}), and $\widetilde{F}^2\Pi$ (32985 cm^{-1}). The subsequent OODR study of the $\widetilde{C}^2\Pi - \widetilde{A}^2\Pi\ 0_0^0$ transition of SrOH by the Bernath group [4] has been the only available high-resolution spectroscopic studies on these states.

In the present study, the 0_0^0 bands of the $\widetilde{A}^2\Pi - \widetilde{X}^2\Sigma^+$ and $\widetilde{C}^2\Pi - \widetilde{A}^2\Pi$ transitions of SrOD have been observed and rotationally analyzed. A total of 364 lines have been measured and assigned for the $\widetilde{A}^2\Pi - \widetilde{X}^2\Sigma^+\ 0_0^0$ transition, and 288 lines for the $\widetilde{C}^2\Pi - \widetilde{A}^2\Pi\ 0_0^0$ transition. The present data set was combined with the available ground state data from previous work, and a weighted least-squares fit was performed. A complete set of molecular spectroscopic constants has been obtained for the $\widetilde{X}^2\Sigma^+$

(000), $\widetilde{A}^2\Pi$ (000) and $\widetilde{C}^2\Pi$ (000) states of SrOD. The results presented in this chapter have been published in Ref. [19].

9.2 Experimental details

The SrOD molecules were generated by the reaction of Sr metal vapor and D_2O vapor in a Broida-type oven, which has been described in Section 2.1.3. Sr metal was resistively heated in a carbon crucible to produce the metal vapor, which was entrained in a flow of ~6 Torr of argon carrier gas. The oxidant gas, D_2O vapor, was admitted to the argon metal-vapor mixture through a ring located above the oven, which was connected to a glass tube containing liquid D_2O at room temperature.

The $\widetilde{A}^2\Pi - \widetilde{X}^2\Sigma^+$ transition was recorded by laser excitation spectroscopy (Section 2.2.2). Figure 9.1 shows an energy level diagram of $^2\Pi$ and $^2\Sigma^+$ states and the allowed transitions between these two states. The output of a cw single-mode ring DCM dye laser (Coherent 699-29) was focused vertically into the reaction chamber of the Broida-type oven. The typical laser power was 400-600 mW in the range of 14500–14850 cm^{-1}. As the ring dye laser was scanned, the excitation fluorescence from the $\widetilde{A}^2\Pi$ state was collected using a photomultiplier tube (PMT) with a 725 nm red pass filter. Most branches obtained by this way were clear and easily assigned, except for the R_{2ff}, Q_{21fe} and R_{21ee} branches (Figure 9.2). These three branches are on the high wavenumber side of the band origin, and are probably overlapped with branches from hot bands (e.g., 2_1^1). To simplify the appearance of the spectra, these three branches were also recorded using selective fluorescence detection [8,20]. By scanning the laser through these three branches and monitoring the fluorescence from the connecting P_{21ee}, Q_{2ef} and P_{2ff} branches through a monochromator, the complexity and congestion of the spectrum were much reduced (Figure 9.2).

The $\widetilde{C}^2\Pi - \widetilde{A}^2\Pi$ transition was recorded by OODR spectroscopy (Section 2.2.3). The pump laser was a linear cavity dye laser with a bandwidth of about 1 cm^{-1}. This laser was used to excite the $\widetilde{A}^2\Pi_{1/2} - \widetilde{X}^2\Sigma^+$ 0_0^0 transition at 14535 cm^{-1} (the P_{1ee} and Q_{12ef} band heads) and the $\widetilde{A}^2\Pi_{3/2} - \widetilde{X}^2\Sigma^+$ 0_0^0 transition at 14795 cm^{-1} (the P_{21ee} and Q_{2ef} band heads). The probe laser was a single-mode titanium-sapphire ring laser (Coherent 822-29), which was used to promote the SrOD molecules from the $\widetilde{A}^2\Pi$ state to the $\widetilde{C}^2\Pi$ state. Because there was no low resolution work on the high-lying states of SrOD, the probe laser wavenumbers for each spin-orbit component of the $\widetilde{C}^2\Pi - \widetilde{A}^2\Pi$ transition were chosen based on the corresponding transition of SrOH in the previous work [4]. The output of the pump and probe lasers were directed collinearly and focused into the reaction chamber of the Broida-type oven. The signal was optimized by maximizing the overlap of the pump and probe lasers in the reaction zone. As the probe laser was scanned, the excitation fluorescence from the $\widetilde{C}^2\Pi$ state was collected using a PMT with a 500 nm blue pass filter. The probe laser scanned the 12690-12805 cm^{-1} region for the $\widetilde{C}^2\Pi_{1/2} - \widetilde{A}^2\Pi_{1/2}$ transition, and the 12450 – 12600 cm^{-1} region for the $\widetilde{C}^2\Pi_{3/2} - \widetilde{A}^2\Pi_{3/2}$ transition.

In both experiments, a small fraction of the single-mode laser beam was directed into an I_2 cell. The laser excitation spectrum of I_2 [21] was recorded simultaneously to calibrate the line positions of the $\widetilde{A}^2\Pi - \widetilde{X}^2\Sigma^+$ transition and the absorption spectrum of I_2 [22] was recorded simultaneously to

calibrate the line positions of the $\widetilde{C}^2\Pi - \widetilde{A}^2\Pi$ transition. The accuracy of the SrOD line positions is approximately 0.005 cm^{-1}.

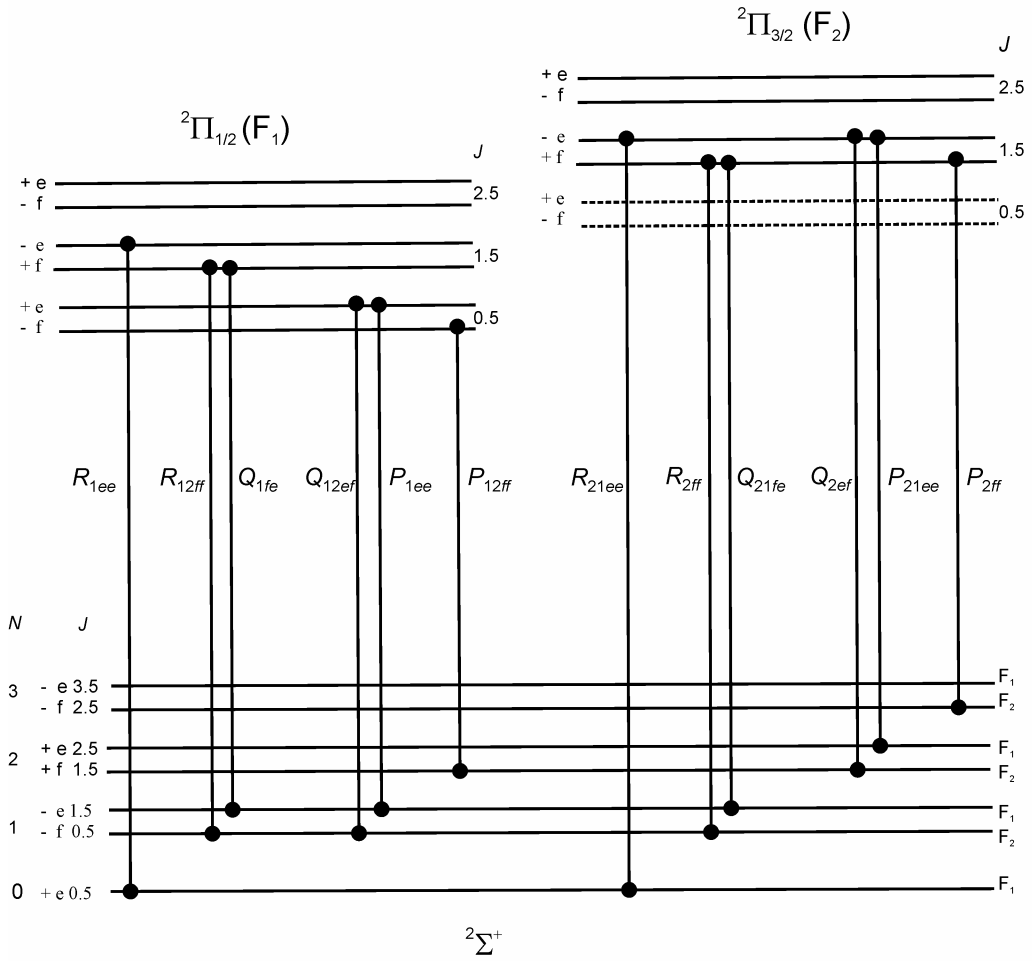

Figure 9.1 An energy level diagram of the $\widetilde{X}^2\Sigma^+$ (000) and $\widetilde{A}^2\Pi$ (000) states of SrOD. Each rotational level of the $\widetilde{X}^2\Sigma^+$ state is split into a doublet due to spin-rotation interaction, and is labeled by quantum numbers *N*, *J*, rotationless (*e*/*f*) parity and total (+/–) parity. Each rotational level of the $\widetilde{A}^2\Pi$ state is is split into a doublet due to Λ-doubling, and is labeled by quantum numbers *J*, rotationless (*e*/*f*) parity and total (+/–) parity. The twelve allowed branches of the $X\,^2\Pi - X\,^2\Pi$ transition are labeled by the branch notation $\Delta J_{F', F'', P', P''}$ (F=1 or 2 and P = *e* or *f*) or $\Delta J_{F, P', P''}$ if F′=F″=F.

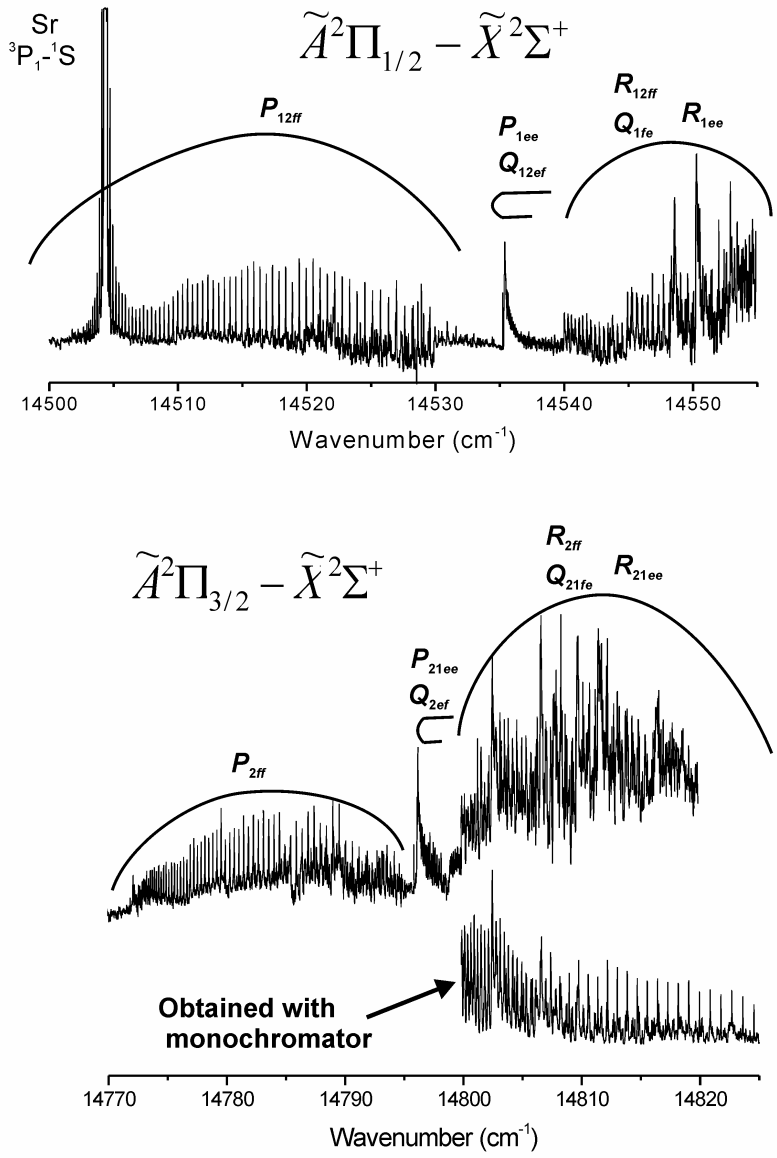

Figure 9.2 An overview of the 0_0^0 band of the $\widetilde{A}^2\Pi - \widetilde{X}^2\Sigma^+$ transition of SrOD. The spectra were recorded by scanning the single-mode ring dye laser and monitoring the fluorescence with a 725 nm red pass filter or through a monochromator. All twelve branches for this transition were observed.

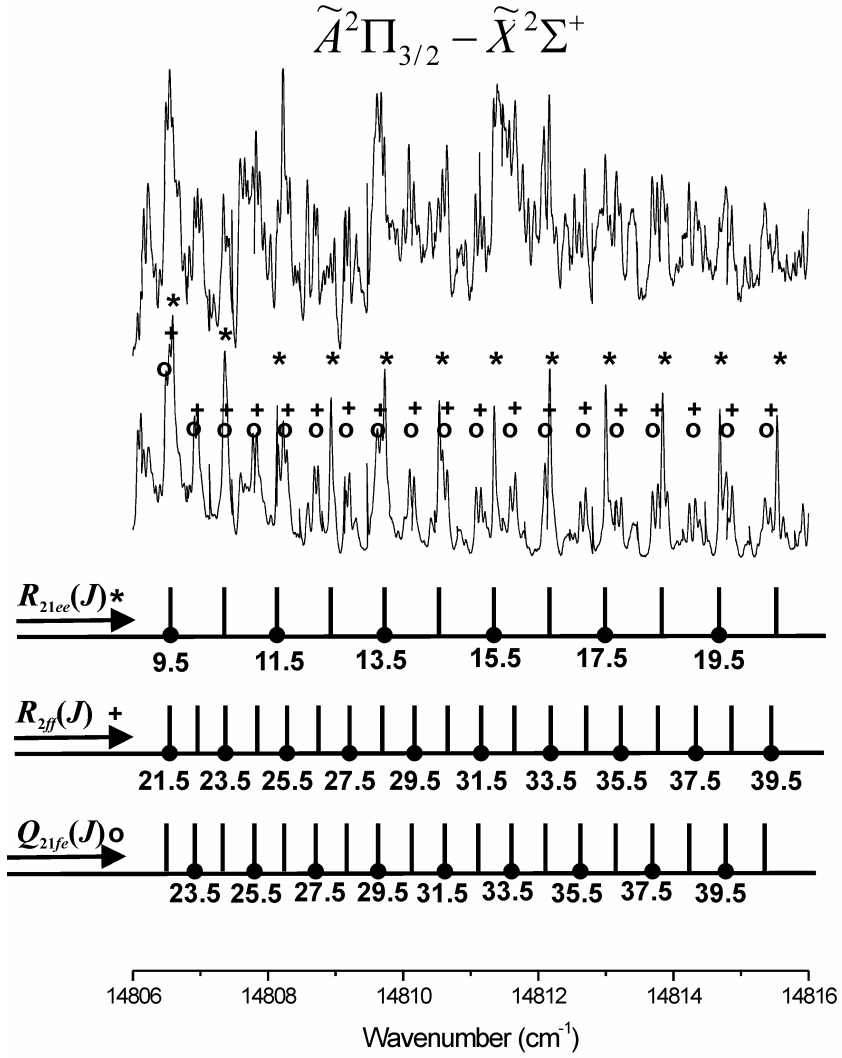

Figure 9.3 An expanded view of the R_{21ee}, R_{2ff} and Q_{21fe} and branches of the 0_0^0 band of the $\widetilde{A}^2\Pi - \widetilde{X}^2\Sigma^+$ transition of SrOD. The top spectrum was obtained by scanning the single-mode ring dye laser and monitoring the fluorescence with a 725 nm red pass filter, and the bottom spectrum was obtained by scanning the single-mode ring dye laser and monitoring the fluorescence through a monochromator. The R_{2ff} and Q_{21fe} branches are split by the spin-rotation interaction in the ground state, which is resolved starting at $J = 15.5$.

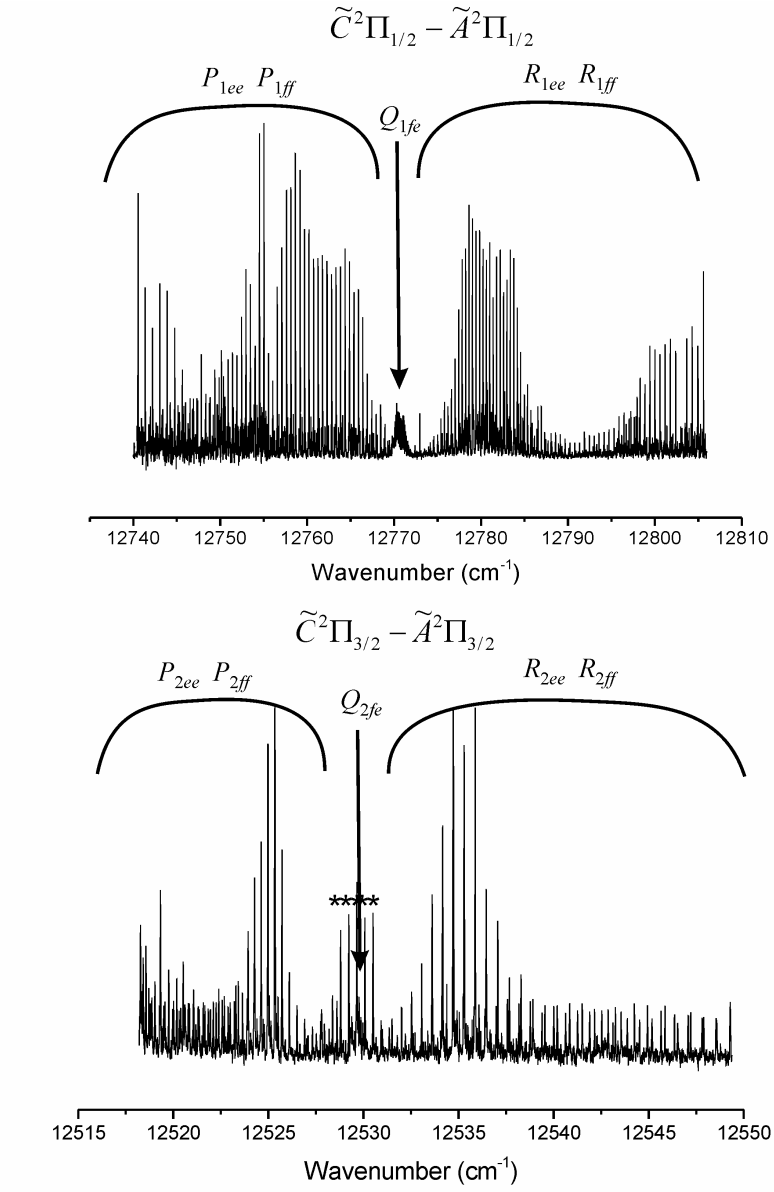

Figure 9.4 An overview of the 0_0^0 band of the $\widetilde{C}^2\Pi - \widetilde{A}^2\Pi$ transition of SrOD recorded by OODR spectroscopy. Both spectra exhibit a double *P* and double *R* structure, and the intensity pattern in the *P* and *R* branches results from the various *J* levels populated in the $\widetilde{A}^2\Pi$ state by the pump laser. The *Q* branches for both spin components are weak. Strong lines located near the Q_{2fe} branch, indicated by asterisks, are probably due to an excited vibrational band.

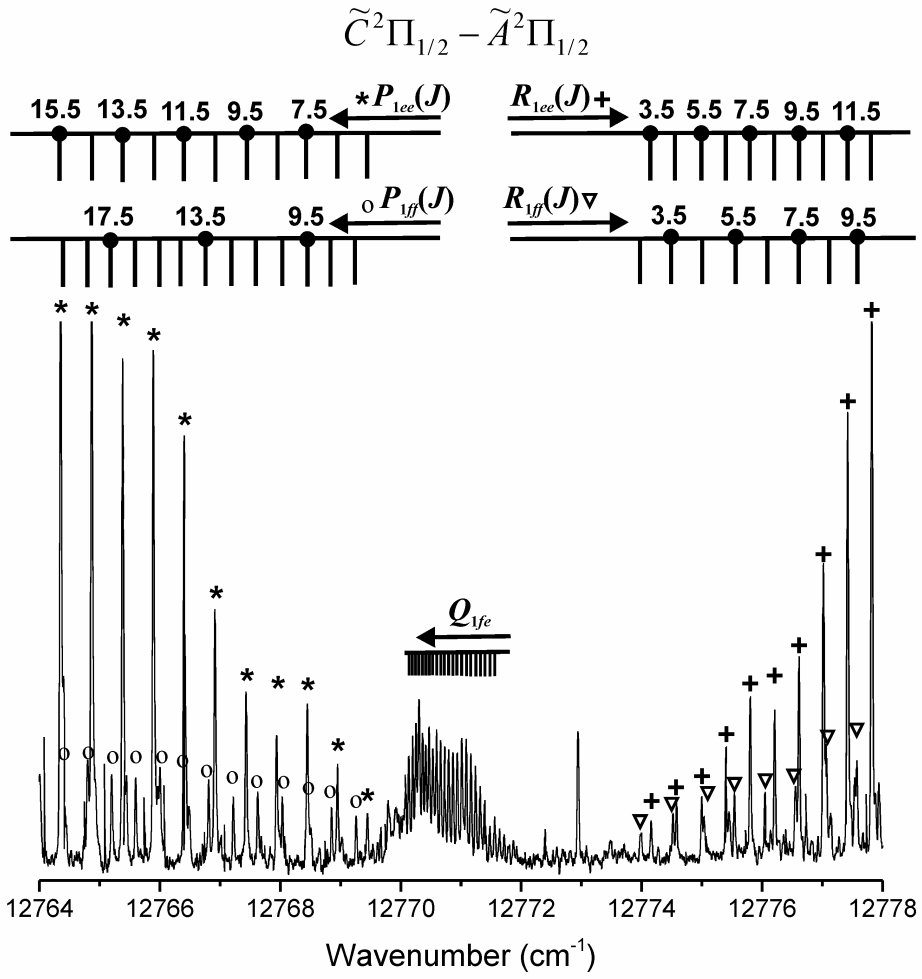

Figure 9.5 An expanded view of the 0_0^0 band of the $\widetilde{C}^2\Pi_{1/2} - \widetilde{A}^2\Pi_{1/2}$ transition of SrOD recorded by OODR spectroscopy. The pump laser was fixed to excite the heads of the P_{1ee} and Q_{12ef} branches of the $\widetilde{A}^2\Pi - \widetilde{X}^2\Sigma^+\ 0_0^0$ transition; therefore, *e* parity levels were predominately populated in the $\widetilde{A}^2\Pi$ state. As a result, the P_{1ee} and R_{1ee} branches are more intense than the P_{1ff} and R_{1ff} branches, and the Q_{1ef} branch was not observed. The Λ-doubling splitting is resolved at very low *J* values.

9.3 Results and discussion

An energy level diagram of $^2\Pi$ and $^2\Sigma^+$ states is shown in Figure 9.1. The $^2\Sigma^+$ levels are located on the bottom and the $^2\Pi$ levels are located at the top. The spin-orbit constant A of the $\widetilde{A}^2\Pi$ state of SrOD is 260 cm^{-1}; therefore, the two subbands, $\widetilde{A}^2\Pi_{1/2} - \widetilde{X}^2\Sigma^+$ and $\widetilde{A}^2\Pi_{3/2} - \widetilde{X}^2\Sigma^+$, are well separated. The selection rules $\Delta J = \pm 1$, $e - e$ and $f - f$ or $\Delta J = 0$ and $e - f$ gives rise to six branches for each subband: P_{ff}, P_{ee}, Q_{ef}, R_{ff}, Q_{fe}, and R_{ee}, which are spaced approximately by $-3B$, $-B$, $-B$, $+B$, $+B$ and $+3B$, respectively. The two $-B$ branches (P_{ee} and Q_{ef}) and the two $+B$ branches (R_{ff} and Q_{fe}) are separated by the ground-state spin-rotation interaction.

Figure 9.2 shows an overview spectrum of the $\widetilde{A}^2\Pi - \widetilde{X}^2\Sigma^+$ 0_0^0 transition obtained by laser excitation spectroscopy. Transitions in all twelve branches were observed and rotationally assigned. The $-B$ branches give rise to strong band heads at J of around 30, and the -3B branches give rise to weak bandheads at J of around 80. The spin-rotation splitting in the ground state is resolved starting at J'' = 15.5. Figure 9.3 shows an expanded view of the R_{2ff}, Q_{21fe} and R_{21ee} branches. Rotational assignments were made using lower state combination differences [13].

The rotational transitions observed for the $\widetilde{A}^2\Pi - \widetilde{X}^2\Sigma^+$ 0_0^0 transition of SrOD were fitted together using a weighted nonlinear least-squares procedure. The energy levels of the $\widetilde{X}^2\Sigma^+(000)$ and $\widetilde{A}^2\Pi(000)$ states of SrOD were calculated using the usual $\hat{N}^2$ Hamiltonian of Brown [23], with matrix elements derived using Hund's case (a) basis functions. An explicit listing of $^2\Pi$ matrix elements is provided in Table 1.2, and the following energy level expression was used for the $X\,^2\Sigma^+$ state:

$$F(J) = BJ(J \pm 1) - D[J(J \pm 1)]^2 - 0.5\gamma(1 \pm J), \qquad (9.1)$$

where the upper (lower) sign refers to f (e) parity. The results of this fit provided combination differences for the $\widetilde{A}^2\Pi(000)$ state of SrOD, which were used for the rotational assignments in the 0_0^0 band of the $\widetilde{C}^2\Pi - \widetilde{A}^2\Pi$ transition.

A $^2\Pi - {}^2\Pi$ transition has two subbands: $^2\Pi_{1/2} - {}^2\Pi_{1/2}$ and $^2\Pi_{3/2} - {}^2\Pi_{3/2}$, which are separated by the difference between the spin-orbit constants A of the two states. There are six allowed branches in each subband, which are the same as those in the $^2\Pi_{1/2} - {}^2\Pi_{3/2}$ transition of TeH (Figure 4.1). Figure 9.4 shows an overview of the 0_0^0 band of the $\widetilde{C}^2\Pi - \widetilde{A}^2\Pi$ transition in SrOD recorded by OODR spectroscopy. Each spectrum exhibits a clear P, Q, and R structure. Because $\Delta\Lambda = 0$ for the $\widetilde{C}^2\Pi - \widetilde{A}^2\Pi$ transition, the Q branch lines are weak [24]. Figure 9.5 shows an expanded view of the $\widetilde{C}^2\Pi_{1/2} - \widetilde{A}^2\Pi_{1/2}$ 0_0^0 transition. Because the pump laser was set to excite the P_{1ee}, Q_{12ef} (at 14535 cm^{-1}) and P_{21ee}, Q_{2ef} (at 14795 cm^{-1}) bandheads of the $\widetilde{A}^2\Pi - \widetilde{X}^2\Sigma^+$ 0_0^0 transition, e parity levels were predominately populated in the $\widetilde{A}^2\Pi(000)$ state. As a result, the P_{ee} and R_{ee} branches of the $\widetilde{C}^2\Pi - \widetilde{A}^2\Pi$ 0_0^0 transition are more intense than the P_{ff} and R_{ff} branches, and the Q_{ef} branches for both spin components were not observed in the present experiment. The rotational assignments of the P_{ee}, R_{ee}, P_{ff} and R_{ff} branches were made using lower state combination differences in the $\widetilde{A}^2\Pi(000)$ state.

Assignments in the weak Q_{fe} branches were made by predictions using the R_{ff} lines and the energy differences between the *e* and *f* levels in the $\widetilde{A}^2\Pi(000)$ state.

Additional weak bands were also observed in the OODR experiments, one of which was observed with a band origin of around 12713 cm^{-1}, and their lower state was confirmed to be the $\widetilde{A}^2\Pi_{1/2}(000)$ state by lower state combination differences. Only the R_{ee} and P_{ee} branches (*J*″ from 5.5 to 36.5) were rotationally assigned for this band. Another band was observed with a band origin of around 12586 cm^{-1}, and the lower state was confirmed to be the $\widetilde{A}^2\Pi_{3/2}(000)$ state. Only the R_{ee} and P_{ee} branches (*J*″ from 5.5 to 36.5) were rotationally assigned for this band. Because only two branches were assigned for these two bands, we do not have enough information to determine their upper states. Beardah and Ellis [18] observed the $\widetilde{B}'^2\Sigma^+$ state of SrOH with energies of 25997 cm^{-1}. The $\widetilde{A}^2\Pi_{1/2}(000)$ and $\widetilde{A}^2\Pi_{3/2}(000)$ states of SrOD have energies of 14537 and 14799 cm^{-1}, respectively. The 0_0^0 bands of the $\widetilde{B}'^2\Sigma^+ - \widetilde{A}^2\Pi_{1/2}$ and $\widetilde{B}'^2\Sigma^+ - \widetilde{A}^2\Pi_{3/2}$ transitions would be located at 11460 and 11198 cm^{-1}, respectively. The Sr-O stretching mode (ν_3) and the Sr-O-D bending mode (ν_2) in the ground state of SrOD were determined to be 517 and 282 cm^{-1}, respectively [2,8,16]. The combination bands $2_0^3 3_0^1$ and $2_0^1 3_0^2$ of the $\widetilde{B}'^2\Sigma^+ - \widetilde{A}^2\Pi_{1/2}$ and $\widetilde{B}'^2\Sigma^+ - \widetilde{A}^2\Pi_{3/2}$ transitions are expected to be at around 12800 and 12500 cm^{-1}. Therefore the two unknown upper states are tentatively assigned as the (012) and (031) levels of the $\widetilde{B}'^2\Sigma^+$ state.

Finally, a simultaneous least-squares fit was performed, which included the present $\widetilde{A}^2\Pi - \widetilde{X}^2\Sigma^+ 0_0^0$ and $\widetilde{C}^2\Pi - \widetilde{A}^2\Pi 0_0^0$ data, as well as the pure rotational transitions measured in the microwave study of the $\widetilde{X}^2\Sigma^+$ (000) state [13]. An estimated uncertainty of 0.005 cm^{-1} was used for most lines obtained in this work, and an uncertainty of 10^{-6} cm^{-1} for the millimeter-wave transitions. Local perturbations were observed at $J = 30.5$ for both *e* and *f* levels of the $\widetilde{C}^2\Pi_{1/2}(000)$ state, and at $J = 23.5$ for both *e* and *f* levels of the $\widetilde{C}^2\Pi_{3/2}(000)$ state, and the perturbed lines were simply deweighted in the fit. The output files of the fit (including complete lists of all data) have been published in the supplementary tables of Ref. [19].

Table 9.1 Hund's case (a) constants (in cm^{-1}) for the $\widetilde{X}^2\Sigma^+$, $\widetilde{A}^2\Pi$ and $\widetilde{C}^2\Pi$ states of SrOD.[a]

Constant	$\widetilde{X}^2\Sigma^+$ (000)	$\widetilde{A}^2\Pi$ (000)	$\widetilde{C}^2\Pi$ (000)
T	0.0	14668.07360(40)	27318.88299(62)
B	0.225316156(14)	0.22932627(53)	0.2316110(15)
$D/10^{-7}$	1.66514(14)	1.6579(12)	2.3965(64)
$\gamma/10^{-3}$	2.20143(32)	…	…
A	…	262.52710(52)	19.5525(11)
$A_D/10^{-4}$	…	…	-3.087(22)
p	…	-0.130107(28)	-0.032380(51)
$q/10^{-4}$	…	-1.361(40)	-8.923(16)

[a] All uncertainties are 1σ.

The spectroscopic constants obtained for SrOD are provided in Table 9.1. In the fit, the absolute energy of the 000 level of the $\widetilde{X}^2\Sigma^+$ ground state was fixed at zero. The origins obtained for the $\widetilde{A}^2\Pi(000)$ and $\widetilde{C}^2\Pi(000)$ states are 14668.07360 (40) cm^{-1} and 27318.88299 (63) cm^{-1} relative to this level, respectively. From the previous paper on SrOH [4], the origins for the $\widetilde{A}^2\Pi(000)$ and $\widetilde{C}^2\Pi(000)$ states are 14674.04171 (39) cm^{-1} and 27307.24754(66) cm^{-1} relative to the 000 level of the $\widetilde{X}^2\Sigma^+$ ground state of SrOH, respectively. The differences between the origins are approximately 10 cm^{-1}. An A_D term was required for the $\widetilde{C}^2\Pi(000)$ state to successfully model the data, which is probably due to the local perturbations observed in different *e* and *f* levels in the $\widetilde{C}^2\Pi(000)$ state. All the other constants are comparable to those for SrOH, except for the $\widetilde{C}^2\Pi(000)$ state spin-orbit constant. For the $\widetilde{A}^2\Pi(000)$ state, a value of 262.52710(52) cm^{-1} was obtained for SrOD and 263.58782(61) cm^{-1} for SrOH. However, for the $\widetilde{C}^2\Pi(000)$ state, a value of 19.5525(11) cm^{-1} was obtained for SrOD and 24.6607(11) cm^{-1} for SrOH. At this moment, there is not enough information to explain the discrepancy in the $\widetilde{C}^2\Pi$ state spin-orbit constants of SrOH and SrOD. Evidently there are local and global perturbations in the $\widetilde{C}^2\Pi$ state that are different for SrOH and SrOD.

As noted in the previous work [4], there is a remarkable difference in the value of the spin-orbit constant between the $\widetilde{A}^2\Pi(000)$ and $\widetilde{C}^2\Pi(000)$ states, which can be attributed to the molecular orbital character of the unpaired electron [4]. The molecular spin-orbit constant A can be represented by a linear combination of the atomic spin-orbit coupling constants, whose coefficients are the orbital mixing percentages. The Sr atomic spin-orbit coupling constants are 534 cm^{-1} for 5$p\pi$ orbital, 112 cm^{-1} for the 4$d\pi$ orbital, 192 cm^{-1} for the 6$p\pi$ orbital and 30 cm^{-1} for the 5$d\pi$ orbital [25]. The molecular orbital of the unpaired electron in the $\widetilde{A}^2\Pi$ state has large mixing percentages of the 5$p\pi$ and 4$d\pi$ atomic orbitals, while the molecular orbital in the $\widetilde{C}^2\Pi$ state has small mixing percentages of

the $5p\pi$ and $4d\pi$ orbitals and large mixing percentages of higher energy orbitals, which results in a much smaller spin-orbit constant in the $\widetilde{C}^2\Pi$ state.

Table 9.2 Bond lengths (Å) for SrOH.

	$\widetilde{X}^2\Sigma^+$ [a]	$\widetilde{A}^2\Pi$ [b]	$\widetilde{B}^2\Sigma^+$ [c]	$\widetilde{C}^2\Pi$ [b]
r_0 (SrO)	2.111	2.091	2.098	2.096
r_0 (OH)	0.922	0.922	0.921	0.822

[a] Determined from millimeter-wave data of SrOH, SrOD and ^{86}SrOH [13].
[b] Determined from optical data of SrOH [4] and SrOD [this work].
[c] Determined from optical data of SrOH and SrOD [8].

The obtained B_0 constants allowed the r_0 bond lengths to be calculated for the $\widetilde{A}^2\Pi$ and $\widetilde{C}^2\Pi$ states. Table 9.2 lists the r_0 bond lengths for the $\widetilde{X}^2\Sigma^+$, $\widetilde{A}^2\Pi$, $\widetilde{B}^2\Sigma^+$ and $\widetilde{C}^2\Pi$ states of SrOH. A value of 0.822 Å was determined for the OH bond length in the $\widetilde{C}^2\Pi$ state, which appears unusually small for a rigidly linear molecule. A $^2\Pi$ Hamiltonian successfully fits the experimental data, suggesting that SrOH is linear or very nearly linear in its $\widetilde{C}^2\Pi$ state. The unusually small OH bond length perhaps indicates that the $\widetilde{C}^2\Pi$ state of SrOH has a floppy bending potential similar to the ground state of MgOH [26]. The ground state of MgOH has an OH r_0 bond length of 0.871 Å [26]. Alternately, the global perturbations of the $\widetilde{C}^2\Pi$ state that have resulted in different A values for SrOH and SrOD may also have given different non-mechanical contributions to the B values. These perturbed B values would then result in anomalous bond lengths.

9.4 Conclusions

High-resolution spectra of SrOD have been recorded using optical-optical double-resonance spectroscopy and laser excitation spectroscopy. SrOD was produced by the reaction of Sr metal vapor and D_2O vapor in a Broida-type oven. The 0_0^0 bands of the $\widetilde{A}^2\Pi - \widetilde{X}^2\Sigma^+$ and $\widetilde{C}^2\Pi - \widetilde{A}^2\Pi$ transitions were observed and rotationally analyzed for the first time. Combined with the previous microwave data from the literature, the present data were fitted using the usual $^2\Sigma^+$ and $^2\Pi$ Hamiltonians, and spectroscopic constants were obtained for the $\widetilde{X}^2\Sigma^+$ (000), $\widetilde{A}^2\Pi$ (000) and $\widetilde{C}^2\Pi$ (000) states of SrOD. An unusually small OH bond length was obtained for the $\widetilde{C}^2\Pi$ state, perhaps indicating that the $\widetilde{C}^2\Pi$ state of SrOH has a floppy potential similar to the ground state of MgOH.

9.5 References

[1] P.F. Bernath, Science **254**, 665 (1991).

[2] P.F. Bernath, Adv. Photochem. **23**, 1 (1970).

[3] A.M. Ellis, Int. Rev. Phys. Chem. **20**, 551 (2001).

[4] J.-G. Wang, P.M. Sheridan, M.J. Dick and P.F. Bernath, J. Mol. Spectrosc. **236**, 21 (2006).

[5] J.F.W. Herschel, Trans. Roy. Soc. Edinburg **9**, 445 (1823).

[6] R.F. Barrow and E. F. Caldin, Proc. Phys. Soc. B **62**, 32 (1948).

[7] C.G. James and T.M. Sugden, Nature (London) **175**, 333 (1955).

[8] J. Nakagawa, R.F. Wormsbecher and D.O. Harris, J. Mol. Spectrosc. **97**, 37 (1983).

[9] C.R. Brazier and P.F. Bernath, J. Mol. Spectrosc. **114**, 163 (1985).

[10] P.I. Presunka and J.A. Coxon, Can. J. Chem. **71**, 1689 (1993).

[11] P.I. Presunka and J.A. Coxon, J. Chem. Phys. **101**, 201 (1994).

[12] P.I. Presunka and J.A. Coxon, Chem. Phys. **190**, 97 (1995).

[13] M.A. Anderson, W.L. Barclay Jr. and L.M. Ziurys, Chem. Phys. Lett. **196**, 166 (1992).

[14] D.A. Fletcher, K.Y. Jung, C.T. Scurlock and T.C. Steimle, J. Chem. Phys. **98**, 1837 (1993).

[15] D.A. Fletcher, M.A. Anderson, W.L. Barclay, Jr. and L.M. Ziurys, J Chem. Phys. **102**, 4334 (1995).

[16] C. Zhao, P.G. Hajigeorgiou, P.F. Bernath and J.W. Hepburn, J. Mol. Spectrosc. **176**, 268 (1996).

[17] M.S. Beardah and A.M. Ellis, J. Chem. Phys. **110**, 11244 (1999).

[18] M.S. Beardah and A.M. Ellis, J. Mol. Spectrosc. **218**, 80 (2003).

[19] S. Yu, J.-G. Wang, P.M. Sheridan, M.J. Dick and P.F. Bernath, J. Mol. Spectrosc. **240**, 14 (2006).

[20] C. Linton, J. Mol. Spectrosc. **69**, 351 (1978).

[21] S. Gerstenkorn and P. Luc, *Atlas du spectre d'Absorption de la Molécule d'Iode*, Laboratorie Aimé-Cotton, CNRS 91405, Orsay, France, 1978.

[22] S. Gerstenkorn, J. Verges and J. Chevillard, *Atlas du spectre d'Absorption de la Molécule d'Iode*, Laboratorie Aimé-Cotton, CNRS 91405, Orsay, France, 1982.

[23] J.M. Brown, E.A. Colbourn, J.K.G. Watson and F.D. Wayne, J. Mol. Spectrosc. **74**, 294 (1979).

[24] G. Herzberg, *Molecular Spectra and Molecular Structure, Vol.* 1, Krieger, Malabar, Florida, 1989.

[25] C.E. Moore, *Atomic Energy Levels, NSRDS Natl. Bur. Stand. No.* 35, U.S. GPO, Washington, DC, 1971, p.192.

[26] A.J. Apponi, M.A. Anderson and L.M. Ziurys, J. Chem. Phys. **111**, 10919 (1999).